# Quantum chemical description of ultrafast exciton self-trapping in perylene based materials

Dissertation

zur Erlangung des naturwissenschaftlichen Doktorgrades

der Julius-Maximilians-Universität Würzburg

vorgelegt von

**Volker Settels**

aus

Mönchengladbach

Würzburg, 2012

Eingereicht bei der Fakultät für Chemie und Pharmazie am

_____

Gutachter der schriftlichen Arbeit

1. Gutachter: _____

2. Gutachter: _____

Prüfer des öffentlichen Promotionskolloquiums

1. Prüfer: _____

2. Prüfer: _____

3. Prüfer: _____

Datum des öffentlichen Promotionskolloquiums

_____

Doktorurkunde ausgehändigt am

_____

# Table of contents


1. Introduction ..... 1

2. Prolegomena ..... 3

2.1 Organic solar cells ..... 3

2.2 Perylene based materials ..... 11

2.3 Exciton transfer in organic materials ..... 15

2.4 Exciton self-trapping ..... 21

3. Theoretical principles ..... 27

3.1 A brief introduction into linear response theory ..... 28

3.2 Configuration Interaction Singles (CIS) ..... 31

3.3 Time-dependent Hartree-Fock theory (TDHF) ..... 33

3.4 Time-dependent Density Functional Theory (TDDFT) ..... 39

3.5 Approximate Coupled Cluster method 2$^{nd}$ order (CC2) ..... 47

3.6 Algebraic Diagrammatic Construction (ADC) ..... 53

4. Computational details ..... 57

5. Exciton self-trapping in perylene based materials ..... 67

5.1 Exciton self-trapping in helical aggregates ..... 67

5.2 Exciton self-trapping in crystals ..... 77

6. Comparison of the electronic structure in perylene based materials ..... 89

6.1 Differences in global minima of the electronic ground state ..... 92

6.2 Energies of the first excited states as a function of a torsion motion ..... 95

6.3 Energies of the first excited states as a function of a shift motion ..... 106

7. Solvatochromic shifts for perylene based materials ..... 111

7.1 Solvent effects on the ground and first excited states ..... 114

7.2 Linear model to estimate solvatochromic shifts ..... 118

7.3 Solvent effects for SCS-CC2 ..... 121

7.5 Molecular solvation ..... 124

7.6 Influence of solvent effects on exciton self-trapping ..... 126

8. Summary ..... 129

Zusammenfassung ..... 133

Bibliography ..... 137

List of abbreviations ..... 147

Danksagung ..... 149

# 1. Introduction

The world's growing population and technological progress leads to an ever increasing demand for energy services.[1] It has become obvious that the energy demand cannot be met using fossil energy sources solely, not only because of their limited availability but also due to their detrimental effects on the environment and world climate.[2] Regenerative energy sources on the other hand have the potential to fill the gap as they are both virtually unlimited and in general environmental friendly. An obvious energy source is sun radiation, which delivers $1.5 \cdot 10^{18}$ kWh of energy per year to the earth.[3] In 2010 the global demand for energy was only a tiny fraction of this ($1.4 \cdot 10^{11}$ kWh).[4]

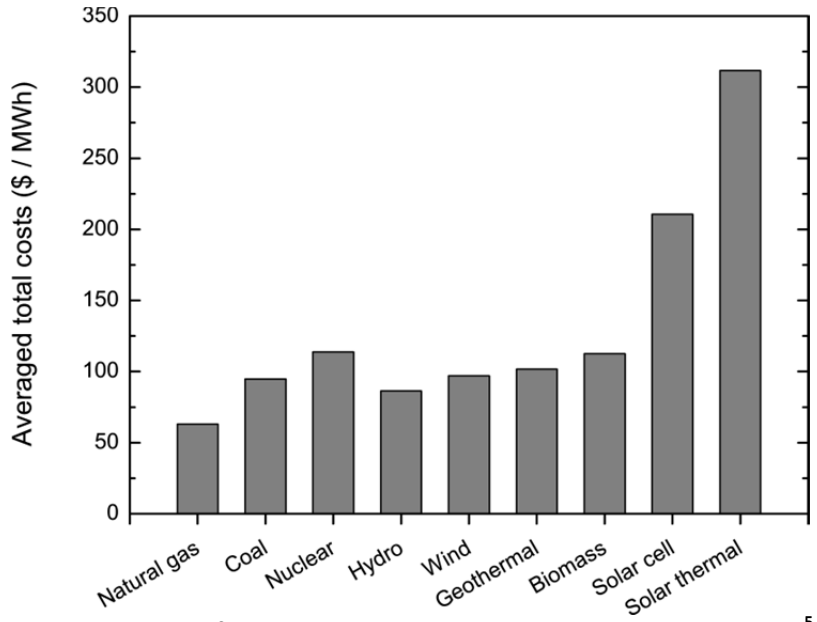


**Figure 1: Estimated averaged costs of energy generating technologies in the USA in 2016.[5] The reference for the currency rate of the US-Dollar ($) is the year 2009.**

The problem is that solar energy is economically still not competitive compared to other energy sources, which is demonstrated by Figure 1. However, in the case of photovoltaic devices there is prospective improvement. Today, mostly inorganic solar cells are used for solar energy conversion into electric power. However, they are fabricated using cost-intensive materials and production, which is especially the case for cells based on mono-crystalline silicon. The best performing devices yield efficiencies up to 25 %.[6] However, the production requires an enormous amount of energy, which has a negative effect on the price/performance ratio. Multi-crystalline devices have a slightly lower efficiency of 20.4 %,[6] but the price/performance ratio is much better. The highest shares in the market have solar cells using amorphous silicon. They are cheaper than the multi-crystalline silicon

devices, but only have an efficiency up to 10.1 %.[6] This is only a third of the efficiency of the best performing devices, which are based on thin GaAs films (28.3 %).[6] Unfortunately, these GaAs cells are even more expensive than mono-crystalline silicon based ones. To make solar cells competitive to other energy generating technologies, a need for development of new devices with a much better price/performance ratio is evident.

Future progress may be achieved by so-called organic solar cells (OPVs). These devices are based on organic materials, which are usually very cheap, and can be processed in easy ways (e.g. roll-to-roll printing). Additionally, only a small amount of material is necessary to construct organic devices.[7] Another benefit of these cells is their high flexibility, in principle they can completely made out of polymers and small organic molecules. A much broader spectrum of possible applications are thinkable (e.g. on car roofs or notebook bags) than for the stiff silicon based devices.

Low efficiencies of about 10 % and an insufficient long-term stability avoid the break-through of OPVs.[8,9] One reason for the low device efficiency is a short diffusion length ($L_D$) of the excitation energy after photo-absorption in the organic material. This is caused by an extrinsic immobilization at grain boundaries or impurities and an intrinsic immobilization. The latter, which efficiency is material-specific, is based on a relaxation into so-called self-trapping states. An in-depth understanding of the underlying atomistic processes of self-trapping is necessary for the future development of materials with long $L_D$, in which intrinsic immobilization is prevented. The goal of this thesis is to make a contribution to such a mechanistic understanding of self-trapping of electronic excitations.

During this thesis exciton self-trapping was studied on the example of perylene based materials, because they are one of the most stable materials within the organic dyes and possess high electron-carrier mobilities as well as high absorbance.[10] Despite these favourable properties highly efficient perylene based solar cells were not reported yet. This deficiency is attributed to trapping states and for a further development of these organic materials the understanding of the basic processes of excitation energy transport and the corresponding self-trapping processes is crucial.

The thesis is built up in the following way. In chapter 2 an introduction into the scientific background is given. This covers a brief overview about organic solar cells and perylene based materials as well as an introduction into exciton transfer in organic materials and exciton self-trapping. In chapter 3 a digest about the computational methods used to calculate excited state properties is given. Then, computational approaches used within this thesis are explained in chapter 4. Atomistic models explaining exciton trapping in certain perylene based materials are presented in chapter 5. Afterwards, the introduced exciton self-trapping mechanisms are generalized to a wide range of perylene based materials (chapter 6) and a discussion of solvent effects is given (chapter 7). The thesis closes with a short summary in chapter 8.

# 2. Prolegomena

## 2.1 Organic solar cells

In the field of solar cells based on organic materials, three types of devices have to be distinguished (see Figure 2): Planar-heterojunction, bulk-heterojunction and dye-sensitized cells. The first two types work very similar. Absorption of light leads to a formation of an excited state, a bound electron-hole pair (exciton), in the organic dye material. The exciton can diffuse to a donor and acceptor interface, where charge separation is possible. By charge transport to the electrodes the conversion of light into electric power is completed.[11-14] These processes are discussed in more detail in the next subchapters. Dye-sensitized solar cells like the Grätzel cell work in a different manner.[15-18] A mesoporous inorganic semiconductor (IS) is in contact with the cathode. The IS is covered by a single layer of an organic dye. After photo-excitation of the dye, the dye is oxidized by electron transfer to the IS. Subsequent, a mediator, which is a redox species dissolved in the electrolyte, regenerates the dye by reduction. The electron at the IS is transferred to the electrode. Finally, the mediator is regenerated at the anode by electrons circulating through the external circuit.[16,19] This thesis deals topics concerning mainly planer- and bulk-heterojunction organic solar cells. Therefore, the rest of this chapter covers these types of devices.

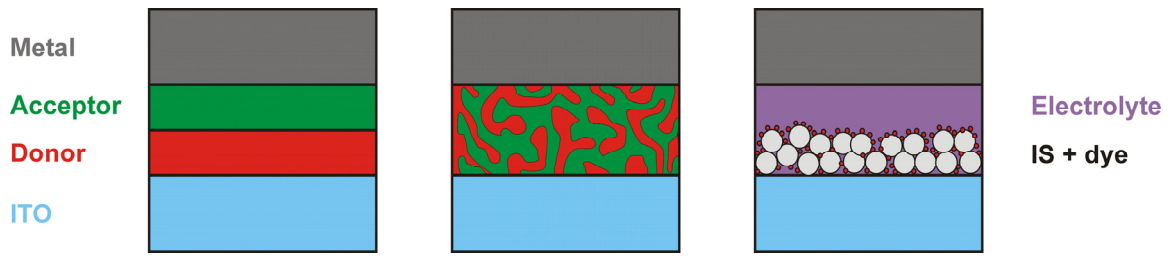


**Figure 2: From left to right: Planar-heterojunction, bulk-heterojunction and dye-sensitized solar cell. Planar-heterojunction cells are fabricated by sublimation of donor and acceptor organic materials on indium tin oxide (ITO) coated glass or on plastic substrates. Bulk-heterojunction cells are produced by spin-coating of a mixed solution of donor and acceptor materials or by co-sublimation on ITO. In the case of dye-sensitized cells, a mesoporous inorganic semiconductor (IS), e.g. $TiO_2$ or ZnO, is placed on ITO. The surface of the IS is covered with a single layer of organic dye molecules. An electrolyte is injected which contains a redox couple, e.g. $I_2$ and $I^-$.[10,16]**

### Performance of organic solar cells

The quality of organic cells is determined by the power conversion efficiency $\eta$, which is the ratio of the output power to the input power. The input power is given by the intensity and energy of the

incident light, while the output power is measured by the electric power of the device. Experimentally the cell efficiency is determined by so-called current density voltage (*J-V*) characteristics (see Figure 3 right). A compact overview about this topic is given in a recent article of Mishra et al.[20] An important parameter of the *J-V* characteristics is the open-circuit voltage ($V_{OC}$), which is the highest voltage delivered by a solar cell occurring at zero current density. It mainly depends on the materials, especially on the energy difference between the highest occupied molecular orbital (HOMO) level of the donor and the lowest unoccupied orbital (LUMO) level of the acceptor material (see Figure 3 left).

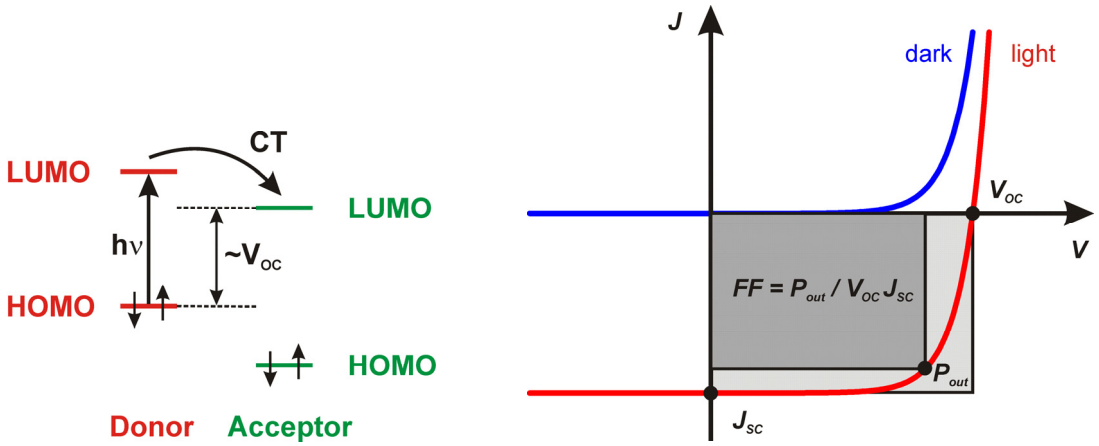


**Figure 3: Left: A simplified four level diagram of the alignment of the HOMO and LUMO levels of the donor (red) and acceptor (green) material in a bulk-heterojunction organic solar cell. Absorption (hv) at the donor material and charge-transfer (CT) to the acceptor material are schematically illustrated. Right: Current density voltage characteristics are shown for a solar cell. The device efficiency *η* is determined by the open-circuit voltage ($V_{OC}$), the short-circuit current density ($J_{SC}$) and the fill factor (*FF*). $P_{out}$ is the maximum power point, where the power output of the device has its maximum.[20]**

The short-circuit current density ($J_{SC}$) is the highest current density measurable in a solar cell. It depends on the number of absorbed photons and created free charge carriers as well as the charge mobility. Further influences are caused by the surface of the photo-active layer and the device thickness. A third parameter determining the cell efficiency is the fill factor (*FF*), which characterizes the device quality:

$$(1) \qquad FF = \frac{V_{P_{out}} \cdot J_{P_{out}}}{V_{OC} \cdot J_{SC}}$$

Here, $V_{P_{out}}$ and $J_{P_{out}}$ are the voltage and current density at the maximum power point $P_{out}$. The largest area within the *J-V* curve defines the *FF*. It depends on the number of generated charge carriers reaching the electrodes. Charge recombination and transport are mainly influencing the fill fac-

tor. It is necessary to have well matching energy levels of the materials to end up with high values for $V_{OC}$ and *FF*. The device efficiency is then given by ($P_{in}$: incoming power by sun light):[20]

$$(2) \qquad \eta = \frac{V_{OC} \cdot J_{SC} \cdot FF}{P_{in}}$$

In production one should ensure that an appropriate combination of materials as well as a good absorbance and solid state morphology are given.[21] Especially the latter is important to avoid losses by charge or exciton recombination. More details about these processes are given later.

**Shockley-Queisser limit**

A theoretical limit for the efficiency of a single *p*-*n*-junction solar cell (*p*: hole conductor; *n*: electron conductor) is given by the so-called Shockley-Queisser limit.[22] The starting point is the hypothesis that the band gap determines the energy of the photo-generated free charge carriers. After absorption, the excited electron rapidly loses all energy, till it reaches the energy of the bottom of the band. Out of the solar spectrum $f(\nu)$ only photons are absorbed, which are higher in energy than the band gap $E_g$($\nu$: frequency). A theoretical limit for the efficiency $\eta$ is given by the ratio of the energy of the generated free electrons $E_{e^-}$ divided by the energy of all photons $E_{h\nu}$:[22]

$$(3) \qquad \eta = \frac{E_{e^-}}{E_{h\nu}} = \frac{E_g \int_{E_g/h}^{\infty} d\nu f(\nu)}{\int_0^{\infty} d\nu f(\nu) h\nu}$$

Therefore, the theoretical limit for the energy conversion depends on the band gap. The best efficiency of 31 % can be found for a band gap of 1.3 eV under normalized sun illumination conditions.[23] For organic solar cells a maximal efficiency of 15 % is expected for a band gap of 1.5 eV.[24] One reason for the lower efficiency of organic devices is the required energy to separate the strongly bound charge carriers after excitation. In principle, so-called tandem cells, which contain several cells absorbing at different wavelengths, can beat this limit, because this is valid for each single cell of the composite.[25] For an organic tandem cell containing two sub-cells a best efficiency of more than 20 % is estimated for band gaps of 1.7 eV and 1.1 eV for the single cells.[24]

**Photo-current generation efficiency**

This subchapter concerns the overall energy conversion efficiency $\eta$ of organic solar cells and its limitations. $\eta$ can be expressed by the product of all single efficiencies of the steps occurring during

energy conversion: photo-absorption ($\eta_A$), exciton diffusion ($\eta_{ED}$), exciton dissociation ($\eta_{CT}$) and charge carrier collection ($\eta_{CC}$).[13]

$$\eta = \eta_A \cdot \eta_{ED} \cdot \eta_{CT} \cdot \eta_{CC} \quad (4)$$

In the following processes are discussed, which determine the efficiencies of each step during photo-current generation.

**Photo-absorption**

The first step for photo-current generation in organic solar cells is the photo-absorption. Best performing dyes should harvest photons from the solar irradiation with a high absorbance. The solar spectrum has the highest intensities in the range of 600 – 800 nm. However, absorption of the complete visible and near IR spectral range is desirable for organic dyes.[12,20] A band gap of 1.1 eV (1100 nm) between the highest occupied and lowest unoccupied band yields an absorption of 77 % of the solar spectrum (see Figure 3 left).[11,12] Most organic dyes possess band gaps of around 2 eV (620 nm), which reduces the amount of harvested photons to 30 %.[11,12] However, small band gap materials have a disadvantage. After absorption the electronically excited part of an aggregate relaxes into the equilibrium geometry, which minimizes the potential energy. This process leads to a loss of potential energy due to relaxation.[14] To improve the spectral absorbance tandem cells have been established.[26,27] Several cells are joined together in such devices. Each one of them contains a dye with an absorption maximum at a different wavelength. In principal, the whole solar spectrum can be covered this way.

Another problem is the absorption coefficient of organic materials which is in the order of $10^5$ $cm^{-1}$. This means that a 100 nm thick layer of organic dye is necessary to absorb photons efficiently.[11,12]

**Exciton diffusion**

In order to get free charge carriers the excitation energy has to diffuse to an interface of donor and acceptor material after photo-absorption. This process is called exciton diffusion. It is estimated that only 10 % of the photo-generated excitons lead to free charge carriers (in conjugated polymers).[12,28] In organic materials excitons are strongly bound electron-hole pairs (Frenkel excitons), which recombine within several nanoseconds. Typical diffusion lengths of 5 - 20 nm are observed, which is a very small distance compared to the required layer thickness for efficient absorption (100 nm).[11,12,20] Only excitons can be transformed into free charge carriers, which reach an interface

during diffusion.[20,28] As a consequence, concerning the layer thickness a compromise between efficient diffusion and absorbance is necessary. This problem can be solved by the use of bulk-heterojunction solar cells instead of simpler planar-heterojunction ones. In this device type thin layers, resulting from spin coating, co-sublimation or doctor blading of a fine mixture of donor and acceptor materials, take care for the small exciton diffusion length. A high absorbance can be achieved at the same time by choosing a proper overall thickness of the mixture layer.

**Charge separation**

At interfaces between donor and acceptor materials, excitons do not decay into free charge carriers spontaneously due to a huge binding energy.[20] An initial charge transfer process resulting in a polaron-pair occurs on a femtosecond time scale, and is much faster than other relaxation processes of the exciton.[29] Therefore, the charge transfer step has an efficiency of almost 100 %. The resulting polaron-pair can either recombine to the ground state or dissociate into free carriers via charge-separated states.[14] An additional driving force is necessary to separate the polaron-pair into free charges due to the large dissociation energy of about 0.1 eV.[20] The difference between the HOMO level of the donor material and the LUMO level of the acceptor material forms a gradient of the chemical potential at the interface (see Figure 3 left).[12] This internal electric field determines the open circuit voltage ($V_{OC}$) and causes a drift of charge carriers.[12] It was found empirically that an energy difference between the two levels of at least 0.3 – 0.4 eV is necessary for an efficient charge separation.[20] A second driving force results from different electrode materials, which yield an external electric field in short circuit conditions.[30] A third driving force is a concentration gradient of the charges which produces diffusion current.[12] Furthermore, the excess energy of a polaron-pair after exciton dissociation influences charge separation.[31] The additional energy helps to overcome the Coulomb attraction of the polaron-pair. Usually charge separation is very efficient.[32] However, if the same material transports electrons and holes, a charge recombination can affect the efficiency of the transport.[33] In the case of charge recombination two mechanisms are distinguished.[34,35] Geminate recombination is defined as between charges bound by Coulomb interaction after exciton dissociation. In organic solar cells this mechanism occurs on a picosecond to nanosecond timescale. A non-geminate process means a recombination of oppositely charged carriers originating from different excitons, which happens on a microsecond to millisecond timescale. These processes result in a lowering of $V_{OC}$.[36] Another problem is the low charge carrier mobility $\mu = \frac{v}{F}$ ($v$: velocity of charges; $F$: applied electric field), which is in the range of $10^{-8}$ – $10^{0}$ $cm^2V^{-1}s^{-1}$ for many organic materials (e.g. silicon has an electron mobility of $1.4 \cdot 10^{3}$ $cm^2V^{-1}s^{-1}$ at room temperature).[20,37-41] The low mobility in organic materials is caused by charge recombination processes and traps.[42,43]

**Charge collection**

The last step of the energy conversion is the extraction of the charge carriers at the electrodes. The materials have to be selected in a way that the energy levels are matching so that no energy gets lost.[12] Normally, this condition can be achieved. The charge extraction depends on the concentration of charge carriers at steady state conditions.[44] If the extraction rate of the charge carriers is low at the electrodes, they cannot leave the device fast enough. This results in the formation of a space charge region at the organic-metal interface, which limits the charge extraction process.[44]

Summarizing, the energy conversion efficiency especially of an flat-heterojunction organic solar cell is mainly limited by absorption and exciton diffusion:[13]

$$\eta \approx \eta_A \cdot \eta_{ED} \quad (5)$$

The efficiency of photo-absorption can be addressed by the used dye and the cell architecture. Therefore, exciton diffusion remains as one serious limitation for organic-solar cells, which limitations are scientifically not well understood. Exciton diffusion is discussed in more detail in the following chapter. Before doing so, the development of cell architectures of organic solar cells using small molecules or polymers is outlined in a short overview.

**Cell architectures**

The starting point of the development of organic solar cells was the discovery of the photovoltaic effect by Alexandre Edmond Becquerel in 1839.[45] But it took until 1954, when the first silicon based solar cell was reported.[46] In the 1970$^{th}$ the first organic devices were studied, but with very low device efficiencies. These cells were based on a single layer of dye material between two electrodes. For example Tang et al. built a cell with a microcrystalline film of chlorophyll and a device efficiency of 0.02 %.[47] The low efficiency is caused by the physics of organic semiconductors. In inorganic ones the absorption of light produces almost instantaneously free charge carriers due to the low binding energy of electrons and holes in so-called Wannier-Mott excitons (binding energies around 0.025 eV).[35] In contrast to this, in organic semiconductors Frenkel excitons are generated after photo-excitation, which possess a much higher binding energy between electron and hole. Typical binding energies are estimated to be in the order of 0.5 - 1.5 eV.[48] Free charge carriers are only produced if the binding energy can be overcome. In principal, this is possible by external electric fields or at certain interfaces as mentioned before.

In 1986 Tang introduced an organic planar-heterojunction cell (see Figure 2) by using copper phthalocyanine as electron donor and 3,4,9,10-perylene tetracarboxylic bisbenzimidazole (PTCBI) as acceptor material.[49] An improved device efficiency of ~1 % was measured. The bilayer structure of the device promotes a charge-transfer (CT) process between donor and acceptor material at the interface. The donor and acceptor materials must be chosen in a way that a dissociation of the exciton into free charge carriers happens efficiently.

Planar-heterojunction cells can be further improved by introducing an exciton blocking layer (EBL) between the acceptor material and the cathode. This layer reflects excitons, which significantly improves $J_{SC}$ by preventing excitons to be quenched at the metal electrode.[50,51] This works due to a large energy offset between the HOMOs and LUMOs of the acceptor material and the exciton blocking material.[52] Additionally, the EBL prevents hot metal atoms to penetrate into the acceptor material during deposition. A large energy offset between the EBL and the cathode is expected to occur which should form a barrier for electron transfer to the electrode. However, this is not observed which can be explained by gap states introduced during deposition of the cathode. This facilitates charge transport through the EBL.[50,51,53-55] The need for gap states limits the size of the EBL to about 10 nm.

Bilayer cells are still limited for their efficiency due to the small exciton diffusion length of organic materials, which is typically in the order of 5 - 20 nm.[11,12,20] Therefore, very thin layers are necessary, which reduces crucially the optical absorbance of the cells. Also this point is discussed in more detail later in this chapter. In 1991 Hiramoto et al. introduced bulk-heterojunction devices (see Figure 2).[56] A perfect bulk-heterojunction cell contains an interpenetrating mixture of donor and acceptor material in a way that all excitons are photo-generated within their diffusion length to an interface. Also, an exclusive contact of the donor material to the anode and of the acceptor material to the cathode is given. This building principle for organic solar cells circumvents the conflict between the short exciton diffusion length and low absorbance. However, this ideal case is still not achieved in existing devices.

In 2003 Forrest et al. introduced a revised bulk-heterojunction cell.[53-55] The device was structured as followed: A donor material is evaporated on an ITO electrode, then a donor and acceptor blend layer follows, finally an EBL and the cathode are deposed. An improvement of 40 % was achieved by this hybrid-heterojunction cell architecture. It is also called a *p*-i-*n* structure (*p*-conductor - intrinsic absorber - *n*-conductor), because an exclusively hole and an exclusively electron conducting layer sandwiches the active bulk-heterojunction one.[57] Efficient doping of the *p*- and *n*-layer enables ohmic contacts to the electrodes which supports charge collection. Mitsubishi Chemicals have constructed today's best bulk-heterojunction solar cell with a device efficiency of 9.2 %.[58]

The drawback of bulk-heterojunction devices are their complex structure caused by the mixture of two materials which could result in traps for charge loss if e.g. a material phase has no contact to the electrodes or domains becomes thicker than the exciton diffusion length. Therefore, a proper adjustment of morphology and phase separation is crucial for the efficiency of bulk-heterojunction solar cells.[20] Also, reproducibility is a problem in the manufacturing process of such devices.[59]

Several hierarchy levels must be taken into account to end up with a well performing device which is nicely outlined in a recent review article of F. Würthner and K. Meerholz.[60] The first one is the molecular level. On this level the donor and acceptor molecules must be optimized for their optical and redox properties. Both molecules should complement each other in absorption to cover large parts of the solar spectrum. The redox properties must be adjusted in a way that the HOMO and LUMO levels of both molecules allow a fast electron transfer at the interface (see Figure 3 left) while the $V_{OC}$ is large at the same time. The second hierarchy level is the super-molecular one (length scale of around 10 nm). For this level, proper phase separation of the donor and acceptor molecules as well as self-assembly of the aggregates must be considered. For the first topic it is important that the molecules prefer to build homo- instead of hetero-aggregates. Self-assembly is desired, because exciton and charge transport is more efficient in well-ordered aggregates with favorable packing motifs. The whole system represents the third level. A formation of optimal domains and paths for the charges is desired on a length scale of 100 nm. This level depicts a big challenge for device manufacture. A proper intermixing and macroscopic orientation of the material layers should be achieved. Time-consuming optimizations and try-and-error concepts must be employed to solve this issue properly. Variation of solvents, deposition technics and thermal post-treatment (“annealing”) is possible. The fourth level of hierarchy is the device one. Proper contacts of the bulk-heterojunction layers to the electrodes must be ensured. Additional EBLs help to solve this problem.

The absorption width of organic materials is typically narrow. Therefore, a single dye cannot cover the whole solar spectrum. To overcome this limitation so-called tandem cells are introduced in 2007 by the Heeger group.[26] In these cells different single-junction cells are stacked together. Each single cell absorbs at different wavelengths, which allows covering a large part of the solar spectrum. The best device efficiency of 10.7 % for an organic solar cell was measured in such a tandem solar cell.[9] Most common cell architectures are parallel and series connected cells.[61] In series connected tandem cells, the sub-cells share a common recombination layer between the stacks. The anode of the first cell is electrically connected to the cathode of the last cell. This electric connection results in a constant photo-current through the device and the single $V_{OC}$ of each cell add up. In a parallel connected setup the single cells share common electrodes. In this case the $V_{OC}$ of the tandem cell is given by the sub-cell with the lowest $V_{OC}$ and the $J_{SC}$ of each sub-cell sum up.

## 2.2 Perylene based materials

There are different organic materials employed in organic solar cells, for instance small molecules, oligomers or polymers.[62-66] Organic solar cells are classified by the used materials: Small molecule, polymer and organic-inorganic hybrid devices.[10] The latter means a combination of organic molecules with inorganic semiconductors like the Grätzel cell (see chapter 2.1). An alternative classification of organic photovoltaics can be done by the device structure: Planar-heterojunction, bulk-heterojunction and dye-sensitized cells (see Figure 2).[10,62]

Today's organic solar cells cannot compete with silicon-based ones and other thin-film photovoltaic devices in stability and efficiency.[6,10] For this reason, the investigation of new organic materials is required. These materials should fulfill efficiency conditions like light harvesting, charge transfer, charge and exciton transport, thermal-, chemical- and photo-stability.[10] 3,4,9,10-perylene tetracarboxylic bisimides (PBIs, see Figure 4) are one of the most stable materials within the organic dyes and possess high electron-carrier mobilities.[10,67] Their electron deficiency disfavors photo-oxidation, which is one major reason for their stability, and makes the material to one of the best organic n-type semiconductors known today.[68,69] PBIs belong to the family of rylene dyes and are well known as high-performance pigments applied in car paints or the coloration of synthetic fibers.[70-72] There is a huge variety of materials belonging to the sub-class of perylene based dyes resulting from the fact that perylene possesses twelve functionalizable positions. The 3,4,9,10 positions are known as *peri*-, the 1,6,7,12 are called *bay*- and the 2,5,8,11 are known as *ortho*-position (see left panel of Figure 4).[10]

The synthetic routes for most of the existing perylene bisimides start at the commercial available 3,4,9,10-perylene tetracarboxylic dianhydride (PTCDA). A simple imidization reaction using aliphatic or aromatic amines yields PBIs, which can be purified easily in high yields.[10] These *peri*-substituted perylenes constitute the 1$^{st}$ generation of PBI dyes. They are often used in planar heterojunction solar cells as acceptor materials (see Figure 2).[10] One famous PBI dye is the *N*,*N*'-dimethyl-perylene bisimide also known as "Pigment Red 179".[70,71] The color of the pigment dependents on the solid-state particle size and can be varied from maroon to red.[10] It is extensively used in industrial paints due to its rich deep color, high transparency, brightness and outstanding weather fastness.[10,70] The solubility of the 1$^{st}$ generation PBIs in different solvents can be adapted by bulky alkyl or aryl substituents at the imide groups.[73] In solution all these perylene dyes show similar absorption spectra, which proofs that the imide substituents do not affect the optical properties.[10,74,75]

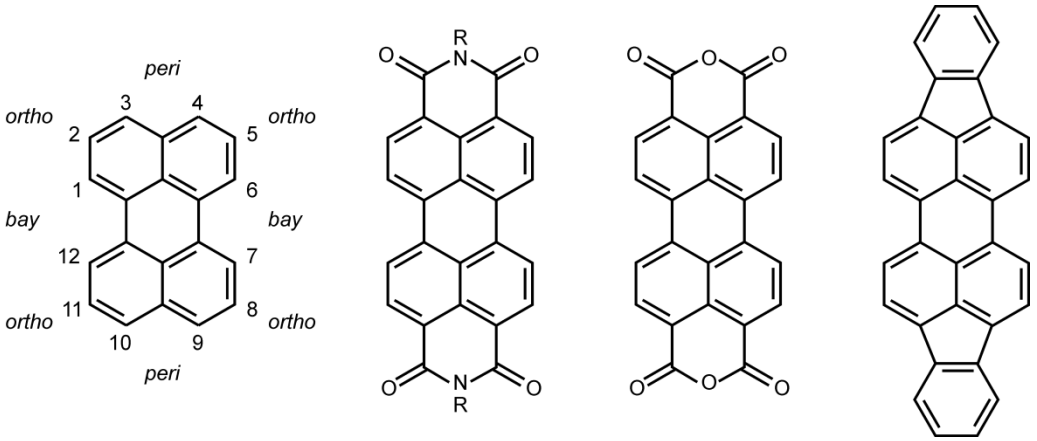


**Figure 4: Different perylene based dyes. The functionalizable positions of perylene are illustrated in the left panel. From left to right some examples for perylene based dyes: Perylene tetracarboxylic bisimide (PBI), perylene tetracarboxylic dianhydride (PTCDA) and diindeno perylene (DIP).**

Recently, another *peri*-substituted perylene has gained interest for application in optoelectronic organic devices: Diindeno perylene (DIP, see Figure 4). In single crystals an exciton diffusion length of 90 nm was measured in accordance with the crystalline grain size.[76] This value is one of the largest reported for organic materials. For example, in α-PTCDA a diffusion length of only 22 nm was published.[77] Well performing organic solar cells need a good calibration of the thickness of the exciton diffusion layer, in order to have a good balance between optical and electronic properties.[78] On one side thicker films yield a better light absorption, which leads to the generation of more excitons. But for small diffusion lengths less excitons reach an interface of donor and acceptor material. On the other side, in thin films the number of structural and chemical defects rises, which results in an effective exciton trapping besides the reduced amount of photo-generated excitons.[76] In conclusion, larger exciton diffusion length will lead to a better performance of organic solar cells, which is provided by DIP. Further benefits for this material are its strong tendency to self-order along the long molecular axis as well as its balanced charge carrier transport.[79,80] Finally, DIP possesses two polymorphs observed at low and high temperatures, respectively.[81] In thin films only the high-temperature phase is found.[81,82] This benefits to its application in organic solar cells, because thermally induced structural changes of the aggregate are prevented. However, there is one serious restraint for the application of DIP in organic solar cells. On weakly interacting substrates like $SiO_2$ or ITO the DIP molecules essentially stand upright (along the long molecular axis), which increases the intermolecular interactions between adjacent DIP molecules.[76,83,84] Since the vector of the transition dipole moments points towards the long molecular axis as well, DIP cannot absorb incoming light efficiently in thin films, because the wave vector of the incoming light is orthogonal oriented to vector of the transition dipole moment. For applications it is necessary to manipulate the orientation of DIP on weakly interacting surfaces to end up with efficient devices. One way to achieve this is to use amorphous films

instead of well-ordered ones. Unfortunately, the large exciton diffusion length in crystals is not found in the amorphous phase (9 nm).[85] Nevertheless, a planar heterojunction cell based on DIP was published with an device efficiency of 4.1 %.[86] A chemical derivatization could be a promising way to change the orientation behavior of DIP on weakly interacting surfaces.

In order to end up with materials with good performance it is insufficient to vary only the imide substituent, because only aggregation behavior and solubility can be adapted.[87] For modification of morphological properties as well as absorption, fluorescence and HOMO/LUMO energies, further variation of the substitution of the perylene is essential.[10] A common way to accomplish this is to halogenate PTCDA to end up with 1,6,7,12-tetrachloro- or 1,6(7)-dibromo-perylene tetracarboxylic anhydride.[88,89] A treatment with amines in an acidic solvent yields *bay*-halogenated PBIs.[90] Using nucleophilic aromatic substitution or metal-catalyzed reactions a variation of the *bay*-substituent can be reached.[87] These PBIs are called the 2$^{nd}$ generation. Often a phenoxylation is used to improve the solubility of the PBIs.[91-93] Compounds with four phenoxy groups in *bay*-position possess a bathochromic shift of more than 50 nm compared to unsubstituted PBIs but retain their high fluorescence quantum yield of almost one.[10] Dyes showing a hypsochromic shift could be synthesized as well.[94] Due to their improved solubility 2$^{nd}$ generation PBIs are used in solution-processed solar cells like bulk-heterojunction devices (see Figure 2) and organic field-effect transistors.[10,87,95,96] Unfortunately, the performance of solar cells with 2$^{nd}$ generation PBI remain behind fullerene-based devices.[10] Today, the power conversion efficiency of the best PBI cell is 3.17 %, while the best fullerene cell yields 8.3 %.[10,97] The main problem of the efficiency of PBI devices seems to be self-trapping of excitons in the domain of strongly aggregated PBI molecules.[10] Morphological control and arrangement of the molecules remains a crucial topic for research on PBIs.[10]

By functionalization in *bay*-position optical and electronic properties of PBIs can be tuned, but the resulting twist of the perylene core is weakening intermolecular interactions compared to the 1$^{st}$ generation PBIs.[10,87] Therefore, a possibility was investigated to adjust optical properties and retain the planarity of the molecule. One way to enable this was to use asymmetric perylene monoimides (PMIs).[98,99] They can be synthesized in a one-pot reaction by imidization and decarboxylation of PTCDA at high temperatures.[100] Afterwards, PMI can be monobrominated at *peri*-position or tribrominated at *peri*- and *bay*-position depending on the solvent.[10] Monobrominated PMIs react with certain naphthalene monoimids in basic conditions to terrylene bisimides, which have a larger aromatic core than PBIs.[98-100] Treating monobrominated PMIs with amines leads to push-pull type perylene dyes, which are used in dye-sensitized solar cells (see Figure 2).[10] The amine group acts as donor and the imide is an acceptor, which gives a bathochromic shifted absorption and strong intramolecular charge transfer. The latter favors high efficient dye-sensitized solar cells.[10] The best device

based on PMIs possesses an energy conversion efficiency of 6.8 %.[10,101] Strong dipole orientation towards the inorganic semiconductor enhances the electron injection and minimizes the charge re-combination.[10]

A recently developed functionalization of PBIs is at the *ortho*-position, which leads to the 3rd generation of PBI dyes.[102-105] These materials can be optimized without geometric distortion of the perylene core.[10] Higher solid-state fluorescence was yielded for these PBIs compared to the other generations, which results in improved energy conversion efficiencies of organic solar cells.[10,106]

## 2.3 Exciton transfer in organic materials

Chapter 2.1 outlined the fundamental processes which limit the efficiency of organic solar cells. Serious problems are morphology and absorbance, especially for bulk-heterojunction devices. For all types of organic solar cells, inefficient exciton diffusion represents a crucial limitation.[13,107-110] Despite their importance, trapping effects limiting exciton diffusion are still not fully understood. For exciton trapping two cases are distinguished: Extrinsic trapping happens at grain boundaries and structural or chemical impurities. Intrinsic trapping happens even in perfect crystals and result from relaxation processes leading to a local distortion of the crystal or aggregate structure. This phenomenon is called exciton self-trapping and is based on a strong lattice deformation, which immobilizes the exciton by its own lattice distortion field.[111-113] Self-trapping is a material specific property and has to be discussed accordingly. In the following, the fundamentals of exciton diffusion are discussed. In the next subchapter, exciton self-trapping is introduced more carefully.

**Regimes of excitation energy transfer**

The basic mechanism of exciton diffusion is the excitation energy transfer (EET) between molecules. Two time scales are important in order to describe this mechanism.[114] The first one is the intramolecular relaxation time $t_{rel}$, which describes the time each molecule needs to return to thermal equilibrium after an electronic transition. The other one is the transfer time $t_{trans}$, which is the time an exciton needs to move from one molecule to another. Both times define three regimes for exciton transfer. If $t_{rel} \ll t_{trans}$, intramolecular relaxation leads to fast dephasing of the exciton and results a localized so-called Frenkel exciton. Such an exciton is transferred incoherently, which causes a diffusive motion. The second regime for exciton transfer can be found for $t_{rel} \gg t_{trans}$. Here, the exciton moves almost freely from molecule to molecule.[114] A spatially confined wave packet must be considered, which is delocalized over many molecules, and a coherent transfer results. An intermediate cases ($t_{rel} \approx t_{trans}$) compose the third regime with partially coherent transfer.

**Förster and Dexter transfer**

Organic materials are mainly non-covalently bound complexes, where typically localized Frenkel excitons are found (first regime).[114] In this case EET could happen via two mechanisms (see Figure 5). The first possibility is a simultaneous de-excitation of one molecule and excitation of another molecule. This is called Förster resonant energy transfer (FRET).[115] The alternative process is described by electron exchange. Formally, the electron in the LUMO of the excited molecule is transferred to the LUMO of the molecule in the ground state. At the same time an electron from the HOMO of the mol-

ecule in the ground state is transferred to the HOMO of the excited molecule. This type of EET is the so-called Dexter transfer (see Figure 5). This process depends on the differential overlap of the LUMOs and HOMOs at both molecules, which decays exponentially with the distance.[116] As a result, Dexter transfer happens only for small spatial separations of the molecules, while Förster transfer occurs even for large distances.[114,116] More detailed discussions about EET can be found in the here cited literature.[114,116-118]

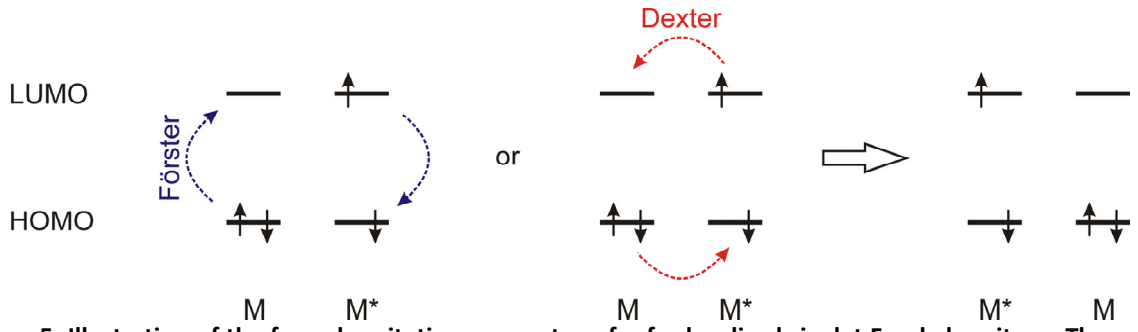


**Figure 5: Illustration of the formal excitation energy transfer for localized singlet Frenkel excitons. The excited molecule (M*) transfers the excitation energy to a molecule in the ground state (M). This happens either via Förster (blue) or Dexter (red) transfer.**

According to Fermi's golden rule, the exciton transfer rate $k_{EET}$ via EET is described by:[114]

$$k_{EET} = \frac{2\pi}{\hbar}|V_{ec}|^2 D_{EET} \quad (6)$$

In this equation, $V_{ec}$ denotes a Coulomb matrix element which does not depend on nuclear coordinates within the Condon approximation. Its meaning is outlined later in this subchapter. $D_{EET}$ describes the combined electronic and vibrational density of states (DOS) referring to the EET process:

$$D_{EET} = \hbar \int d\omega \, D_D^{(em)}(\omega) D_A^{(abs)}(\omega) \quad (7)$$

Here, $D_D^{(em)}(\omega)$ is the combined DOS for the donor de-excitation and $D_A^{(abs)}(\omega)$ the combined DOS for the acceptor excitation. $D_{EET}$ is called the spectral overlap expression, because it is determined by the frequency integral of the overlap expression of the donor and acceptor DOS.

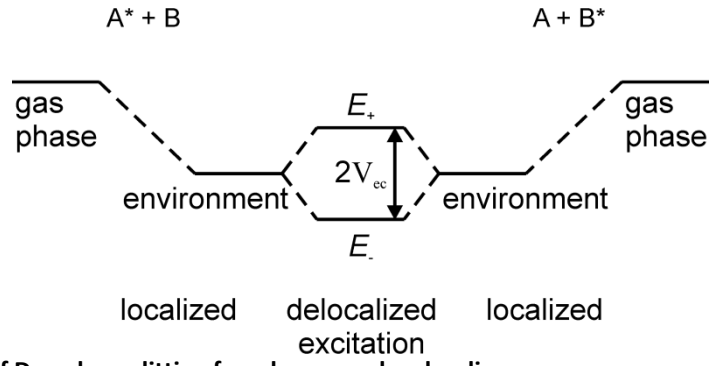


**Figure 6: Illustration of Davydov splitting for a homo-molecular dimer.**

If two molecules – A and B – are considered, $V_{ec}$ is the electronic part of the coupling between the situation where either A (A* + B) or B (A + B*) is excited. This coupling leads to a so-called Davydov-splitting of the excited states (see Figure 6).[117,119,120] In the following derivation of an expression for $V_{ec}$, it is assumed that both molecules have one occupied orbital $\phi_A$ and $\phi_B$ and one excited orbital $\phi_A^*$ and $\phi_B^*$. The ground state is given by

( 8 ) $$\psi_A = \left|\phi_A\bar{\phi}_A\phi_B\bar{\phi}_B\right\rangle$$

and locally excited configurations by:

( 9 ) $$\psi_A = \frac{1}{\sqrt{2}}\left(\left|\phi_A\bar{\phi}_A^*\phi_B\bar{\phi}_B\right\rangle + \left|\phi_A^*\bar{\phi}_A\phi_B\bar{\phi}_B\right\rangle\right)$$

( 10 ) $$\psi_B = \frac{1}{\sqrt{2}}\left(\left|\phi_A\bar{\phi}_A\phi_B\bar{\phi}_B^*\right\rangle + \left|\phi_A\bar{\phi}_A\phi_B^*\bar{\phi}_B\right\rangle\right)$$

The dimer wave function is than a linear combination of both local configurations:

( 11 ) $$\Psi = c_A\psi_A + c_B\psi_B$$

Inserting this wave function into the Schrödinger equation and projecting with the local solutions from the left yields:

( 12 ) $$\begin{pmatrix} H_{AA} & H_{BA} \\ H_{AB} & H_{BB} \end{pmatrix}\begin{pmatrix} c_A \\ c_B \end{pmatrix} = E\begin{pmatrix} 1 & S \\ S & 1 \end{pmatrix}\begin{pmatrix} c_A \\ c_B \end{pmatrix}$$

With:

( 13 ) $$H_{AA} = \left\langle\psi_A\middle|\hat{H}\middle|\psi_A\right\rangle$$

( 14 ) $H_{AB} = \langle \psi_A | \hat{H} | \psi_B \rangle$

( 15 ) $H_{BB} = \langle \psi_B | \hat{H} | \psi_B \rangle$

( 16 ) $S = \langle \psi_A | \psi_B \rangle$

In the case of a homo-dimer $H_{AA} = H_{BB}$ is valid and the following energies result:

( 17 ) $E_{\mp} = \frac{H_{AA} \mp H_{AB}}{1 \mp S} = H_{AA} \mp \frac{H_{AB} - S H_{AA}}{1 \mp S}$

If one assumes $S = 0$ which is valid for large intermolecular distances, the energy difference between $E_+$ and $E_-$ is determined solely by $H_{AB}$, which is now equal to $V_{ec}$. In the orbital basis $H_{AB}$ is expressed as:

( 18 ) $H_{AB} = 2(\phi_A^* \phi_A | \phi_B \phi_B^*) - (\phi_A^* \phi_B^* | \phi_B \phi_A)$

The latter term in ( 18 ) involves the overlap between orbitals at A and B and can be neglected. Only the first term remains, which is the Coulomb interaction determining Förster transfer. The second term describes the exchange interaction describing Dexter transfer. The orbital overlap increases exponentially with the shortening of the distance. As a result, Dexter transfer only becomes significant for short intermolecular distances. In this case $V_{ec}$ is equal to half of the energy splitting defined in ( 17 ).

**Marcus-Hush theory for exciton diffusion**

Diffusion of localized excitons can be described approximately within a hopping model, where the exciton is localized at one molecule and jumps to other molecules with a certain probability. This is equivalent to the Marcus-Hush theory, which is introduced in detail in the here cited literature.[117,121-123] In the Marcus theory, the hopping rate $k_{EET}$ for EET is given by the semi-classical rate ($k_B$: Boltzmann's constant; $T$: Temperature; $\Delta G°$: Difference of Gibbs free energy before and after the jump; $\lambda$: reorganization energy):[117]

( 19 ) $k_{EET} = \frac{|V_{ec}|^2}{\hbar} \sqrt{\frac{\pi}{\lambda k_B T}} \cdot \exp\left(-\frac{(\lambda + \Delta G°)^2}{4 \lambda k_B T}\right)$

This expression shows that the hopping probability depends to the second power on the electronic coupling element $V_{ec}$, which includes Förster and Dexter transfer. $V_{ec}$ is accessible computationally by

the calculation of the Frenkel states of the two molecules within a super-molecular approach. Other approaches are possible as well.[116] As Figure 6 indicates, the coupling is equal to half of the splitting of the Frenkel states of the dimer. If all necessary quantities ($V_{ec}$, $\Delta G^\circ$ and $\lambda$) are calculated, one can use the rates $k$ given by Marcus-Hush theory to model the exciton diffusion within a master equation, which may be solved analytically or numerically, or by a Monte Carlo approach.[124]

**Measurement of exciton diffusion**

In organic materials the exciton diffusion can be determined by measurement of (a) exciton-exciton annihilation, (b) microwave conductivity, (c) heterojunction photocurrent or (d) photoluminescence quenching.[59] This means that neither the diffusion constant $D$ nor the diffusion length $L_D$ is directly measureable and must be interpreted using directly measured quantities. Case (d) is the most common used method and will be discussed in more detail in the following. The decay of the photoluminescence is measured in thin layers of organic material with variable thickness.[125] The material is deposited on fused silica as well as on exciton quenching material (e. g. $TiO_2$).[125] The photoluminescence decays faster on $TiO_2$ than on fused silica, because excitons diffusing to the $TiO_2$-interface are quenched. Parameterized fits of the available measured data have to be analyzed in order to extract the exciton diffusion constant. The distribution of excitons $n(z,t)$ in a thin film of an organic material as a function of depth and time can be described by a one-dimensional diffusion equation ($n$: concentration of excitons):[125]

$$\frac{\partial n(z,t)}{\partial t} = D\frac{\partial^2 n(z,t)}{\partial z^2} - k(t)n(z,t) \quad (20)$$

The second term of equation ( 20 ) accounts for the limited lifetime of excitons due to photoluminescence. $k(t)$ is the decay rate of the photoluminescence in absence of a quenching material and $z$ denotes the vertical distance from a point in the thin film from the interface to the vacuum.[125] Two boundary conditions are necessary to solve this differential equation. The first one is the initial distribution of excitons $n(z,0)$. If reflection at the $TiO_2$-interface and interference can be neglected, according to Beer-Lambert law results ($\alpha$: absorption coefficient):[125]

$$n(z,0) = n(0,0)e^{-\alpha z} \quad (21)$$

If a perfect quencher is assumed, the second boundary condition is $n(L,t) = 0$, where $L$ is the thickness of the film.[125] This condition leads to an underestimation of diffusion, if the quencher is not perfect. The term $k(t)$ can be determined by the non-quenched sample on fused silica for each film

thickness. The diffusion constant $D$ can be fitted to the measured photoluminescence data. The exciton diffusion length $L_D$ is related to the diffusion constant $D$ and is typically in the order of several namometers ($\tau$: exciton lifetime):

( 22 ) $L_D = \sqrt{2D\tau}$

## 2.4 Exciton self-trapping

In crystals with a strong coupling of charge carriers to the lattice, electrons or holes can become self-trapped as a polaron in its own lattice distortion field.[126] Two kinds of self-trapped charge carriers have to be distinguished: Dielectric polarons, which result from Coulombic interaction of a charge and a deformable lattice,[126,127] and molecular polarons, which are caused by chemical bond formation.[128,129] In real systems both kinds are usually mixed. A bound electron hole-pair with a strong coupling to the crystal lattice is called a self-trapped exciton.[111] Here, the electronic excitation causes a strong local deformation of the lattice which leads to an immobilization of the exciton by its lattice distortion field. Self-trapped excitons can be characterized in the same way like the self-trapped charge carriers.[111] Most studies concern exciton self-trapping in inorganic crystals like ionic halide crystals[130-132] and in solid rare-gas crystals.[133-135] In other crystals the effect is only rarely reported. For this reason, it is convenient to introduce exciton self-trapping on the example of metal halides. Williams et al. wrote a nice review article about this topic.[111] In the ground state metal halides are built up by closed-shell rare-gas like ions which means that in the crystals Coulombic interactions are dominating rather than covalent bonding. Valence excitations break up the closed-shell conditions and make covalent bonding possible. Most common is a dimerization of near neighbors. Such chemical bonding in the excited state results in a strong lattice coupling which can trap the electronic excitation. The self-trapped state will not be formed instantaneously since the initial excitation is extended in band states. A thermal fluctuation of appropriate magnitude will lead to a quick localization of the exciton in a self-trapped state with molecular dimensions.[111,129] The same mechanism holds for self-trapping of holes and electrons as well.

**Exciton trapping in organic materials**

In metal halides, molecular self-trapping of excitons dominates due to the formation of covalent bonds which is not expected in organic materials. On one hand ππ*-excited states are usually more stable than excited covalent states in metal halides.[136] On the other hand in organic crystals dispersive interactions are dominating resulting in larger lattice distances than in metal halides, which further frustrates chemical bond formation between adjacent molecules. However, chemical reactions after photo-excitation are well known also for organic and bio-materials like photo-induced proton transfer to prevent radiation damage in DNA and proteins[137,138] or photo-induced isomerization of retinal for animal vision.[139,140] Organic materials used in solar cells are selected in a way that they are photo-stable and, thus, molecular self-trapping should be of minor importance in this case.[10]

The band structure of organic materials is much more complicated than the one of metal halides due to a larger number of close lying excited states and a stronger crystalline disorder. Furthermore, two different kinds of excited states have to be distinguished: Frenkel-type and charge-transfer (CT) states. In organic materials excitons belonging to both types were characterized in the literature. Time-resolved and temperature-dependent photoluminescence measurements were performed on columnar stacks of sexithiophene by Glowe et al.[141] Both species of excitons were identified: Self-trapped Frenkel-type excitons and dark CT excitons. Both are produced directly by photo-excitation. Initial photo-excitation of a free Frenkel exciton branches into a self-trapped exciton, which is localized to one molecule, and a CT exciton, in which the electron and the hole are localized on different sides of the stack. CT excitons are generated with ~5 % efficiency, because CT states are normally 0.2 - 0.3 eV above the Frenkel ones in aggregates of π-conjugated oligomers.[142] Branching is possible due to coupling (resonance) between Frenkel and CT states due to a large bandwidth of the Frenkel states, which embrace the CT states.[141] This leads to the conclusion that directly after photo-excitation the nature of the exciton in organic semiconductors is dominated by super-molecular couplings. The same conclusion can also gained from studies of the photo-excitation in films of *trans*-quinacridone by transient and quasi steady state photo-modulation techniques.[143] The initial Frenkel exciton relaxes within 5 ps into an excimeric state which possesses a mixed Frenkel and CT character. In this final excimeric state the exciton gets self-trapped.

In both cases exciton self-trapping happens through a relaxation into lower lying excited states in which the exciton is immobilized. This constitutes a third kind of self-trapping which is dominating in organic materials. Such exciton traps were also suggested by other recent experiments. Platt et al. reported that in thin film blends of functionalized anthradithiophene derivatives with $C_{60}$ the photoluminescence quantum yield is dramatically reduced due to a exciton transfer into dark trap states on a sub-200-ps time scale.[144] The energy migration into the trap states explains a measured Stokes shift in the photoluminescence spectrum of the studied amorphous films. It was stated that the presence of trap states in the bulk leads to exciton localization to four or five monomers. In another example, Jursenas et al. studied polycrystalline films of *N*,*N*-dimethylaminobenzylidene 1,3 indandione by femtosecond time-resolved luminescence and pump-probe absorption techniques.[145] An initial localization and thermalization of excitons was observed. The localization happens on a timescale less than 100 fs which results in a self-trapped exciton due to strong exciton-phonon coupling. A further decay of the self-trapped exciton possesses two non-radiative relaxation stages. The first one takes place with a time constant of 800 fs and is related to the final localization of the exciton. During the thermalization process an additional relaxation directly to the ground state via a conical intersection is possible. After localization the second stage appears which happens on a time scale of several

picoseconds to nanoseconds. It is assigned to the non-radiative decay of the relaxed self-trapped exciton resulting into lower excited states or by surface defects. A fast localization of the exciton on a few monomers after photo-excitation was reported in other materials as well.[146,147] In the case of conjugated polymer materials exciton self-trapping was also found due to a relaxation into lower lying states. Chang et al. studied the exciton evolution in thin films of a conjugated polymer by time-resolved photo-luminescence measurements.[148] The initial exciton is delocalized over more than one chain. Due to interchain interactions an intermolecular relaxation occurs into a lower electronic state within less than 50 fs which precedes EET.[148,149] This results an ultrafast redshift of the emission and a rotation of the transition dipole moment. In another study, Traub et al. identified energetically low lying trap states by single molecule and single aggregate spectroscopy.[150] These low energy traps could be due to electronic coupling or conformational change in the geometry of the polymer chains. However, interchain interactions introduce new states in polymeric materials which potentially dominate the photo-physics in the bulk.[151] This interpretation is supported by Athanasopoulos et al., who were only able to reproduce measured exciton diffusion lengths by Monte-Carlo simulations if they consider a concentration of 0.5 % trap states.[152] They suggested traps as domains with a higher crystalline order. A transfer into these domains is likely possible but a leaving is not due to an energetic relaxation to the bottom of the exciton band within the domain.

Extrinsic exciton trapping at grain boundaries or impurities can limit exciton diffusion as well as intrinsic self-trapping. Extrinsic trapping is affected by the degree of order in the bulk and increased exciton diffusion lengths were reported in highly ordered films. Bolinger et al. proposed a long ranged energy transfer in highly ordered single polymer nano-domains by using an electro-optical single-molecule spectroscopy imaging technique.[153] Such single polymer chains contain only few to none energetically low lying states which act as efficient traps in bulk materials.[154] In the case of zinc phthalocyanine, Yang et al. produced thin films by using a weak epitaxy growth technology which enables them to produce single-crystal like films.[155] In comparison to films grown under normal conditions, they found an improved charge carrier transport and exciton diffusion in the higher ordered films. The exciton diffusion length increases from 9 nm in normal films to 16 nm in single-crystal like films due to a higher density of extrinsic traps (e.g. structural defects) in the normal films. An influence on the crystalline order on the exciton diffusion length was also found for PTCDA by Lunt et al.[77] With increasing crystallite size the exciton diffusion length rises nearly fourfold from 6.5 nm to 21.5 nm. Exciton trapping at grain boundaries was figured out as one limitation for exciton diffusion. However, the diffusion length is significantly smaller as the averaged crystallite size of 2 µm, which indicates that intrinsic self-trapping plays a crucial role as well.

In summary, in organic materials two kinds of exciton trapping are dominant according to the recent literature. First, extrinsic trapping occurs at grain boundaries or impurities which can be addressed by forcing a high degree of order in the solid state. Second, self-trapping happens at energetically low lying states which are caused by intrinsic properties of the used material. The following part of this subchapter concerns such self-trapping in the case of perylene based materials which are in the focus of this thesis.

**Exciton self-trapping in perylene based materials**

In the following recent literature is introduced about exciton self-trapping in perylene based materials. One of the best explored materials is crystalline perylene. Two polymorphs of perylene exist: α-perylene with a dimeric packing motif and β-perylene which is build up by monomers (see Figure 7).[156,157] In α-perylene the dimeric perylene molecules are separated by 3.47 Å, whereas the dimers are separated by more than 10 Å. In β-perylene the closest distances between the centers of two molecules are 5.88 Å and 6.36 Å.

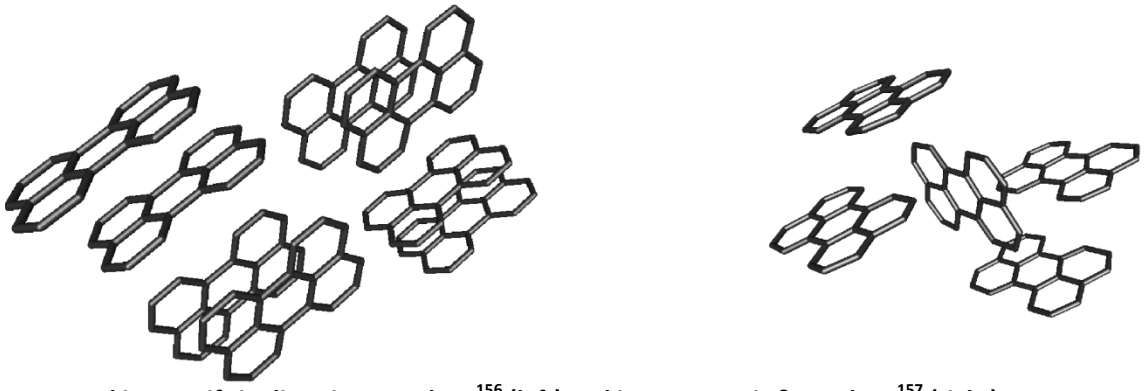

**Figure 7: Packing motifs in dimeric α-perylene[156] (left) and in monomeric β-perylene[157] (right).**

In the case of α-perylene it is well-known that the excitation localizes on a dimer on a sub-picosecond time scale.[158-164] West et al. studied the dynamics of the relaxation with non-linear optical spectroscopy.[158] Before self-trapping takes place, the exciton is delocalized over up to 16 monomers. During self-trapping the exciton localizes to an excimeric state on a dimer. By interpreting results from stimulated Raman spectroscopy, it was suggested that self-trapping happens via a shift motion of two molecules along the inter-dimer axis which significantly decreases the intermolecular distance. A gradient for this motion was identified in the Franck-Condon region. Furube et al. found out that about 80 % of the excimeric states are populated within less than 100 fs.[163] The remaining 20 % are generated more slowly with a time constant of 2 ps. This implies that population transfer into the self-trapped state occurs over two pathways with different time scales: First, it results by ultrafast

self-trapping and, second, by slower extrinsic trapping at defects of the crystal structure. The exciton is stabilized in the self-trapped state by 0.08 eV and possesses a long fluorescence life time of 110 ns. A slow diffusive motion of the self-trapped exciton is expected due to strong interactions of the exciton with the crystal lattice.[162,163] In fact the exciton-exciton annihilation rate is reduced by a factor of 50 compared to the monomeric β-perylene.[163] In β-perylene the exciton loses only 0.01 eV due to relaxation, which indicates a weak interaction with the crystal lattice. An almost free exciton motion and a high diffusion length are expected. Accordingly, self-trapped excitons are generated with a rate of only $7 \cdot 10^{10}$ $s^{-1}$ (corresponds to 14 ps).[162] This slow process could indicate rather extrinsic trapping than self-trapping.

In the literature exciton trapping was also figured out as a considerable limitation for internal quantum efficiency of PBI based solar cells.[147,165,166] Experiments of Howard et al. were performed with organic solar cells, where PBI is used as a finely dispersed acceptor material.[147] If the blend becomes coarser, the excitons relax in the time scale of 100 ps into a stable intermolecular state, which immobilizes the exciton and, therefore, frustrates charge transfer at donor/acceptor interfaces. It was proposed that 97 % of all photo-excitations get self-trapped. It was estimated that the exciton jumps just five times before relaxation occurs into a self-trapped state. With the help of transient absorption kinetics it was found that the dynamic of the relaxation is bimolecular. The relaxation into this intermolecular trapping state is a terminal loss mechanism for solar cells with aggregates of PBI molecules. Howard et al. determine a reduction of the internal quantum efficiency by about 20 %.

In another study, Graaf et al. characterized emission spectra of thin films of a bay-substituted PBI derivative (see chapter 2.2 for a discussion of PBI derivatives).[165] In condensed phase they observed emission from the monomer and from a red-shifted state. The red-shifted state is populated via a monomeric state because of similar rising and decay times. Temperature dependent measurements reveal an activation energy of 60 meV for its population. The state was indicated as a trap state for exciton diffusion and was referred to rare irregularities in the material due to its low intensity. An assured characterization of the extrinsic trap was not possible.

Schlosser et al. found an ultrafast Förster transfer between PBI molecules in a polymethyl methacrylate film.[166] Per transfer step the exciton is transferred over 2.3 nm within 1.5 ps, which results in a high mobility of excitons. Additionally, it was observed that excitons move to PBI dimers, which act as traps. This reduces the exciton diffusion length to 7 nm, which corresponds to 10 transfer steps. If the dimer formation could be suppressed, a diffusion length of around 120 nm is expected, which is comparable to the typical thickness of layers used in organic devices.

Recently it was found that the functionalization of PBI has an influence on the energy conversion efficiency of solar cells.[106,167] An increased open-circuit voltage is found for derivatives with larger

substituents.[167] Kamm et al. improved the device efficiency by a factor of two in varying the substitution on PBI.[106] This was possible by introducing an alkyl-chain on *ortho*-position (see chapter 2.2 for a discussion of derivatives of PBI). The lifetime of the excited state as well as its emission wavelength are influenced by the substituents on the PBI.[106] Based on these observations, Kamm et al. deduced that the photo-physics of PBIs is determined by the substituents, because they alter the packing motifs in the solid phase.

Reliable atomistic insight into exciton self-trapping can only be provided if a clear correlation between exciton self-trapping and aggregate structure is known. Fink et al. managed to explain the absorption and emission spectra of helical PBI aggregates in cyclohexane by dimer calculations in combination with a time-dependent Hartree-Fock (TD-HF) approach.[168] They could assign the absorption band of PBI aggregates at around 480 nm to the population of the second electronic state which has predominantly Frenkel character. The strongly red shifted and broad emission band results from photoemission out of the lowest Frenkel state. The broadness of the emission band originates from the potential energy surface (PES) topology of the final state. Its lifetime is long since it shows a nearly vanishing transition dipole probability with respect to the ground state. Thus, the lowest Frenkel state serves as a self-trapping state for the excitonic energy and its population limits the exciton transfer efficiency. These investigations essentially explained the spectra, but they were inappropriate to provide an understanding of the transition between the two excited states. Such an understanding is necessary to achieve an atomistic insight into exciton self-trapping. Such knowledge is important for a rational design of improved materials.

# 3. Theoretical principles

To determine properties of electronically excited states becomes a more and more important topic in computational chemistry. Theoretical methods can help to explain and to interpret experimental spectra or characterize optically dark states, which are not accessible without further effort by spectroscopy. Such states are important for example in light harvesting complexes.

Methods for excited states (in the scope of this thesis, this phrase means always electronically excited states) can be separated into two classes: wave function and electron density functional based methods. Former can be distinguished between methods determining the wave function of the excited state (MRCI, CASSCF, CIS, CISD, symmetry-adapted cluster [SAC] CI) and ones based on the polarization propagator (algebraic diagrammatic construction [ADC], $2^{nd}$-order polarization propagator approximation [SOPPA], equation of motion [EOM] CC, linear response [LR] CC, time-dependent HF [TDHF]). Furthermore, there exist methods which are approximations to the listed ones like CC2 or CIS($D_\infty$). To the class of electron density functional based methods belongs the linear response method time-dependent density functional theory (TDDFT). In this chapter only the basics of a few of these methods are discussed. At the beginning the first order methods CIS, TDHF and TDDFT will be introduced. Afterwards the second order correlation methods CC2 and ADC(2) will be presented.

The basis of most of the methods presented in this chapter is linear response theory (TDHF, TDDFT and CC2). It describes time-dependent processes in a system influenced by a weak oscillating electric field like one-photon absorption and emission. Therefore, a brief introduction into linear response theory for an exact state will be presented before introducing computational methods.

## 3.1 A brief introduction into linear response theory

The response theory for an exact state is presented in the following. A molecular system is described by a time-independent Hamiltonian $H_0$ and the time-depending interaction operator $V(t)$ acts on the system. It is assumed that $V(t)$ disappears for $t \to -\infty$. The fluctuation potential is expressed by its Fourier transformed:[169]

( 23 ) $$V(t) = \int_{-\infty}^{\infty} d\omega \tilde{V}(\omega) e^{(-i\omega+\alpha)t}$$

Here, $\alpha$ is a real positive infinitesimal (larger than zero but smaller than the smallest positive real) number. This expression for the interaction operator is often called adiabatically switched on perturbation.[169] $V(t)$ is a Hermitian operator $V(t) = V^*(t)$. Next, it is assumed that the eigenvalues of $H_0$ are known and at $t \to -\infty$ the system is described by:

( 24 ) $$H_0|\psi\rangle = E_0|\psi\rangle$$

$|\psi\rangle$ can be developed in the eigenstates $|n\rangle$ of $H_0$. For each eigenvalue $E_n$ the following is valid:

( 25 ) $$H_0|n\rangle = E_n|n\rangle$$

The time-dependence of the system is formulated by the time-dependent Schrödinger equation:

( 26 ) $$i\frac{d}{dt}|\psi(t)\rangle = \big(H_0 + V(t)\big)|\psi(t)\rangle$$

At time $t$ the perturbed wave function $|\psi(t)\rangle$ can be expressed by a perturbation series:[170]

( 27 ) $$|\psi(t)\rangle = |\psi\rangle + \int_{-\infty}^{\infty} d\omega_1 \big|\tilde{\psi}^{(1)}(\omega_1)\rangle e^{(-i\omega_1+\alpha)t} + \int_{-\infty}^{\infty}\int_{-\infty}^{\infty} d\omega_1 d\omega_2 \big|\tilde{\psi}^{(2)}(\omega_1,\omega_2)\rangle e^{(-i(\omega_1+\omega_2)+2\alpha)t} + \dots$$

Now, $\big|\tilde{\psi}^{(1)}(\omega)\rangle$ contains all terms, which depend linearly on the perturbation $V(t)$, and $\big|\tilde{\psi}^{(2)}(\omega_1,\omega_2)\rangle$ all terms, which depend to the second power on it. The correction of the wave function is not the most interesting part of dynamical process. It is more important to obtain information

on the change of an observable (expressed by an expectation value) during time. The time-dependence of the expectation value of an arbitrary operator $A$ is given by a Taylor series:

( 28 )

$$\langle\psi(t)|A|\psi(t)\rangle = \langle\psi|A|\psi\rangle + \int_{-\infty}^{\infty} d\omega_1 e^{(-i\omega_1+\alpha)t}\left[\langle\tilde{\psi}^{(1)}(-\omega_1)\big|A\big|\psi\rangle + \langle\psi\big|A\big|\tilde{\psi}^{(1)}(\omega_1)\rangle\right] + \frac{1}{2}\int_{-\infty}^{\infty}\int_{-\infty}^{\infty} d\omega_1 d\omega_2 e^{(-i(\omega_1+\omega_2)+2\alpha)t}\,\langle\tilde{\psi}^{(1)}(-\omega_1)\big|A\big|\tilde{\psi}^{(1)}(\omega_2)\rangle + \langle\tilde{\psi}^{(1)}(-\omega_2)\big|A\big|\tilde{\psi}^{(1)}(\omega_1)\rangle + \cdots$$

The first term of expression ( 28 ) describes the expectation value of the unperturbed system. The second term is the linear response function and contains all terms depending linearly on the time-dependent perturbation. All following terms belong to the quadratic and higher order response functions. The collection of terms done in the last formula is only possible, because the response function is symmetric with respect to the simultaneous interchange of the frequency $\omega$ and the operator $e^{(-i\omega_1+\alpha)t}$.[170] At this point it becomes clear why the positive infinitesimal $\alpha$ is important. It insures that only the unperturbed terms survive for $t \to -\infty$. In literature often an abbreviated form of the linear response function is used:

( 29 ) $$\langle\langle A; \tilde{V}(\omega_1)\rangle\rangle_{\omega_1} = \langle\tilde{\psi}^{(1)}(-\omega_1)\big|A\big|\psi\rangle + \langle\psi\big|A\big|\tilde{\psi}^{(1)}(\omega_1)\rangle$$

The linear response of a system contains solely one-photon transitions (absorption and emission). Two-photon transitions are described by the quadratic response $\langle\langle A; \tilde{V}(\omega_1), \tilde{V}(\omega_2)\rangle\rangle_{\omega_1,\omega_2}$ and so on.

The expressions for the perturbation of the wave function $|\psi^{(i)}\rangle$ can be determined by the Ehrenfest theorem for all orders. The derivation of the explicit formula for the linear response theory goes beyond the scope of this thesis and is carefully described in the literature of J. Olsen und P. Jørgensen.[170,171] Finally, one finds for the linear response function:

( 30 ) $$\langle\langle A; \tilde{V}(\omega)\rangle\rangle_{\omega} = \sum_{n\neq 0}\frac{\langle\psi|A|n\rangle\langle n|\tilde{V}(\omega)|\psi\rangle}{\omega-(E_n-E_0)} - \sum_{n\neq 0}\frac{\langle\psi|\tilde{V}(\omega)|n\rangle\langle n|A|\psi\rangle}{\omega+(E_n-E_0)}$$

As mentioned before, $|n\rangle$ are eigenstates of the unperturbed system according to $H_0|n\rangle = E_n|n\rangle$. The choice of the operator $A$ depends on the questioned observable. In the case of electronically excited states it is the transition dipole moment. For example dynamic polarizabilities can be calcu-

lated analogously. $\tilde{V}(\omega)$ describes the electromagnetic field at the frequency $\omega$ according to $\tilde{V}(\omega) = f\left(e^{i\omega t} + e^{-i\omega t}\right)$. Here, $f$ is the amplitude of the field.

The linear response function of the transition dipole moment has poles at the frequencies equal plus and minus the excitation energies of the unperturbed system:[170]

$$(31)\quad \lim_{\omega\to\omega_k}(\omega-\omega_k)\,\langle\langle A;\tilde{V}(\omega)\rangle\rangle_\omega = \langle\psi|A|k\rangle\langle k|\tilde{V}(\omega)|\psi\rangle$$
$$\lim_{\omega\to\omega_k}(\omega+\omega_k)\,\langle\langle A;\tilde{V}(\omega)\rangle\rangle_\omega = -\langle\psi|\tilde{V}(\omega)|k\rangle\langle k|A|\psi\rangle$$

The excitation energy is given by $\omega_k = E_k - E_0$. Consequently, the linear response function contains all information about the excitation energies of the unperturbed reference state $|\psi\rangle$ and the corresponding elements of the transition matrix. Higher order response functions yield the same information for multi-photon processes.

## 3.2 Configuration Interaction Singles (CIS)

The simplest method to determine excited states is the so-called Δ-method.[172] A ground state method with constraints is used to determine the excited state. The constraints are necessary to prevent the calculation from collapsing to the ground state. The first excited triplet state can be approximated by the triplet ground state. The lowest excited state of each irreducible representation can be calculated by adapting the symmetry of the ground state wave function. The use of the Δ-method is restricted due to the accessible excited states. Furthermore, excited states are often described by more than one configuration, which is not covered by this method. Therefore, more advanced methods are necessary like the ones introduced in the following.

After the Δ-method the next simplest approach is CIS. The derivation of the method starts with the insertion of the CIS wave function $\Psi_{CIS} = \sum_{ia} c_i^a \Phi_i^a$ ($\Phi_i^a$: singly excited configuration out of the HF determinant) into the time-independent Schrödinger equation:

( 32 ) $$H|\Psi_{CIS}\rangle = E_{CIS}|\Psi_{CIS}\rangle$$
$$H|\sum_{ia} c_i^a \Phi_i^a\rangle = E_{CIS}|\sum_{ia} c_i^a \Phi_i^a\rangle$$

By projection onto the space of singly excited determinants one gets, if $\{\Phi_i^a\}$ is a complete orthonormal set:

( 33 ) $$\sum_{ia}\langle\Phi_j^b|H|\Phi_i^a\rangle c_i^a = E_{CIS}\sum_{ia}\langle\Phi_j^b|\Phi_i^a\rangle c_i^a = E_{CIS}\sum_{ia}\delta_{ij}\delta_{ab}c_i^a$$

With the use of the following Slater-Condon rule one obtains ($\varepsilon_a$, $\varepsilon_i$: energies of the occupied and empty orbitals, $\mathrm{E}_0$: Hartree-Fock energy):[173]

( 34 ) $$\langle\Phi_j^b|H|\Phi_i^a\rangle = (\mathrm{E}_0 + \varepsilon_a - \varepsilon_i)\delta_{ij}\delta_{ab} + (ia||jb)$$

Here, an unusual definition for $(ia||jb)$ is employed:

( 35 )
$$(ia||jb) = \int\int \phi_i(\vec{r}_1)\phi_a(\vec{r}_1)\frac{1}{r_{12}}\phi_j(\vec{r}_2)\phi_b(\vec{r}_2)dr_1dr_2 - \int\int \phi_i(\vec{r}_1)\phi_j(\vec{r}_1)\frac{1}{r_{12}}\phi_a(\vec{r}_2)\phi_b(\vec{r}_2)dr_1dr_2$$

After insertion one gets the excitation energy $\omega_{CIS}$:

( 36 ) $\sum_{ia}\left[(\varepsilon_a - \varepsilon_i)\delta_{ij}\delta_{ab} + (ia||jb)\right]c_i^a = (E_{CIS} - E_0)\sum_{ia}\delta_{ij}\delta_{ab}c_i^a = \omega_{CIS}\sum_{ia}\delta_{ij}\delta_{ab}c_i^a$

This term can be converted into a matrix form. The used nomenclature will be helpful in the derivation of TDHF (see chapter 3.3).

( 37 ) $AX = \omega X$ with: $A_{ia,jb} = (\varepsilon_a - \varepsilon_i)\delta_{ij}\delta_{ab} + (ia||jb)$ and $X_{ia} = c_i^a$

The excitation energies $\omega$ are obtained by diagonalization of the matrix $A$. The wave function of the excited states belongs to the corresponding eigenvectors $X$. Their coefficients have to be applied to the HF reference. Furthermore, CIS is a method developed primarily for the ground state, which delivers only the Hartree-Fock solution for the ground state due to Brillouin's theorem. But it has strengths for excited states, because of its variational character. Due to the Rayligh-Ritz principle CIS delivers an upper limit to the exact energy of the ground and excited states. Furthermore, it is the only truncated CI method which is size-consistent. CIS yields pure singlet and triplet states for closed shell systems and the wave functions of ground and excited states are directly comparable. This is crucial if one is interested in transitions between states. Finally, there are analytic expressions for the state energies. An efficient differentiation after external parameters is possible and e.g. structure optimizations are available.

Overall, CIS overestimates excitation energies by 0.5 to 2 eV in comparison to experiments.[172] This is caused by the fact that the singly excited determinants yielded from the HF ground state are only a rough approximation to the excitation energy. The leading term in the matrix A is the difference in the orbital energies $(\varepsilon_a - \varepsilon_i)$, which normally is a rough approximation to the excitation energy. The energies of the empty orbitals are defined for the (*N*+1) instead of the *N* electron system within HF theory. Another reason for the failure of CIS is the complete neglect of electron correlation, according to Brillouin's theorem. Finally, CIS does not fulfill the Thomas-Reiche-Kuhn sum rule, which says that the sum of the oscillator strengths of all transitions is equal to the number of electrons. Therefore, oscillator strength or transition dipole moments calculated by CIS are only qualitatively correct.[172]

Overall, CIS is a valuable method especially for large molecules due to its favorable scaling behavior. It scales to the second power with the number of excited states and by $O(n^4)$ with the number $n$ of basis functions. By using of the resolution of identity approximation (RI)[174] a scaling behavior of $O(n^3)$ can be reached. On a standard computer it is possible to calculate excited states of molecules with up to 300 atoms and 5000 basis functions.[172]

## 3.3 Time-dependent Hartree-Fock theory (TDHF)

The starting point of TDHF is to consider the perturbation of a single Slater determinant (equivalent to the HF approach) in a general time-dependent potential $V(t)$. Plugging in the time-dependent Schrödinger equation $H(t)\Psi(t) = \mathrm{i}\frac{\partial}{\partial \mathrm{t}}\Psi(t)$ delivers:

( 38 ) $F(t)\Phi(t) = \big(F + V(t)\big)\Phi(t) = \mathrm{i}\frac{\partial}{\partial t}\Phi(t)$

$F$ corresponds to the time-dependent Fock operator, which follows from the HF approach. $V(t)$ could be an external time-dependent electric field for example. At time $t = 0$ a molecular system is in a stationary state, which can be described by a single determinant. Following, the time-independent HF equation is utilized and a fluctuation potential is applied which varies the HF orbitals only slightly. Now the time-dependent perturbation theory first order is applicable, which considers the linear response of the orbitals and the Fock operator. The time-dependent fluctuation potential itself as well as the linear response of the Coulomb and exchange operators to the change of the orbitals is included.

A depict derivation of the TDHF equations is possible by the density matrix formalism. The density matrix $P_{pq}$ depends on the electron density $\rho$ by (*p*, *q*, *r*: orbital indexes, $\chi$: time-independent orbitals):

( 39 ) $\rho(t) = \sum_{pq}^{M} c_p(t)c_q^*(t)\chi_p\chi_q^* = \sum_{pq}^{M} P_{pq}\chi_p\chi_q^*$

The Roothaan-Hall equation $FC = \varepsilon SC$ in an orthonormal basis ($S = 0$) can be reformulated using the density matrix. Now the time-independent density matrix is idempotent:[175]

( 40 ) $PP = \big(CC^\dagger\big)\big(CC^\dagger\big) = C\underline{1}C^\dagger = CC^\dagger = P$ or: $P^2 = P$

By expansion from the right by $C^\dagger$ and the Hermitian tronsposed term from the left, one gets (*F* is hermitian):

( 41 ) $FC = \varepsilon C$ $\quad (FC)^\dagger = (\varepsilon C)^\dagger$

$C^\dagger F = \varepsilon C^\dagger$

$FCC^\dagger = \varepsilon CC^\dagger$ $\quad CC^\dagger F = \varepsilon CC^\dagger$

$$FP = \varepsilon P \qquad\qquad PF = \varepsilon P$$

By subtracting both expressions one ends up with:

( 42 ) $$FP - PF = 0$$

Hence, the time-independent Fock and density matrix commute. An analogue reformulation is possible for the time-dependent HF equation in an orthonormal basis as well:

( 43 ) $$\left(F - i\frac{\partial}{\partial t}\right)C = \varepsilon C \qquad\qquad \left[\left(F - i\frac{\partial}{\partial t}\right)C\right]^{\dagger} = (\varepsilon C)^{\dagger}$$

$$C^{\dagger}F + i\frac{\partial}{\partial t}C^{\dagger} = \varepsilon C^{\dagger}$$

$$FCC^{\dagger} - i\left(\frac{\partial}{\partial t}C\right)C^{\dagger} = \varepsilon CC^{\dagger} \qquad\qquad CC^{\dagger}F + iC\left(\frac{\partial}{\partial t}C^{\dagger}\right) = \varepsilon CC^{\dagger}$$

$$FP - i\left(\frac{\partial}{\partial t}C\right)C^{\dagger} = \varepsilon P \qquad\qquad PF + iC\left(\frac{\partial}{\partial t}C^{\dagger}\right) = \varepsilon P$$

After subtraction of the Hermitian transposed expressions one yields by using of the time derivative of the density matrix:

( 44 ) $$FP - PF = i\left(\frac{\partial}{\partial t}C\right)C^{\dagger} + iC\left(\frac{\partial}{\partial t}C^{\dagger}\right) = i\frac{\partial}{\partial t}P$$

$$\sum_q \left(F_{pq}P_{qr} - P_{pq}F_{qr}\right) = i\frac{\partial}{\partial t}P_{pr}$$

This is the von Neumann equation for HF. In the basis of the orthonormal HF orbitals the following is valid for the unperturbed Fock $F^{(0)}$ and density matrix $P^{(0)}$ (*i*, *j*: indexes of occupied orbitals; *a*, *b*: indexes of empty orbitals):

( 45 ) $$F_{pq}^{(0)} = \delta_{pq}\varepsilon_p$$

$$P_{ij}^{(0)} = \delta_{ij} \qquad \text{and:} \qquad P_{ia}^{(0)} = P_{ai}^{(0)} = P_{ab}^{(0)} = 0$$

Within the scope of first order time-dependent perturbation theory one gets for the Fock and density matrix in a time-dependent external field:

( 46 ) $$F_{pq} = F_{pq}^{(0)} + F_{pq}^{(1)}$$

$$P_{pq} = P_{pq}^{(0)} + P_{pq}^{(1)}$$

After inserting into the expression of the time-dependent density matrix and collecting all first order terms one ends up with:

$$(47)\quad \sum_q \left(F_{pq}^{(0)} P_{qr}^{(1)} - P_{pq}^{(1)} F_{qr}^{(0)} + F_{pq}^{(1)} P_{qr}^{(0)} - P_{pq}^{(0)} F_{qr}^{(1)}\right) = i\frac{\partial}{\partial t} P_{pr}^{(1)}$$

The first order change of the Fock matrix will be introduced as containing two terms. The first one describes the perturbation itself, which is the fluctuating electric field. It is useful to express the perturbation by a Fourier-transformed term in the frequency domain. This allows to confine the response of the Fock matrix to a single fluctuating perturbation at the frequency $\omega$.[175] The second term is responsible for the reaction of the two-electron part of the Fock operator to the change of the density matrix:[172]

$$(48)\quad F_{pq}^{(1)} = g_{pq} + \Delta F_{pq}^{(0)}$$

$$g_{pq} = \frac{1}{2}\left(f_{pq}(\omega) e^{-i\omega t} + f_{qp}^{\dagger}(\omega) e^{i\omega t}\right)$$

$$\Delta F_{pq}^{(0)} = \sum_{st} \frac{\partial F_{pq}^{(0)}}{\partial P_{st}} P_{st}^{(1)}$$

The matrix $f(\omega)$ is a one-electron operator and describes the amplitude of an oscillating electric field (in the following the hint for the frequency dependency is neglected). The time-dependent perturbation is chosen to be complex conjugated to achieve a Hermitian expression for it. The change of the density matrix $P_{pq}^{(1)}$ by the fluctuation potential is given by introducing the coefficients $d$:

$$(49)\quad P_{pq}^{(1)} = \frac{1}{2}\left(d_{pq} e^{-i\omega t} + d_{qp}^{\dagger} e^{i\omega t}\right)$$

The matrix $d$ contains the perturbation densities. After plugging these terms into the time-dependent density matrix expression and collecting all terms depending on $e^{-i\omega t}$ one ends up with (the complex conjugated expression is given by all terms depending on $e^{i\omega t}$):

( 50 )

$$\sum_q \frac{1}{2}\left\{F_{pq}^{(0)} d_{qr} - d_{pq} F_{qr}^{(0)} + \left(f_{pq} + \sum_{st} \frac{\partial F_{pq}^{(0)}}{\partial P_{st}} d_{st}\right) P_{qr}^{(0)} - P_{pq}^{(0)} \left(f_{qr} + \sum_{st} \frac{\partial F_{qr}^{(0)}}{\partial P_{st}} d_{st}\right)\right\} e^{-i\omega t} = \frac{1}{2} i d_{pr} \frac{\partial}{\partial t} e^{-i\omega t}$$

By differentiation after time one gets:

( 51 )

$$\sum_q \left\{F_{pq}^{(0)} d_{qr} - d_{pq} F_{qr}^{(0)} + \left(f_{pq} + \sum_{st} \frac{\partial F_{pq}^{(0)}}{\partial P_{st}} d_{st}\right) P_{qr}^{(0)} - P_{pq}^{(0)} \left(f_{qr} + \sum_{st} \frac{\partial F_{qr}^{(0)}}{\partial P_{st}} d_{st}\right)\right\} = \omega d_{pr}$$

For the first order change of the density matrix one gets by inserting its perturbation series in $P = P^2$:[175]

( 52 ) $$P^2 = \left(P^{(0)} + P^{(1)}\right)\left(P^{(0)} + P^{(1)}\right) = P^{(0)}P^{(0)} + P^{(0)}P^{(1)} + P^{(1)}P^{(0)} + P^{(1)}P^{(1)}$$

The first order terms are equivalent to the first order change of the density matrix:

( 53 ) $$P_{pr}^{(1)} = \sum_q \left(P_{pq}^{(0)} P_{qr}^{(1)} + P_{pq}^{(1)} P_{qr}^{(0)}\right)$$

This is only true if all occupied-occupied $d_{ij}$ and empty-empty blocks $d_{ab}$ of the perturbation matrix $d$ are equal to zero.[172] Therefore, only the occupied-empty $d_{ia}$ and empty-occupied blocks $d_{ai}$ have to be considered in the following. Moreover, the unperturbed Fock and density matrices are diagonal and the elements of the density matrix for the empty orbitals are equal to zero.

( 54 ) $$F_{aa}^{(0)} x_{ai} - x_{ai} F_{ii}^{(0)} + \left(f_{ai} + \sum_{bj}\left\{\frac{\partial F_{ai}^{(0)}}{\partial P_{bj}} x_{bj} + \frac{\partial F_{ai}^{(0)}}{\partial P_{jb}} y_{bj}\right\}\right) P_{ii}^{(0)} = \omega x_{ai}$$

$$F_{ii}^{(0)} y_{ai} - y_{ai} F_{aa}^{(0)} - P_{ii}^{(0)} \left(f_{ia} + \sum_{bj}\left\{\frac{\partial F_{ia}^{(0)}}{\partial P_{bj}} x_{bj} + \frac{\partial F_{ia}^{(0)}}{\partial P_{jb}} y_{bj}\right\}\right) = \omega y_{ai}$$

The nomenclature is changed to be consistent with the common literature. Now, $x_{ai} = d_{ai}$ and $y_{ai} = d_{ia}$ is defined ($d = x + y$).[175] A positive infinitesimal perturbation is considered ($f \to 0$). This is called zero-frequency limit. Within this limit the perturbation of the Fock matrix by the external field can be neglected. Only the change of the Fock matrix due to the perturbation densities has to be considered.[172]

( 55 ) $$\sum_{bj}\left\{\frac{\partial}{\partial P_{bj}}F_{ia}^{(0)}\right\}=\sum_{bj}\left\{\frac{\partial}{\partial P_{bj}}\left((i|h_{core}|a)+(ia||jb)\right)\right\}=\sum_{bj}\left\{\frac{\partial}{\partial P_{bj}}(ia||jb)\right\}=(ia||bj)$$

In the case of canonical HF orbitals, $F_{pp}^{(0)}=\varepsilon_p$ and $P_{ii}^{(0)}=1$ is valid:

( 56 ) $$\varepsilon_a x_{ai}-x_{ai}\varepsilon_i+(ia||bj)x_{bj}+(ia||jb)y_{bj}=\omega x_{ai}$$
$$\varepsilon_i y_{ai}-y_{ai}\varepsilon_a-(ia||bj)x_{bj}-(ia||jb)y_{bj}=\omega y_{ai}$$

In a matrix notation one ends up with the TDHF equations:

( 57 ) $$\begin{bmatrix}A & B\\ B^* & A^*\end{bmatrix}\begin{bmatrix}X\\ Y\end{bmatrix}=\omega\begin{bmatrix}1 & 0\\ 0 & -1\end{bmatrix}\begin{bmatrix}X\\ Y\end{bmatrix}$$

with:

$$A_{ia,jb}=\delta_{ij}\delta_{ab}(\varepsilon_a-\varepsilon_i)+(ia||jb)$$
$$B_{ia,jb}=(ia||bj)$$

The first term of the matrix $A$ contains orbital energy differences of the orbitals form which and in which the excitation takes place. The second term and the matrix $B$ come from the linear response of the Coulomb and the exchange operator to the first order change of the orbitals. The pseudo-eigenvalue equation delivers excitation energies and corresponding transition vectors in the space of the MOs.[172]

According to the Slater-Condon rules the element $A_{ia,jb}$ is equivalent to the integral $\left\langle\Phi_j^b\middle|H-E_0\middle|\Phi_i^a\right\rangle$ of the CIS method. The element $B_{ia,jb}$ covers correlation effects in the ground state by doubly excited determinants via the integral $\left\langle\Phi_0\middle|H\middle|\Phi_{ij}^{ba}\right\rangle$.

If one compares the TDHF equation with the CIS counterpart, one finds that TDHF is equivalent to CIS for $B=0$. In the physical community CIS is called Tamm-Dancoff approximation (TDA) for this reason. TDA will be further discussed in chapter 3.4. TDHF is an extension of CIS, because it contains not only excited states but also de-excited states (corresponding to $X$ and $Y$). A de-excitation of the HF ground state is unphysical. However, this accounts for correlation effects, which should be small. Indeed, the size of the $Y$ amplitudes is a measure for the correlation in the ground state. These amplitudes must be small compared to the $X$ ones. Otherwise, the use of TDHF is questionable.[172]

As long as there are no triplet instabilities, the matrix $(A-B)$ is positive definite. This makes it possible to transform the non-Hermitian TDHF equation into a Hermitain eigenvalue equation with half-dimension:[172]

( 58 ) $(A-B)^{1/2}(A+B)(A-B)^{1/2}Z=\omega^2 Z$ with: $Z=(A-B)^{1/2}(X+Y)$

The TDHF equation can be solved by a Davidson procedure like CIS. The computational time is twice as large as for CIS, because the matrix $B$ must be treated as well.

TDHF has related properties to CIS. The method is size-consistent and pure singlet and triplet states are found for closed-shell systems. Nevertheless, TDHF has some problems in predicting triplet states reliably. In the case of a complete basis TDHF fulfills the Thomas-Reiche-Kuhn sum rule for the oscillator strength in contrast to CIS. Transition moments calculated by TDHF should be superior to their CIS counterparts.[172]

Excitation energies obtained by TDHF are somewhat smaller than the CIS ones. Still, TDHF overestimates excitation energies typically by 0.8 eV. For charge-transfer states even worse results are found. TDHF determines the relative energies of triplet states typically as too low. Due to this TDHF is no real improvement above CIS for potential energies. The higher computational costs of TDHF are most often not justified.[172]

## 3.4 Time-dependent Density Functional Theory (TDDFT)

Time-independent DFT is based on the two Hohenberg-Kohn theorems, which are not valid for a time-dependent theory. Therefore, a time-dependent DFT approach needs corresponding theorems, which have to be formulated and proved. The analog to the first Hohenberg-Kohn theorem is the Runge-Gross theorem. It states that the time-dependent exact electron density $\rho(r,t)$ determines the time-dependent external potential $V(r,t)$ besides a time-dependent spatial constant function $C(t)$, which effects a time-dependent phase factor on the time-dependent wave function $\Psi(r,t)$. Consequently, the time-dependent wave function is a functional of the electron density.[172,176] It can be shown that $\frac{\partial}{\partial t}\alpha(t) = C(t)$ is valid. Consequently, one gets for the time dependent wave function:

( 59 ) $$\Psi(r,t) = \Psi[\rho(t)](t) \cdot e^{-i\alpha(t)}$$

The Runge-Gross theorem is a first step for the formulation of a time-dependent many-body theory. A second condition is the existence of a variational principle, which would be an analogue to the second Hohenberg-Kohn theorem. Such a principal can be derived from the quantum mechanical action integral $A$ in the period $t_0$ to $t_1$:

( 60 ) $$A[\rho] = \int_{t_0}^{t_1} dt \left\langle \Psi[\rho](r,t) \middle| i\frac{\partial}{\partial t} - H(r,t) \middle| \Psi[\rho](r,t) \right\rangle$$

If the time-dependent wave function describes the solution of the Schrödinger equation with the initial condition $\Psi(r,t_0) = \Psi_0(r)$, in general the wave function is a stationary point of the action integral. Therefore, the exact electron density can be calculated by the following Euler equation, if appropriate boundary conditions are applied:[172]

( 61 ) $$\frac{\partial A[\rho]}{\partial \rho(r,t)} = 0$$

This relation is a prescription to determine the exact density and is the wanted analog to the second Hohenberg-Kohn theorem. In the following the time-dependent action integral is used to derive the time-dependent Kohn-Sham equations. The starting point is the time-dependent electronic Schrödinger equation:

( 62 ) $H(r,t)\Psi(r,t) = \mathrm{i}\frac{\partial}{\partial \mathrm{t}}\Psi(r,t)$ with: $H(r,t) = T(r) + V_{\mathrm{ee}}(r) + V_{\mathrm{en}}(r) + V(t)$

and: $r = \vec{r} = \{\vec{r}_1, \vec{r}_2, \dots, \vec{r}_N\}$

Now, $T(r)$ is the operator for the kinetic energy of all electrons, $V_{\mathrm{ee}}(r)$ the one of the electron-electron repulsion, $V_{\mathrm{en}}(r)$ describes the nucleus-electron attraction and $V(t)$ is the time-dependent potential. The last one is given by a sum over single particle operators ($N$: number of electrons):

( 63 ) $V(r,t) = \sum_{i=1}^{N} v(r_i, t)$

Using the definition of the Hamiltonian in ( 62 ) one can separate the action integral into two parts. One is universal and solely depends on the number of electrons. The other depends on the external potential $v(r,t) = V_{en}(r) + V(r,t)$:

( 64 ) $A[\rho] = B[\rho] - \int_{t_0}^{t_1} dt \int d^3 r \rho(r,t) v(r,t)$

The universal potential $B[\rho]$ is given by:

( 65 ) $B[\rho] = \int_{t_0}^{t_1} dt \left\langle \Psi[\rho](r,t) \middle| i\frac{\partial}{\partial t} - T(r) - V_{ee}(r) \middle| \Psi[\rho](r,t) \right\rangle$

According to the time-independent Kohn-Sham equations a time-dependent non-interacting reference system is introduced with the external single particle operators $v_S(r,t)$. The density $\rho_S(r,t)$ of the non-interacting system is equal to the exact density $\rho(r,t)$. Corresponding to the generalization of the Runge-Gross theorem after van Leeuwen[177] the existence of such a non-interacting reference system is normally ensured. This reference system can be expressed by a Slater determinant $\Phi(r,t)$, which contains one-electron orbitals $\phi_i(r,t)$. The electron density is given by:

( 66 ) $\rho(r,t) = \rho_S(r,t) = \sum_{i=1}^{N} |\phi_i(r,t)|^2$

The orbitals are solutions of the time-dependent single particle Schrödinger equation:

( 67 ) $i\frac{\partial}{\partial \mathrm{t}}\phi_i(r,t) = \left(-\frac{1}{2}\nabla_{\mathrm{i}}^2 + v_S(r,t)\right)\phi_{\mathrm{i}}(r,t)$

Otherwise, the non-interacting density can be introduced by the mentioned Euler equation. Due to the non-interacting reference system $\mathrm{V_{ee}} = 0$, it is valid that:

( 68 ) $$A_S[\rho] = B_S[\rho] - \int_{t_0}^{t_1} dt \int d^3r \rho(r,t) v_S(r,t)$$

with:

( 69 ) $$B_S[\rho] = \int_{t_0}^{t_1} dt \left\langle \Psi[\rho](r,t) \middle| i\frac{\partial}{\partial t} - T(r) \middle| \Psi[\rho](r,t) \right\rangle$$

At the stationary point one gets:

( 70 ) $$\frac{\partial A_S[\rho]}{\partial \rho(r,t)} = \frac{\partial B_S[\rho]}{\partial \rho(r,t)} - v_S(r,t) = 0$$

If a time-dependent single particle potential $v_S(r,t)$ exists, it must be a unique functional of the density according to the Runge-Gross functional. At the point of the exact density one finds:

( 71 ) $$v_S(r,t) = \frac{\partial B_S[\rho]}{\partial \rho(r,t)}$$

Having this equation, the action integral of the interacting system can be reformulated:

( 72 ) $$A[\rho] = B_S[\rho] - \int_{t_0}^{t_1} dt \int d^3r \rho(r,t) v(r,t) - \frac{1}{2}\int_{t_0}^{t_1} dt \int d^3r \int d^3r' \frac{\rho(r,t)\rho(r',t)}{|r-r'|} - A_{xc}[\rho]$$

Now, $A_{xc}[\rho]$ is the so-called exchange correlation part (*xc*) of the action integral:

( 73 ) $$A_{xc}[\rho] = B_S[\rho] - \frac{1}{2}\int_{t_0}^{t_1} dt \int d^3r \int d^3r' \frac{\rho(r,t)\rho(r',t)}{|r-r'|} - B[\rho]$$

It contains all contributions, which are beyond the non-interacting reference system. By inserting the reformulated action integral in the Euler equation, one gets:

( 74 ) $$\frac{\partial B_S[\rho]}{\partial \rho(r,t)} = v(r,t) + \int d^3r' \frac{\rho(r',t)}{|r-r'|} + \frac{\partial A_{xc}[\rho]}{\partial \rho(r,t)}$$

This expression is only valid for the exact density of the interacting system. With the introduced definition of the time-dependent single particle potential the following is valid:

$$(75)\quad v_S(r,t) = \frac{\partial B_S[\rho]}{\partial \rho(r,t)} = v(r,t) + \int d^3r' \frac{\rho(r',t)}{|r-r'|} + \frac{\partial A_{xc}[\rho]}{\partial \rho(r,t)}$$

One ends up with the Kohn-Sham equations by putting this expression into the time-dependent single particle Schrödinger equation:

$$(76)\quad i\frac{\partial}{\partial t}\phi_i(r,t) = \left(-\frac{1}{2}\nabla_i^2 + v(r,t) + \int d^3r' \frac{\rho(r',t)}{|r-r'|} + \frac{\partial A_{xc}[\rho]}{\partial \rho(r,t)}\right)\phi_i(r,t)$$

$$i\frac{\partial}{\partial t}\phi_i(r,t) = F^{\mathrm{KS}}\phi_i(r,t)$$

The time-dependent Kohn-Sham equations (KS) are single particle equations similar to the time-independent ones. The electrons are treated in the mean field of all electrons. All exchange and correlation effects are included in $\frac{\partial A_{xc}[\rho]}{\partial \rho(r,t)}$. Till this point the KS equations are formally exact. But the exact *xc* action integral is unknown and approximations to it have to be introduced. The first one is to replace the non-local in time *xc* action integral by a time-independent local one. This is called *adiabatic local density approximation* (ALDA).[172] The basis for this substitution is that the density varies only slowly in time. The benefit is that existing *xc* functional can be employed, which were developed for time-independent DFT.

The derivation of the TDDFT equations follows the one of the TDHF equations and for this reason it is skipped here. The only difference is that the Fock matrix is replaced by the KS matrix:

$$(77)\quad \begin{bmatrix} A & B \\ B^* & A^* \end{bmatrix}\begin{bmatrix} X \\ Y \end{bmatrix} = \omega \begin{bmatrix} 1 & 0 \\ 0 & -1 \end{bmatrix}\begin{bmatrix} X \\ Y \end{bmatrix}$$

with:

$$A_{ia,jb} = \delta_{ij}\delta_{ab}(\varepsilon_a - \varepsilon_i) + (ia|jb) + (ia|f_{xc}|jb)$$
$$B_{ia,jb} = (ia|bj) + (ia|f_{xc}|bj)$$

In contrast to TDHF the last term does not correspond to the response of the non-local HF exchange potential, which is a coulomb term. Here, it is the response of the *xc* potential. In context of the ALDA this is the second functional derivative of the *xc* energy $E_{xc}$:

( 78 ) $(ia|f_{xc}|jb) = \int\int d^3r d^3r' \phi_i^*(r)\phi_a(r) \frac{\partial^2 E_{xc}}{\partial\rho(r)\rho(r')} \phi_j^*(r')\phi_b(r')$

Similar to TDHF the Tamm-Dancoff approximation (TDA) can be introduced for TDDFT as well. To do so, the matrix $B$ is neglected and only the occupied-empty block of the matrix *d* is considered:

( 79 ) $AX = \omega X$

This Hermitian eigenvalue equation is usually a good approximation to TDDFT. One reason for this could be that for DFT some correlation is considered already in the ground state via the *xc* functional. Since the size of the amplitudes of $Y$ and the elements of the matrix $B$ are measures of missing correlation in the ground state, their values should be even smaller in TDDFT than in TDHF. Hence, TDA should be a better approximation to TDDFT than to TDHF. In combination with TDHF, TDA end up with CIS. This is not the case for TDDFT. Figure 8 gives an overview about the relation of these methods.[172]

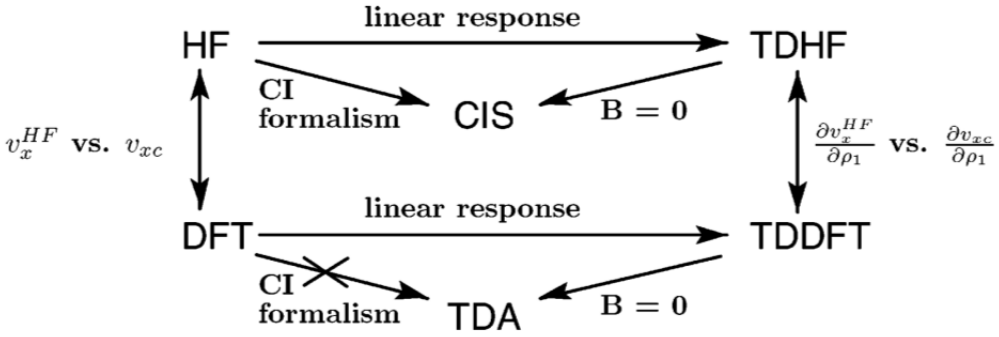


**Figure 8: Schematic illustration of the relation of HF and DFT in their time-independent und time-dependent representations. Furthermore, the Tamm-Dancoff approximation (TDA) is shown for both methods.[172] Reprinted with permission from A. Dreuw, M. Head-Gordon, Chem. Rev. 2005, 105, 4009. Copyright 2012, American Chemical Society.**

In the context of ALDA it is possible to utilize every ground state *xc* functional for TDDFT. It came out that the results of TDDFT are rather sensitive to the choice of the *xc* functional. Therefore, it is always necessary to proof the reliability of TDDFT by wave function based methods.[172]

Overall, the properties of TDDFT are comparable to the ones of TDHF. Exceptions are that TDDFT is more resistant to triplet instabilities than TDHF and that explicit electron correlation is included in TDDFT via the *xc* functional.[172] Like TDHF, TDDFT can be transformed into a Hermitian eigenvalue

equation. But, TDDFT is computationally a little bit more demanding than TDHF, if a hybrid functional is used. The reason for this is that next to the response of the coulomb and exchange terms also the response of the *xc* functional has to be calculated. This is done numerically on an atom centered three dimensional grid, like it is done for time-independent DFT. For a pure GGA functional the matrix $(A - B)$ becomes diagonal. This allows avoiding the multiplication of the test vectors in the iterative Davidson procedure. Now the computational demand for TDDFT and TDA is comparable. For hybrid functional TDA reduces the computational time to a factor of two at maximum. Using TDDFT it is possible to calculate molecular systems with up to 300 atoms, if the *resolution of identity* (RI) approximation is used.[172]

With TDDFT excitation energies are calculated with errors of typically 0.1 to 0.5 eV for valence excited states. Therefore, the error of TDDFT is in the same range than the one of the much more demanding methods EOM-CCSD or CASPT2. To reach this accuracy a large basis set is necessary. The reason for the high accuracy is caused by the fact that normally the KS orbital energy differences, which are the leading term in the elements of the matrix *A*, are good estimates to excitation energies. In contrast to HF the energies of the empty orbitals are calculated for the *N*-electron system in DFT. They correspond to the single particle energies of an excited electron rather to the energy of an additional electron like in HF.[172]

Although, TDDFT yields good results for valence excited states, there are serious problems for Rydberg, charge transfer (CT) and doubly excited states (the last point is also valid for CIS and TDHF). For such states the excitation energies can be wrong by several eV. Doubly excited states are not covered by linear response theory. They can be calculated by special frequency or energy dependent *xc* functionals. The problem for Rydberg and CT states can be traced back to the wrong long-range behavior of common *xc* functionals. They drop faster than $1/R$ ($R$: electron-nucleus distance). At very large donor acceptor distances the excitation energy should trend to the energy difference of ionization potential *IP* and electron affinity *EA* in the case of CT states:

( 80 ) $$\omega_{CT} = IP^{Donor} - EA^{Akzeptor}$$

At large distances the matrix $B$ vanishes, since the overlap is zero between occupied and empty orbitals. Then the matrix $A$ is reduced to:

( 81 ) $$A_{ia,jb} = \delta_{ij}\delta_{ab}(\varepsilon_a - \varepsilon_i)$$

Hence, CT excitation energies are solely described by orbital energy differences at large donor acceptor distances. Since they are calculated for the *N*-electron system, the CT excitation energies are massively underestimated. The benefit of TDDFT for valance excited states converts into the opposite for CT states. For these states TDHF should yield better results. An obvious approach to solve this problem is to use hybrid functional with a HF exchange part, which is variable with the distance $r_{ij}$:

( 82 ) $$\frac{1}{r_{ij}} = \frac{1-erf(\mu r_{ij})}{r_{ij}} + \frac{erf(\mu r_{ij})}{r_{ij}}$$

Here, *erf* is the error function. The operator $\frac{1}{r_{ij}}$ is replaced by a short-range (first one) and a long-range term (second one). The Parameter $\mu$ determines the position of the transition between short- and long-range parts. For the short-range part common GGA or hybrid functional are used, where the long-range part is described by HF. Popular so called long-range corrected functional using this approach are CAM-B3LYP or ωB97x.

In Figure 9 a pure GGA, a hybrid and a long-range corrected functional are compared for different classes of excitations.[178] A different error is found depending on the spatial overlap $\Lambda$ of occupied and empty orbitals. For valence excitation $\Lambda$ is almost one and the error of all functional similar. The spatial overlap becomes smaller for Rydberg and CT excitations. The GGA functional yields large errors for small $\Lambda$ values. The hybrid functional behaves slightly better due to the HF part. A significant improvement is found for the long-range corrected functional. This proofs the former considerations and underlines the importance of long-range corrections.

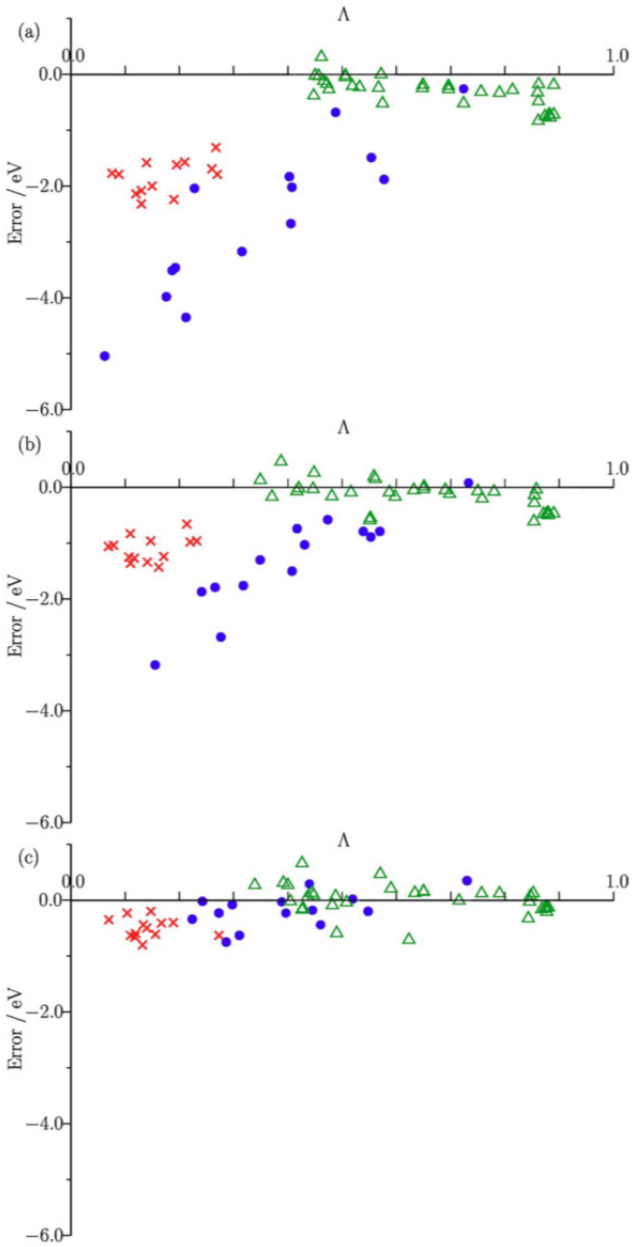


**Figure 9: Error of excitation energies calculated by TDDFT plotted against the spatial overlap Λ between occupied and empty orbitals. (a) The pure GGA functional PBE, (b) the hybrid functional B3LYP and (c) the long-range corrected functional CAM-B3LYP are compared for valence (green triangles), Rydberg (red crosses) and CT excitations (blue dots).[178] Reprinted with permission from M. J. G. Peach, P. Benfield, T. Helgaker, D. J. Tozer at al., J. Chem. Phys. 2008, 128 (4), 044118. Copyright 2012, American Institute of Physics.**

## 3.5 Approximate Coupled Cluster method 2nd order (CC2)

CC2 is an approximation to the 2nd order coupled cluster method CCSD. The energy within CCSD is determined by ($\psi_0$: HF reference wave function, $T_i$: Cluster operator):

( 83 ) $$H\exp(T_1+T_2)|\psi_0\rangle = E\exp(T_1+T_2)|\psi_0\rangle$$

The initial equations to determine the amplitudes of the singly excited $t_i^a$ and doubly excited $t_{ij}^{ab}$ manifold are given by ($\psi_m^x$: Singly excited wave function out of the HF reference, $\psi_{mn}^{xy}$: Doubly excited wave function out of the HF reference):

( 84 ) $$\langle\psi_m^x|H\exp(T_1+T_2)|\psi_0\rangle = E\langle\psi_m^x|\exp(T_1+T_2)|\psi_0\rangle$$
$$\langle\psi_{mn}^{xy}|H\exp(T_1+T_2)|\psi_0\rangle = E\langle\psi_{mn}^{xy}|\exp(T_1+T_2)|\psi_0\rangle$$

It is common to rewrite these equations for practical reasons. To do so one multiplies from the left by $\exp(-T_2-T_1)$. This corresponds to a similarity transformation of the Hamiltonian:[179]

( 85 ) $$\exp(-T_2-T_1)H\exp(T_1+T_2)|\psi_0\rangle = E\exp(-T_2-T_1)\exp(T_1+T_2)|\psi_0\rangle$$
$$\exp(-T_2-T_1)H\exp(T_1+T_2)|\psi_0\rangle = E|\psi_0\rangle$$

By projection on $\langle\psi_0|$, $\langle\psi_m^x|$ and $\langle\psi_{mn}^{xy}|$ one gets:

( 86 ) $$E = \langle\psi_0|\exp(-T_2-T_1)H\exp(T_1+T_2)|\psi_0\rangle$$
$$0 = \langle\psi_m^x|\exp(-T_2-T_1)H\exp(T_1+T_2)|\psi_0\rangle$$
$$0 = \langle\psi_{mn}^{xy}|\exp(-T_2-T_1)H\exp(T_1+T_2)|\psi_0\rangle$$

These similarity transformed equations ( 86 ) are called *linked* CCSD equations - in contrast to the former equations ( 83 ) and ( 84 ), which are the *unlinked* CCSD equations. Both systems of equations lead to the same amplitudes and energies as solution. The similarity transformation causes a non-Hermitian Hamiltonian.

Now, a $T_1$-transformed Hamilton according to $\widetilde{H} = \exp(-T_1)\,H\,\exp(T_1)$ can be introduced:

( 87 ) $$E = \langle\psi_0|\exp(-T_2)\exp(T_2)|\psi_0\rangle$$

$$0 = \langle \psi_m^x | \exp(-T_2) \exp(T_2) | \psi_0 \rangle$$
$$0 = \langle \psi_{mn}^{xy} | \exp(-T_2) \exp(T_2) | \psi_0 \rangle$$

The Baker-Campbell-Hausdorff (BCH) series for two operators $A$ and $B$ is:

( 88 ) $$\exp(-A)\, B\, \exp(A) = B + [B,A] + \frac{1}{2!}\big[[B,A],A\big] + \frac{1}{3!}\Big[\big[[B,A],A\big],A\Big] + \cdots$$

It can be shown that for the similarity transformed Hamiltonian the BCH series ends with the term, which is quadratic for the amplitudes. This is due to the special structure of the cluster operators:[179]

( 89 )
$$\exp(-T) H \exp(T) = H + [H,T] + \frac{1}{2}\big[[H,T],T\big] + \frac{1}{6}\Big[\big[[H,T],T\big],T\Big] + \frac{1}{24}\Big[\big[\big[[H,T],T\big],T\big],T\Big]$$

This series can be applied to the $T_1$-transformed CCSD equations for the amplitudes ( 87 ). Many of the resulting commutators are zero (see p 687f in the book *„Molecular Electronic-Structure Theory"* of T. Helgaker et al.)[179] and one ends up with:

( 90 ) $$\langle \psi_m^x | \widetilde{H} | \psi_0 \rangle + \langle \psi_m^x | \big[\widetilde{H}, T_2\big] | \psi_0 \rangle = 0$$
( 91 ) $$\langle \psi_{mn}^{xy} | \widetilde{H} | \psi_0 \rangle + \langle \psi_{mn}^{xy} | \big[\widetilde{H}, T_2\big] | \psi_0 \rangle + \frac{1}{2} \Big\langle \psi_{mn}^{xy} \Big| \Big[\big[\widetilde{H}, T_2\big], T_2\Big] \Big| \psi_0 \Big\rangle = 0$$

Concerning the computational time the last two terms preponderate. They scale with $N^6$ ($N$: Number of basis functions). All other terms scale with $N^5$ or faster. Furthermore, these terms describe higher excitations than doubles. If one just wants to approximate the double excitations, these terms are not necessary. In this scope the order of a term is defined as following: A term with $n^{\text{th}}$ order contains the cluster operator $T_{(n+1)}$. This definition differs from the one of Møller-Plesset perturbation theory (MP), where the single excitations are in 0$^{\text{th}}$ order. A reason for this new definition is that the singles are a key parameter for the orbital relaxation.[179]

For the double excitations all terms of 2$^{\text{nd}}$ or higher order are neglected, to reduce the computational effort due to the consideration above. These are the complete third term in ( 91 ) and parts of the second one. Expanding the Taylor series of the $T_1$-transformed Hamiltonian one gets (only terms till 1$^{\text{st}}$ order are listed):

( 92 ) $$\exp(-T_1) H \exp(T_1) = \left(1 - T_1 + \frac{1}{2}T_1^2\right) H \left(1 + T_1 + \frac{1}{2}T_1^2\right)$$

$$\exp(-T_1)H\exp(T_1) = H + HT_1 + \frac{1}{2}HT_1^2 - T_1H - T_1HT_1 + \frac{1}{2}T_1^2H$$

By plugging this expression into the 2nd term of ( 91 ) one ends up with (again only terms till 1st order are shown):

$$(93)\quad \left\langle \psi_{mn}^{xy}\middle|\left[\widetilde{H},T_2\right]\middle|\psi_0\right\rangle = \left\langle \psi_{mn}^{xy}\middle|\left[\left(H + HT_1 + \frac{1}{2}HT_1^2 - T_1H - T_1HT_1 + \frac{1}{2}T_1^2H\right),T_2\right]\middle|\psi_0\right\rangle$$

After breaking up the commutator relation in ( 93 ) only two terms survive, if terms of higher order than 1st are neglected. This approximated expression can be contracted again to a commutator relation:

$$(94)\quad \left\langle \psi_{mn}^{xy}\middle|\left[\widetilde{H},T_2\right]\middle|\psi_0\right\rangle \approx \left\langle \psi_{mn}^{xy}\middle|(HT_2 - T_2H)\middle|\psi_0\right\rangle = \left\langle \psi_{mn}^{xy}\middle|[H,T_2]\middle|\psi_0\right\rangle$$

In order to yield an energy, which is correct up to 2nd order, it is sufficient to consider the amplitudes of the double excitations only till 1st order. This approach is comparable to MP2. Using this, the equations for the double excitations can be further simplified. The Hamiltonian $H$ in ( 94 ) is approximated by the Fock operator $F$. This leads to initial equations to solve the amplitudes for the double excitations, which are very similar to the MP2 counterparts. The final CC2 equations are:[180]

$$(95)\quad \left\langle \psi_m^x\middle|\widetilde{H}\middle|\psi_{HF}\right\rangle + \left\langle \psi_m^x\middle|\left[\widetilde{H},T_2\right]\middle|\psi_{HF}\right\rangle = 0$$
$$\left\langle \psi_{mn}^{xy}\middle|\widetilde{H}\middle|\psi_{HF}\right\rangle + \left\langle \psi_{mn}^{xy}\middle|[F,T_2]\middle|\psi_{HF}\right\rangle = 0$$

The equations for the single excitations are the unchanged ones from CCSD. All terms of second or higher order are neglected. Therefore, only the amplitudes of the single excitations remain as parameters, which have to be calculated iteratively. The equations for the amplitudes of the double excitations $t_{mn}^{xy}$ match the MP2 ones besides the fact that the two electron MO integrals are modified:[181]

$$(96)\quad t_{mn}^{xy} = \frac{1}{1+\delta_{mn}\delta_{xy}} \cdot \frac{(xm|yn)}{\varepsilon_m - \varepsilon_x + \varepsilon_n - \varepsilon_y}$$

CC2 scales with the number of basis functions like MP2 ($N^5$), but the CC2 equations have to be solved iteratively in contrast to MP2. It is expected that the CC2 energy is of the same quality than MP2. Therefore, the benefit of CC2 is not the accuracy for the ground state energy. It is the possibil-

ity to calculate time-dependent properties. This is possible due to the considered single excitations, which are not included in MP2.

To determine time-dependent properties one has to consider a system under a time-dependent one-electron fluctuation $V(t)$:

( 97 ) $H = F + U + V(t)$ with: $V(t) = \int_{-\infty}^{\infty} d\omega f(\omega) e^{-i\omega t}$

In ( 97 ) $F$ means the Fock operator and $U$ a time-independent perturbation. This perturbation contains the correlation of the CC2 ansatz. An explicit orbital relaxation is not requested. The reason for this is that in the context of linear response theory an orbital relaxation would yield artificial HF poles. This means that not $F + V(t)$ is the 0[th] order problem for the perturbation theory (this would be valid for orbital relaxation), but only $F$ is the unperturbed system. The different perturbations $U$ and $V(t)$ act on the system. Here, the single excitations are 0[th] order for the perturbation $U$ and first order for the time-dependent perturbation $V(t)$. This approach is an alternative to consider orbital relaxation. Double excitations are treated like in the case of the time-independent CC2 equations. They are approximated to be 1[st] order in $U$ and for $V(t)$ all terms are retained. This leads to the time-dependent CC2 equations for the amplitudes:[180]

( 98 ) $\left\langle \psi_m^x \middle| \tilde{H} + \left[\tilde{H}, T_2\right] \middle| \psi_{HF} \right\rangle = i \frac{\partial t_m^x}{\partial t}$

$\left\langle \psi_{mn}^{xy} \middle| \tilde{H} + [F + V(t), T_2] \middle| \psi_{HF} \right\rangle = i \frac{\partial t_{mn}^{xy}}{\partial t}$

Using ( 98 ) one can compile the linear response functions. A detailed derivation can be found in literature.[180,182] Excitation energies and transition moments are given by the poles of the response function. The poles can be determined by the eigenvalues of the Jacobian matrix $A$:

( 99 ) $AX = \omega X$ with: $X^\dagger X = 1$

The Jacobian $A$ contains derivatives of the CC2 equations, which are collected in $\Omega_\mu$, with respect to the amplitudes $t_\nu$:[183]

( 100 ) $A_{\mu\nu} = \frac{\partial \Omega_\mu}{\partial t_\nu}$

The Jacobian of CC2 is given by ($\tau_m^x$, $\tau_{mn}^{xy}$: excitation operators):[184]

$$(101)\quad A^{CC2} = \begin{pmatrix} \langle \psi_m^x | [(\widetilde{H} + [\widetilde{H}, T_2]), \tau_m^x] | \psi_{HF} \rangle & \langle \psi_m^x | [\widetilde{H}, \tau_{mn}^{xy}] | \psi_{HF} \rangle \\ \langle \psi_{mn}^{xy} | [\widetilde{H}, \tau_m^x] | \psi_{HF} \rangle & \langle \psi_{mn}^{xy} | [F, \tau_{mn}^{xy}] | \psi_{HF} \rangle \end{pmatrix}$$

This matrix is non-symmetric. Close to conical intersections this causes serious problems, which is demonstrated in the following. Consider a block-diagonalization of the Jacobian $A$ by a non-unitary transformation:

$$(102)\quad A = U_L A U_R \qquad \text{with:} \quad U_L U_R = 1$$

Further, two almost degenerate states $i$ and $j$ are considered, whose eigenvalues are decoupled:

$$(103)\quad A = \begin{pmatrix} A_{ii} & A_{ij} & 0 \\ A_{ji} & A_{jj} & 0 \\ 0 & 0 & \ddots \end{pmatrix}$$

In general the 2x2 block of this effective two state problem can be expressed by:

$$(104)\quad A^{2x2} = \begin{pmatrix} E - \Delta & S - R \\ S + R & E + \Delta \end{pmatrix}$$

The eigenvalues are $E_{1,2} = E \mp \sqrt{\Delta^2 + S^2 - R^2}$. In the case of a symmetric matrix ($R = 0$), both states are degenerate, if $\Delta$ and $S$ vanish. This yields conical intersections in the dimension $N^{int} - 2$ ($N^{int}$: Number of internal degrees of freedom for the core coordinates). If both states belong to different irreducible representations, $S$ has to vanish and the intersection has the dimension $N^{int} - 1$. Different cases have to be separated for non-symmetric Jacobians, which appear for iterative Coupled Cluster methods in general:[184]

(i) $R^2 < \Delta^2 + S^2$: One obtains two real eigenvalues according to $E_{1,2} = E \mp \sqrt{\Delta^2 + S^2 - R^2}$. This is the usual case for single point calculations or geometry optimizations.

(ii) $R^2 > \Delta^2 + S^2$: A conjugated pair of degenerate roots is found with the eigenvalues $E_{1,2} = E \mp i\sqrt{\Delta^2 - S^2 - R^2}$.

(iii) $R^2 = \Delta^2 + S^2$: A non-physical degeneration is predicted. This degeneration has the dimension $N^{int} - 1$.

(iv) $R = \Delta = S = 0$: This is the only condition to find a true intersection. Unfortunately, the dimension is lowered to $N^{int} - 3$ due to the additional condition, which is too low.

Methods possessing a non-symmetric Jacobian, like CC2 or CIS($D_\infty$), are not able to describe conical intersections between states of the same irreducible representation qualitatively correct.

Another drawback of these methods is the fact that the left and right eigenvector of the solution of the linear response function are not equivalent. A further diagonalization is necessary, to calculate transition moments according to $\vec{M}_i = \sum_n X_{n,i} \langle \psi_n | \vec{\mu}_e | \psi_0 \rangle$. The additional computational effort is in the same order than the preliminary calculation of the excitation energy.

## 3.6 Algebraic Diagrammatic Construction (ADC)

The *algebraic diagrammatic construction* is a method exclusively for excited states, which is based on the many-particle Green's function. The ADC equations can be derived by the so-called *intermediate state representation*:

The polarization propagator $\Pi(\omega)$ contains all information about the excitation spectrum in context of the many-particle Green's function. A $N$-electron system is considered with the Hamiltonian $H$ and the exact ground state wave function $|\psi_0\rangle$ with the exact energy $E_0$. The polarization propagator for this system in its general algebraic form becomes (derived from Goldstone diagrams):[185,186]

( 105 ) $\Pi(\omega) = f^\dagger(\omega - A)^{-1} f$

The Jacobian $A$ of ADC is defined as:

( 106 ) $A_{IJ} = \langle\psi_I|H - E_0|\psi_J\rangle$

$f$ is the matrix of the effective transition amplitudes:

( 107 ) $f_{J,rs} = \langle\psi_J|c_r^\dagger c_s|\psi_0\rangle$

Here, a complete set of intermediate states $|\psi_I\rangle$ is introduced. This set is achieved by constructing a set of so-called correlated excited states $|\Psi_J^0\rangle$ out of the wave function of the exact ground state $|\Psi_0\rangle$:

( 108 ) $|\Psi_J^0\rangle = C_J|\Psi_0\rangle$ with: $C_J \epsilon \{c_a^\dagger c_i; c_b^\dagger c_j c_a^\dagger c_i, a < b, i < j; \cdots\}$

The set of correlated states is not an orthonormal system. A successive Gram-Schmidt-orthonormalization starting from $|\Psi_0\rangle$ is necessary to end up with the intermediate states. Now, one has a complete set of intermediate states in the space of the exact excited states.

The excitation energies are equivalent to the eigenvalues of the Jacobian like for CC2:

( 109 ) $AX = \omega X$ with: $X^\dagger X = 1$

The excited states $|\Psi_n\rangle$ are given by:

( 110 ) $|\Psi_n\rangle = \sum_I X_{In}|\Psi_I\rangle$

Transition moments $T_n = \langle\psi_n|D|\psi_0\rangle$ are calculated by:

( 111 ) $T_n = \sum_I X_{In}\,\langle\psi_I|D|\psi_0\rangle = \sum_I X_{In}\sum_{rs} d_{rs} f_{I,rs}$

Here, $D$ is an one-particle transition operator with the matrix elements $d_{rs} = \langle\varphi_r|d|\varphi_s\rangle$.[185]

The Jacobian $A$ and the matrix of the transition amplitudes $f$ can be developed in a perturbation series:

( 112 ) $A = A^{(0)} + A^{(1)} + \cdots$

$f = f^{(0)} + f^{(1)} + \cdots$

This ends up with a formal perturbation series of the polarization propagator $\Pi(\omega)$. This opens a way to classify ADC systematically into orders. Only terms until a given order are considered in the perturbation series of $A$ and $f$. If one considers terms up to $n^{\text{th}}$ order, one gets ADC($n$).[185]

In general, the wave function and energy of the exact ground state are unknown. Therefore, one has to find approximations for them. A common way to do this is Møller-Plesset perturbation theory (MP). For a given order of ADC, it is common to use the same order of MP perturbation theory.[187]

ADC is a size-consistent method for excitation energies and transition moments. This means that local and non-local excitations are strictly decoupled (the ADC equations are separable). Furthermore, the configuration space of ADC is smaller than the one of a comparable CI method, which means that ADC is more compact than CI.[185]

The Jacobian of ADC is symmetric in contrast to the iterative Coupled Cluster methods. The Jacobian of ADC(2) is the symmetric variant of the corresponding one of CIS($D_\infty$):[184]

( 113 ) $\underline{A}^{CIS(D_\infty)} = \begin{pmatrix} \langle\psi_m^x|[(H + [H, T_2]), \tau_m^x]|\psi_{HF}\rangle & \langle\psi_m^x|[H, \tau_{mn}^{xy}]|\psi_{HF}\rangle \\ \langle\psi_{mn}^{xy}|[H, \tau_m^x]|\psi_{HF}\rangle & \langle\psi_{mn}^{xy}|[F, \tau_{mn}^{xy}]|\psi_{HF}\rangle \end{pmatrix}$

( 114 ) $\underline{A}^{ADC(2)} = \frac{1}{2}\underline{A}^{CIS(D_\infty)} + \frac{1}{2}\left(\underline{A}^{CIS(D_\infty)}\right)^{\dagger}$

The symmetric Jacobian of ADC(2) has benefits with respect to the computational effort compared to CC2 or CIS($D_\infty$) due to the identical left and right eigenvector in ( 109 ). The calculation of gradients and transition moments is considerably simplified. Moreover, the problem close to conical intersections is solved (see chapter 3.5). In principle, ADC(2) delivers qualitatively correct potential energies at conical intersections. However, one has to keep in mind that ADC(2) is a one-determinant method and static correlation effects are not considered. At conical intersections with the ground state, ADC(2) fails for this reason. Here multi-reference methods like CASPT2 should be used.

CC2, CIS($D_\infty$) as well as ADC(2) are iterative methods, which scale with $N^5$ ($N$: Number of basis functions). In a comparison of the errors in the excitation energies of these methods with CCSD, which scales with $N^6$, CC2 and ADC(2) yield comparable results to CCSD. This underlines the importance of both methods for the calculation of excited states. Especially ADC(2) is a very valuable method due to its benefits for the calculation of transition moments as discussed above. The effort to calculate transition moments with CC2 can become as demanding as the calculation of excitation energies. However, ADC(2) is a method purely for excited states and the ground state must be calculated with MP2 or comparable methods. This is in contrast to CC2, for which the ground state energy is defined.

# 4. Computational details

The computations were performed for dimers as a model system for larger aggregates. To investigate variations in energy order and characters of the involved states as a function of the relative orientation of both monomers, potential energy curves were computed for two different motions: a torsional motion representing aggregates in solution and a shift motion for crystals. The monomer geometries of the chromophores were optimized with the dispersion corrected density functional theory (DFT-D2) method[188,189] using the BLYP[190-192] functional in combination with the TZVP[193] basis set at the non-hydrogen atoms and the TZV[193] basis set at the hydrogen atoms.[193] In the following this level of theory is designated as BLYP-D/TZV(P). The same method was used to calculate the geometry optimized dimer structures. To obtain the possible minimum structures in the electronic ground state, geometry optimizations were performed out of a large number of randomly generated dimer structures.

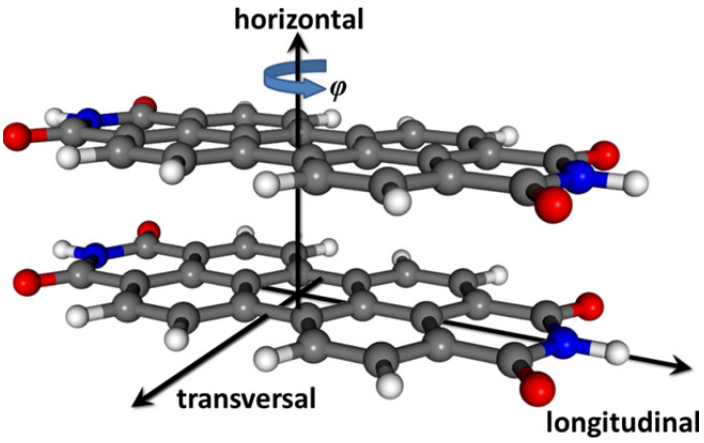


**Figure 10: Internal coordinates to describe the relative orientation of the monomers with respect to each other. The angle ϕ represents the torsion motion of the dimer system.**

**Potential energy curves**

Potential energy curves (PECs) were calculated for dye dimers built up as shown in Figure 10 from two monomers with a distance of 3.3 Å. The latter corresponds to the optimal distance of non-relaxed dimers for PBI and DIP determined by the above mentioned DFT method. The ground state potential energy curves were computed by Møller-Plesset theory at second order MP2 using spin component scaling (SCS-MP2) in combination with the resolution of identity approximation.[174,194,195] Excitation energies were calculated by the approximate coupled cluster second order method using

spin component scaling (SCS-CC2).[196,197] For these computations the TZV(P) basis sets described above is employed, expect for the PESs in chapter 5.2 where a SVP basis set was employed.[194,198] SCS-CC2 was also used with the resolution of identity approximation[193,199,200] employing the recommended TZVP auxiliary basis set[194] for all atoms. All calculations were performed with the Turbomole 6.0 program package.[201]

**Character analysis**

The analysis of the character of the excited states was performed by a method developed by Liu et al.[202,203] It is based on a Löwdin localization of the delocalized dimer MOs to the monomers. After the corresponding transformation of the wave functions of the excited states the coefficients can be used to analyse the states by their amount of charge transfer versus Frenkel character.

**Mechanically embedded QM/MM**

In the description of exciton self-trapping processes quantum mechanical (QM) approaches are mandatory since electronically excited states are involved. On the other hand the computations in chapter 5.2 have to include a large fraction of the crystal to describe how it hampers photo-induced motions by steric restrictions. A cluster was used which comprises 9500 atoms to get a reliable description of the motions. Because accurate QM approaches are way too expensive to describe systems of that size, a hybrid QM/MM approach is employed. It uses the SCS-CC2 approach to describe the electronically excited states (localized to a dimer). Force field (molecular mechanics, MM) approaches are employed to incorporate the steric restrictions arising from the crystal environment. Since the main focus is on the electronic states of a dimer of PTCDA (or DIP) in their arrangements as found in crystals, the surrounding is described with a polarizable force field which is capable to describe the crystal structure accurately (see below). The crystal environment is approximated by a large cluster of surrounding molecules. It comprises three layers around the inner dimer which can adapt to motions of the inner dimer. They are surrounded by a fourth layer which is fixed at the crystal geometry. This system allows investigating the relaxation of the surrounding molecules as found in the crystal lattice as a response to a given (frozen) configuration of the central dimer.

The ground state energy of the whole system is calculated as follows (subtractive scheme):

$$E\left(\frac{QM}{MM}\right) = E_d(QM) + E(MM) - E_d(MM) \quad (115)$$

where $E_d(X)$ is the dimer intermolecular energy calculated at the respective level $X$ ($X = QM$ or $MM$). $E(MM)$ is the energy of the whole cluster geometrically optimized by specially developed

force fields by Dr. M. Tafipolski (see below).[204] Dimer excitation energies (corrected with Apéry's constant, see below) are added to the ground state energy $E(QM/MM)$. The mechanically embedded QM/MM approach includes all steric interactions between the dimer and the environment. It also allows the adaption of the surrounding to photo-induced motions of the dimer. It only partially covers additional polarization effects arising due to the crystal environment. However, as discussed in chapter 7 such effects would even increase the efficiency of the trapping process rather than stop it.

It is well established that the so-called Davydov splitting of the Frenkel states results from the electronic coupling between excited states of two molecules.[114,205,206] This coupling is dominated by the dipole-dipole or Förster interaction of the oscillating transition dipoles of both monomers during the excitation process. Due to the close packing for adjacent chromophores in the crystal structures, additional Dexter interactions[207] become significant. Both interactions are properly represented by the supermolecule approach for the dimer applied in the present work. However, in a crystallite, other important interactions have to be considered which arise from further adjacent molecules and from molecules in the π-stack of the crystal. They cannot be neglected as the dipole-dipole interaction decays relatively slowly as $1/R^3$, where R is the distance between the monomer centers. The importance of such interactions was also underlined by a recent paper of Gierschner et al.[208] The missing interactions could, in principle, also be calculated with the supermolecule approach. However, such an approach is too demanding due to the relatively slow convergence of the dipole-dipole interactions and the complex dynamic polarizations between donor and acceptor molecules.[206,209-211] Already the computation of a trimer is not feasible. For that reason, the missing interactions are approximated by assuming that the interactions of the molecules along the π-stack decay according to the dipole-dipole rule. Interactions with molecules not belonging to the π-stack are neglected. Using this assumption, the excitation energies $\Delta E_s^i$ of the two Frenkel states $i = \{1,2\}$ in the solid are calculated to be at

$$\Delta E_s^i \approx 2 \cdot \left(1 + \frac{1}{2^3} + \frac{1}{3^3} + \frac{1}{4^3} + \frac{1}{5^3} + \cdots\right)\left(\Delta E_d^i - \Delta E_m\right) + \Delta E_m \quad (116)$$

$$\Delta E_s^i = 2 \cdot \zeta(3) \cdot \left(\Delta E_d^i - \Delta E_m\right) + \Delta E_m$$

where $\zeta(3) \approx 1.202$ is Apéry's constant.[212,213] $\Delta E_d^i$ and $\Delta E_m$ are the excitation energies calculated for the dimer and monomer, respectively. As a consequence, in this approximation the Davydov splitting of the PBI chromophores in a crystal is increased by a factor of about 2.4 compared to the dimer one (see Figure 11).

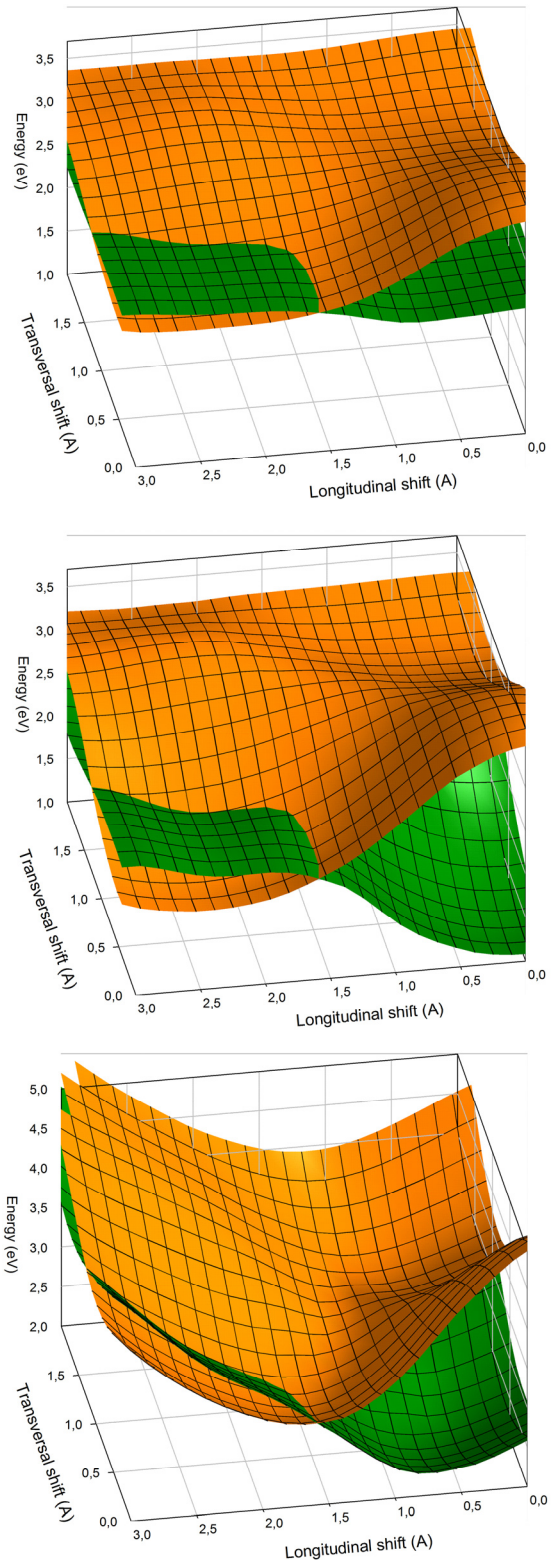


**Figure 11: PESs of the bright ($S_2$, orange) and dark ($S_1$, green) Frenkel state: The pure dimer curves provided by SCS-CC2/SVP (top); Two times the Apéry's constant is used to account for increased state splitting in the π-stack (middle); a mechanical embedding QM/MM approach is additionally employed to represent the crystal surrounding (bottom). Only the last PESs are used to derive the exciton self-trapping mechanism introduced in chapter 5.2.**

For the *intramolecular* interactions in PTCDA and DIP a modified versions of the AMOEBA polarizable force field was used by Dr. M. Tafipolski.[214] They have been developed based on the monomer calculations to reproduce B3LYP/cc-pVDZ optimized geometries and the Hessian matrix (especially low-frequency modes < 200 $cm^{-1}$) to allow energy minimizations of the big cluster (excerpt from the crystal structure, see above) using fully flexible monomers needed for QM/MM mechanical embedding calculations. For $\alpha$-PTCDA the *intermolecular* electrostatic energy could be accurately described with atom-centered multipoles up to quadrupoles calculated with the Distributed Multipole Analysis (GDMA) program.[215,216] Nevertheless, an extended re-parameterization of the standard parameters of the AMOEBA force field by Dr. M. Tafipolski was necessary to achieve accurate geometries.

Even after extended re-parameterization the AMOEBA polarizable force field could not reproduce the geometrical structure of the DIP crystal.[76] Hence, a recent approach was employed which includes the short-range charge-penetration term in a force field.[204] For this short-range term the parameters were used as recently optimized for benzene crystals without further modification. Additionally, the van-der-Waals terms were re-parameterized so that the force field reproduces the physically well-defined components of the intermolecular energy (electrostatic, exchange-repulsion, dispersion and induction) predicted by the symmetry-adapted perturbation theory. The new force field accurately reproduces the crystal structure of DIP in thin films.

**Solvent model calculations**

The calculations regarding solvent effects in chapter 7 are performed in a slightly different way. The geometry of the considered chromophore monomers were optimized with the dispersion corrected DFT method[188,189] BLYP[190-192,217,218] using the Turbomole 6.0 package.[201] For all non-hydrogen atoms the TZVP basis set was used and for hydrogen atoms the TZV basis set.[193,200] This combination is called TZV(P) in the following. In the literature it was shown that the binding energies resulting from BLYP-D/TZV(P) and SCS-MP2/QZVPP computations are very similar.[168] Additionally, a PBI dimer with a small molecular solvent shell of twelve methane molecules was geometry optimized on the same level of theory. The solvent molecules are arranged in a way around the imide groups that a $C_2$ symmetric structure is retained (see Figure 12). In the optimization all atoms belonging to the perylene core were kept fixed at their positions in the monomer geometry in order to prevent a folding of the dimer.

Dimer systems are taken as a model for larger aggregates.[219] They are built up as π-stacks with a distance of 3.3 Å which corresponds to the optimal distance of non-relaxed PBI dimers determined by the mentioned dispersion corrected DFT method. To investigate variations in energy order and characters of the involved states as a function of the relative orientation of both monomers, PECs are

computed which describe a torsion motion along the stacking axis of the two monomers from 0° to 90° (see Figure 10). The calculations were performed with the Gaussian 03 package[220] using the 6-311G**[221-224] basis set for all atoms in combination with the BLYP-D functional.

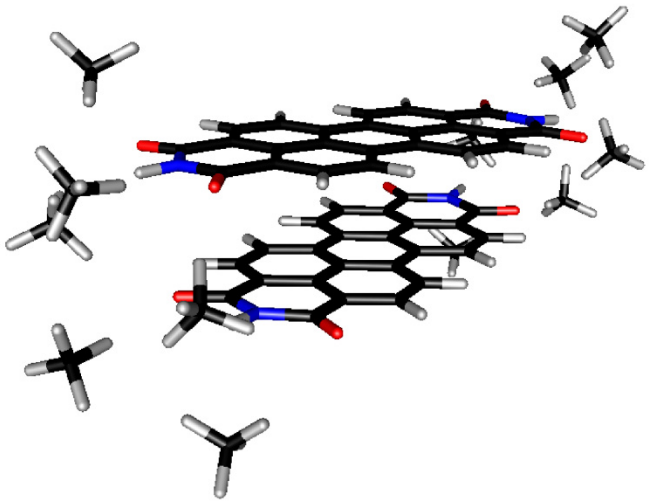

**Figure 12: Optimized geometries of a 30° rotated PBI dimer with a small solvent shell of 12 methane molecules.**

The excited state properties were calculated with TD-HF/6-31G**.[225-229] To account for dispersion effects, PECs of the excited states were approximated by adding the excitation energy to the dispersion corrected BLYP ground state energy. This method is called TD-HF-D in the following. In a former work this method was compared to SCS-CC2.[230] Trends in the PECs are correctly reproduced, while the excitation energies of the charge-transfer (CT) states are overestimated.

As solvents water ($\varepsilon$ = 78.39, $n$ = 1.333) and cyclohexane ($\varepsilon$ = 2.028, $n$ = 1.424) is studied to include environments with large dielectric constants $\varepsilon$ as well as high refractive indexes $n$.[220] The integral equation formalism variant of the polarizable continuum model (IEFPCM)[231-234] is employed for the description of excited state properties in solution which is widely used for this purpose.[229,235-240] For very fast processes like optical transitions the polarization response of the solvent can be divided into a fast and a slow component.[241] The fast one refers to the electronic polarizability of the solvent and is expected to happen at the same time scale as the excitation process itself. The slow component is due to structural reorientation (mostly rotation) of the solvent molecules. This happens on a much slower time scale. Accordingly, optical transitions have to be described in a so-called "nonequilibrium" regime.[234] Also the dielectric constant has to be separated into two constants. The first one is the static dielectric constant ε describing the unperturbed solute-solvent equilibrium. It influences ground state properties by changing the electron distribution and thus the structure of the molecule. The second one describes the polarization of the electron density which is fast enough to follow the

oscillatory fields during an excitation process. This is the fast dielectric constant $\varepsilon_f = n^2$, where $n$ is the refractive index.[241] The surrounding influences the excitation energies and transition moments via $\varepsilon_f$.

In order to get a reliable energetic order of Frenkel and CT states in a polarizable surrounding, higher order methods like SCS-CC2 has to be used for which a polarizable continuum model (PCM) procedure is not feasible as mentioned before. In a first approach the solvatochromic shifts calculated by TD-HF are just transferred directly to SCS-CC2/SVP[181,194,196-198] results under vacuum conditions. This simple method is tested for its reliability by a linear model which relates the solvatochromic shits to properties calculated under vacuum conditions. It uses linear relations between the solvatochromic red shift $\Delta E^{ex}$ of the excitation energy $E^{ex}$ and the squared transition dipole moment $\mu^2$ in solution as well as a linear relation of the oscillator strength in solution and under vacuum conditions. According to the description of Bayliss the solvatochromic shift is given by

( 117 ) $$\Delta E^{ex} \sim \frac{\mu^2}{R^3} \cdot \frac{n^2-1}{2n^2+1}$$

where $R$ is the radius of a spherical cavity and $n$ the refractive index.[242] The transition dipole moment is also influenced by a polarizable surrounding. However, in this context it is more convenient to discuss the oscillator strength $f$. These two properties are related by

( 118 ) $$f = \frac{2}{3}\frac{m_e}{\hbar^2 e^2} E^{ex} \mu^2$$

where $m_e$ is the mass of the electron and $e$ the electric charge of the electron.[243] The relation between the oscillator strength in vacuum $f^{vac}$ and solution $f^{sol}$ is given by Chako's formula:[244]

( 119 ) $$f^{sol} = f^{vac} \frac{\left(n^2+2\right)^2}{9n}$$

The above realtions are valid for spherical cavities. Deviations are expected for the more complicated shaped cavities of PCM approaches. Therefore, linear relations have to be parameterized which is introduced in the following. Solvatochromic shifts are calculated on TD-HF//IEFPCM level of theory for different geometries. Structures with different torsional angels around the stacking axis are ideal for this purpose due strongly varying oscillator strengths.[230] The oscillator strength under vacuum conditions $f^{vac}$ is related to the one in solution $f^{sol}$ by:

( 120 ) $$f^{sol} = c^f f^{vac}$$

Here, $c^f$ is a fit parameter which will be determined according to the introduced set of different dimer geometries. The solvatochromic shift of the excitation energy $\Delta E^{ex}$ is related to the transition dipole moment in solution $\mu$, which is given by equation ( 120 ), by:

$$\Delta E^{ex} = c^{ex}\mu^2 + \Delta E_0^{ex} \qquad (121)$$

In equation ( 121 ) $c^{ex}$ and $\Delta E_0^{ex}$ are fit parameters. In the case of excitations into Frenkel states of a dimer, each monomer gives rise to an oscillating transition density with a large transition dipole moment. For the dark Frenkel state the two moments point in opposite directions and, thus, cancel each other. However, a transition density of higher order remains causing short-range interactions with the solvent molecules. They lead to large solvatochromic shifts of the excitation energy $\Delta E_0^{ex}$ at zero transition dipole moments for which a parameter is introduced in ( 121 ). For the same reason it makes sense to distinguish between Frenkel and CT states for linear relations. The latter states possess a vanishing transition dipole moment on a first glance and no solvatochromic shift is expected. However, due to mixing with Frenkel states they gain some transition dipole moment. This will cause some solvatochromic shift of the excitation energy, but only a very small shift at zero transition dipole moment is expected. Additionally, a stabilization of the resulting charges could occur which will increase the value for $c^{ex}$ of CT states.

**Pitfalls**

In order to avoid problems during the diverse iterative processes in the IEFPCM calculations, it is necessary to disable the symmetry of the cavity (key word NOSYMMCAV at the end of the input file). Also Bondi atom radii were used to end up with only one cavity. For other atom radii, e.g. Pauling radii, two separated cavities were found for a PBI dimer at 3.3 Å distance. An example for a Gaussian03 input file is:

```
#P HF td=(NStates=20)/6-311G** SCRF=(IEFPCM,Read,Solvent=Water)

Solvent model calculation for water

0 1
[Geometry]

NOSYMMCAV
RADII=BONDI
```

Gaussian always gives out the first *N* excited states. If one is interested in the CT states, it turned out that for certain dimer arrangements, e.g. parallel ones, a large number of excited states must be calculated. A number of 20 excited states was always enough for the calculations performed in for this thesis. The used values for the fast $\varepsilon_f$ and slow $\varepsilon$ dielectric constants are:

**Table 1: List of all used fast and slow dielectric constants within this thesis.**

| solvent | ε | $\varepsilon_f$ |
|---|---|---|
| cyclohexane | 2.02 | 2.028 |
| dichloromethane | 8.93 | 2.020 |
| acetonitrile | 36.64 | 1.806 |
| water | 78.39 | 1.776 |

For all dimer calculations it was necessary to take care that the self-consistent field converges on the correct root. In most cases it was sufficient to perform a reference calculation, which was used as an initial guess for the wave function in the productive runs. By using Turbomole it was helpful to use smearing of the occupation number by enable the Fermi option in the “SCF options” in “define”. If this recipe fails, it is always useful to reduce the basis set size or to use a higher order point group for the system under study to achieve a well-converged reference wave function.

In Turbomole the irreducible representation of the questioned excited states has to be specified. During reading the coordinates from a file by “define”, the system is automatically rotated. Therefore, the irreducible representation of the wanted state could change, e.g. from $B_{3u}$ to $B_{1u}$, caused by the rotation. One should always review if the correct states are specified.

# 5. Exciton self-trapping in perylene based materials

## 5.1 Exciton self-trapping in helical aggregates

A part of this chapter will be communicated in a manuscript for publication: A. Schubert, V. Settels, W. Liu, F. Würthner, C. Meier, R. F. Fink, S. Schindlbeck, S. Lochbrunner, B. Engels, V. Engel, *submitted*. Quantum dynamic calculations were performed by A. Schubert (Universität Würzburg).

**Abstract**

*The fast and efficient transport of energy absorbed from light is of central importance in photosynthesis as well as photovoltaic processes. In this context molecular π-aggregates play a central role as, e.g., coupled chromophores in light harvesting complexes or dye molecules in organic semiconductor devices.[42,245,246] What limits the energy transfer are de-excitation mechanisms leading to a trapping of energy on local sites and it is thus of great interest to obtain a basic understanding of such self-trapping processes. The molecular dimer is an important sub-unit of aggregates and it has been shown that, after excitation, the energy tends to localize very fast in these subunits.[147] Therefore, in what follows, elementary processes taking place after photo-absorption are discussed in dimers.*

The electronic structures of excited molecular dimers can be mainly described by the configurations indicated in Figure 13. States with Frenkel character arise from local HOMO-LUMO excitations on one monomer. They will be called Frenkel excited states in the following. These Frenkel excited singlet states interact via the strong and long ranging Förster coupling (see Figure 5). It is mainly responsible for the exciton energy transfer (EET)[114,247] and is reflected in the corresponding spectra by Davydov splitting (see Figure 6). Local excited states with triplet coupled spins (Figure 13, left hand side) interact via short ranging Dexter coupling (see Figure 5), which can, nevertheless, lead to significant triplet exciton diffusion lengths as in general the life time of the triplet states exceeds that of the respective singlet states by orders of magnitude.[248-252] States with charge transfer (CT) character (Figure 13, two right hand panels) arise by excitation of an electron from one dye molecule to another one in close proximity. In a dimer model two Frenkel ($M^*M$, $MM^*$) and two CT states ($M^-M^+$,$M^+M^-$) exist for singlet and triplet states (M: one monomer of the dimer). Coupling between the pairwise degenerate states leads to four separate energy levels. The computed adiabatic states contain admixtures of both types of configurations as the effective energy differences of the related diabatic states are in general small compared to their coupling.[114,202,230,247]

The separations of the four singlet (triplet) states depend on the coupling strength which is crucially determined by the nuclear geometry. The variation of the latter turns the levels into potential hyper-surfaces which, in the simplest case where a single reaction coordinate $q$ can be identified, are potential energy curves $V(q)$. Based on such curves, which are obtained from *ab initio* electronic structure calculations, in this chapter a new mechanism for rapid energy relaxation is proposed for aggregates of PBI in solution. The most important ingredients are motions on non-adiabatically coupled electronic states of Frenkel and CT character. It has to be noted that the latter are usually not taken into account. If, after photo-excitation, the system can relax to the crossing regions on a time-scale faster than that of a Förster energy transfer, a population transfer takes place to the lower lying excited states resulting in an efficient self-trapping of the exciton.

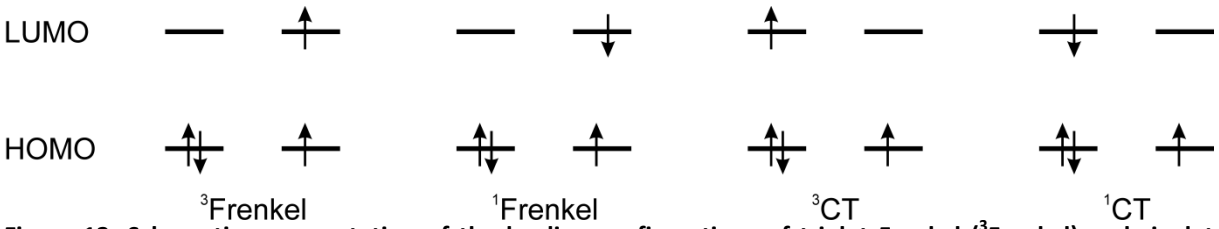


**Figure 13: Schematic representation of the leading configurations of triplet Frenkel ($^3$Frenkel) and singlet Frenkel ($^1$Frenkel) as well as triplet charge transfer ($^3$CT) and singlet charge transfer ($^1$CT) states in terms of localized HOMO and LUMO orbitals. Each configuration is represented with four orbitals, the two LUMOs (upper lines) and the two HOMOs (lower lines) which are localized on one or the other monomer, left and right, respectively.**

Recently aggregates of PBI in methyl-cyclohexane were investigated experimentally and theoretically[168] to understand the optical properties of such important building blocks for organic electronics.[96,253] The picture which evolved can be summarized as follows: According to the dimer transition dipole geometry with monomer moments at a relative angle of 30°, the upper of the two states resulting from the splitting of the Frenkel states is preferentially populated. By some unidentified mechanism, relaxation to the lowest excited state takes place. Thereby, the two monomers orient to have parallel transition dipole geometry. Radiative decay to the ground state, which is forbidden for the exact parallel configuration, is only possible if nuclear degrees of freedom are incorporated and, as a consequence, a long emission lifetime and a low fluorescence yield as compared to the monomer case are found.[254] Due to the flat excited state torsional potential the red-shifted emission band is broadened significantly. The final fluorescing state represents a trap for excitons due to a loss in energy of around 1 eV and the described geometrical distortion. Up to this point, a consistent picture of the absorption and emission properties could be established. However, a more fundamental insight into the decay dynamics and the reaction path which leads to the fluorescing state is missing. This would yield an atomistic understanding of exciton self-trapping in PBI aggregates in solution.

Lochbrunner and co-workers performed femtosecond transient absorption measurements in order to investigate the nature of the self-trapping process.[255] The measured absorption change is composed by three components (see Figure 14). One is a step function reflecting the bleach which is switched on with excitation and does not change thereafter. An exponential decay with negative amplitude resembles stimulated emission and decays with a time constant of 215 fs. The last component is an oscillatory contribution with a period of 381 fs. As a key result, the data shows that the excited state is de-populated on an ultrafast time scale. Such a rapid decay cannot be explained with the previously discussed non-adiabatic dynamics along the torsional degree of freedom involving only the Frenkel states, because they do not interact sufficiently strong in the relevant region of coordinate space.[168] Additionally, due to the large moment of inertia, the torsional motion is very slow so that the angle of 60°, where a curve crossing between the higher and the lower Frenkel state occurs, cannot be reached on a femtosecond time scale. Thus, there must be present a different geometry change which makes the non-adiabatic transition effective.

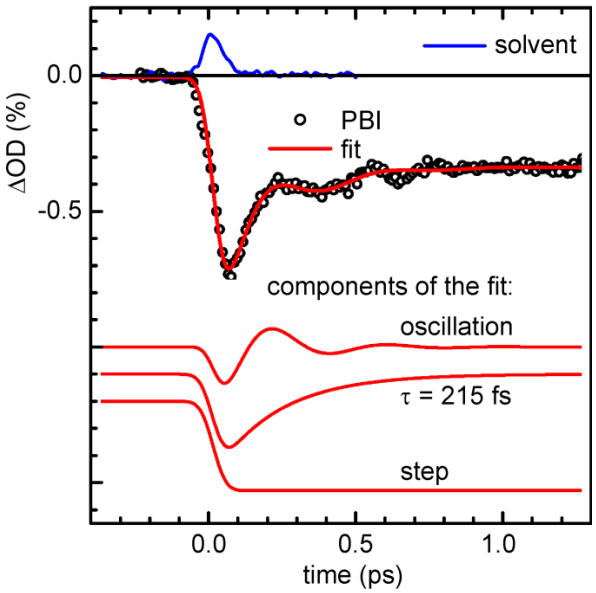


**Figure 14: Time-dependent absorption change ΔOD at 520 nm (open circles) measured by Lochbrunner and co-workers, signal of the pure solvent (upper fine line) and model function fitted to the data (thick solid line). The three lower lines show the contribution to the model function. They are shifted to lower ΔOD values for better visibility.[255] The figure is reproduced with kind permission of Prof. Dr. S. Lochbrunner.**

Depopulation of the initially excited Frenkel state is expected to occur via a barrier-free motion with a small motion of inertia, which couples this state to the lower lying dark Frenkel one. As a result, motions of molecules relative to each other can be excluded due to the high moment of inertia. One potential de-population mechanism can be derived by the following thought: In the case of a perfect localization of the excitation onto one monomer, Davydov splitting disappears and the Fren-

kel states become degenerated. Afterwards, the exciton can relax in the lowest lying Frenkel state, which again should induce a Davydov splitting. This motion can potentially be realized by relaxing one monomer to a structure ($M^*$), which is optimal for its first excited state, and keeping the other fixed to its ground state structure (M). In order to do so, the PBI monomer structure was optimized for the optically bright 1 $^1B_{2u}$ state using SCS-MP2/TZV(P) level of theory. The dimer is then arranged at the inter-monomer configuration with a center-of-mass separation of 3.3 Å and a torsion angle of 30°. A reaction coordinate is introduced which linearly relates the initial ground state (MM) configuration with coordinates $\vec{R}_i$ to the final ($MM^*$) configuration with coordinates $\vec{R}_f$ as $\vec{R} = \vec{R}_i + q(\vec{R}_f - \vec{R}_i)$, where $\vec{R}$ collectively denotes the coordinates of all nuclei. For this motion the ground state is calculated by SCS-MP2/SVP and excitation energies by SCS-CC2/SVP. Figure 15 shows the resulting potential energy curves.

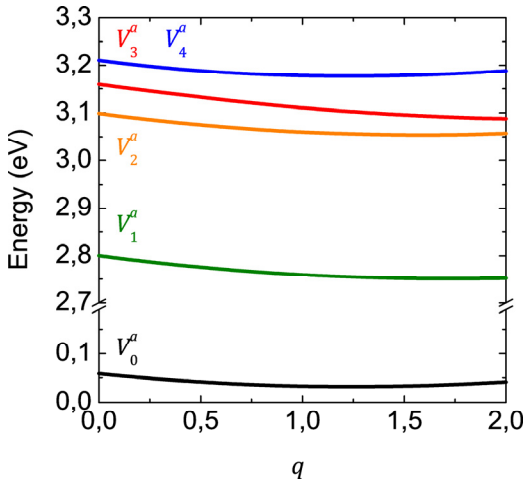


**Figure 15: Potential energy curves of the ground and first Frenkel and CT excited states for a PBI dimer. A motion is considered, in which one monomer changes its structure from the ground state geometry ($q$ = 0) to the optimized excited state structure ($q$ = 1) while the other monomer is fixed.**

All states are stabilized during the motion. The effect is moderate for the ground state, which reaches a minimum for $q$ = 1.2. Here, its energy is 0.03 eV lower than at the starting point ($q$ = 0). An explanation for this finding could be that at $q$ = 0 the dimer is build up by a SCS-MP2 optimized ground state structures. This structure is different from the optimized structure of the dimer (see chapter 6.1). Therefore, a structural change of the dimer could also stabilize the ground state. The energy stabilization of the excited states ($V_1^a$: 0.05 eV; $V_2^a$: 0.05 eV; $V_3^a$: >0.07; $V_4^a$: 0.03) is larger than the one of the ground state. Unfortunately, along the potential energy curve (PEC) the Davydov splitting between the Frenkel states $V_1^a$ and $V_2^a$ increases slightly ($7 \cdot 10^{-3}$ eV from $q$ = 0 to $q$ = 2) instead the expected decrease, which indicates that the excitation does not localize during this motion.

Interestingly, the lowest CT state ($V_3^a$) shows the largest stabilization out of the calculated states (see Figure 15). Consequently, a motion stabilizing this CT state could be more promising as the one discussed until now to de-popultate the bright Frenkel state ($V_2^a$). At the vertical excitation geometry, one finds that the states for the Frenkel and the (energetically higher) CT configurations are close in energy (about 0.04 eV, see Figure 16). It is then not unlikely that, upon a geometry deformation, this gap decreases so that strong mixing of these states occurs. To clarify this situation, the influence of a deformational motion of a PBI dimer connecting the ground state structure to the geometry $M^+M^-$ was considered, optimized for states with (approximate) charge-transfer character. In the $M^+M^-$ structure, one monomer has changed its structure from the ground state geometry (M) to the one optimized for the anion ($M^-$) and the other monomer to the one optimized for the cation ($M^+$). In a dimer with $M^+M^-$ geometry, one expects that the CT state is stabilized, which yields $M^+M^-$, and the other CT is destabilized, which end up with $M^-M^+$. Due to problems with spin contamination in HF calculations, the monomer structures of the anion and cation were optimized using B3LYP-D/TZV(P). A dimer was constructed in away similar to the former one with a intermolecular distance of 3.3 Å and a rotation around the stacking axis of 30°. Also, a reaction coordinate from the ground state structure (MM) to the $M^+M^-$ structure is introduced similarly to the one for the motion to the $MM^*$ structure. Ground state energies for the motion are calculated with SCS-MP2/SVP and excitation energies with SCS-CC2/SVP.

In Figure 16 (upper left panel), adiabatic potentials $V_{n_a}^a(q)$, of the lowest excited singlet states 1 - 4 $^1$B are displayed (full lines). With a deviation of approximately 0.08 eV, the relative position of the two bright adiabatic states (denoted as $n_a$ = 1, 2 in the figure) is in agreement with experiment.[168] The absolute position of the potentials deviates by 0.4 eV from the measured absorption peak. Here one has to keep in mind that the calculation is performed for gas-phase dimers so that effects of higher order aggregation and solvent interactions are not included. Photon excitation from the ground state into the main absorption band at 480 nm (higher energy Frenkel state) results in the population of state ($n_a$ = 2) at $q$ = 2. As anticipated, the deformation introduces energy shifts of the potentials and an avoided crossing between the states ($n_a$ = 2, 3) around $q$ = 0.4 can be identified. The lower left panel of Figure 16 shows curves which represent the amount of CT character of the respective adiabatic electronic states.[202,203] Thus, at the excitation configuration ($q$ = 0), the two lowest states are mainly Frenkel of character.[230] An increase of $q$ leads to a strong interaction between the states, and the excited Frenkel state acquires CT character whereas the lower CT state becomes mostly Frenkel. Thus one may envision a non-adiabatic transition opening a reaction path which, eventually, will lead to an exciton self-trapping in the lowest state. It is worthwhile to mention

that, in going from one to the other geometry (i.e. from $q$ = 0 to $q$ = 1), the atomic positions are not changed dramatically where a deviation in position is about 0.01 Å, in the average.

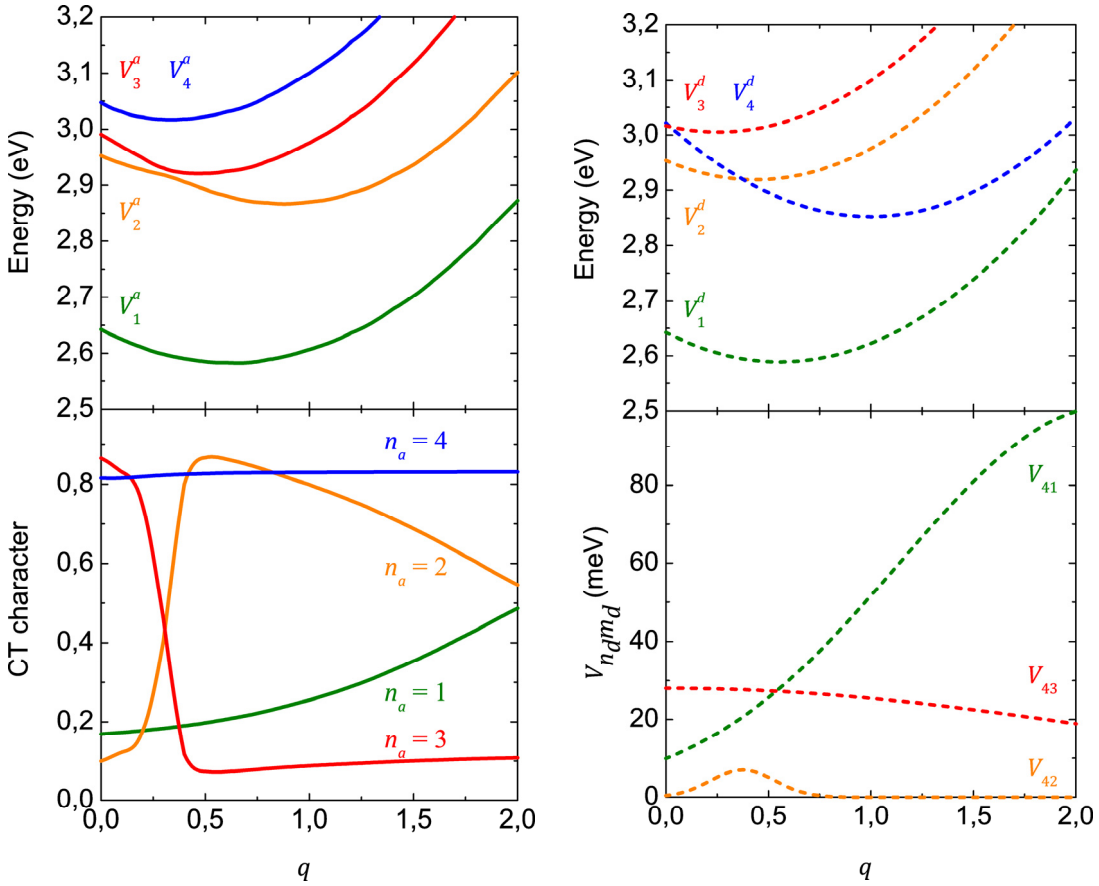


**Figure 16: Upper panel: Adiabatic excited state potentials as a function of the reaction coordinate $q$. The lower panel contains the percentage of CT character of the different adiabatic states. The vertical line at $q = 0$ indicates the geometry accessed by photo-absorption from the ground state. The value of $q = 1$ corresponds to the structure in which the monomers of the dimer take the $M^+$ and $M^-$ geometry, respectively.**

The electronic properties associated with the various excited states exhibit a strong coupling with increasing reaction coordinate $q$. The non-adiabatic, kinetic coupling elements can therefore be expected to be very strong. For example, the permanent dipole moments (shown in Figure 17) document a mixing between the states $V_1^a$ and $V_2^a$ and also between states $V_2^a$ and $V_3^a$. Another indication for the coupling is the variation of the charge transfer characters of the adiabatic states, which are shown in the lower left panel of Figure 16. The charge transfer characters are found from a careful analysis of the *ab initio* wave functions based on localization of the dimer wave function to a monomer basis.[202] This method, of course, is only valid for mixing charge transfer states with Frenkel ones. The coupling between the two charge transfer states is implemented due to the expected degeneracy for localized charge transfer at $q$ = 0 for symmetry reasons. The state $V_4^a$ ($V_3^a$) is included in the simulation, however, it does not participate in any way in the dynamics discussed here.

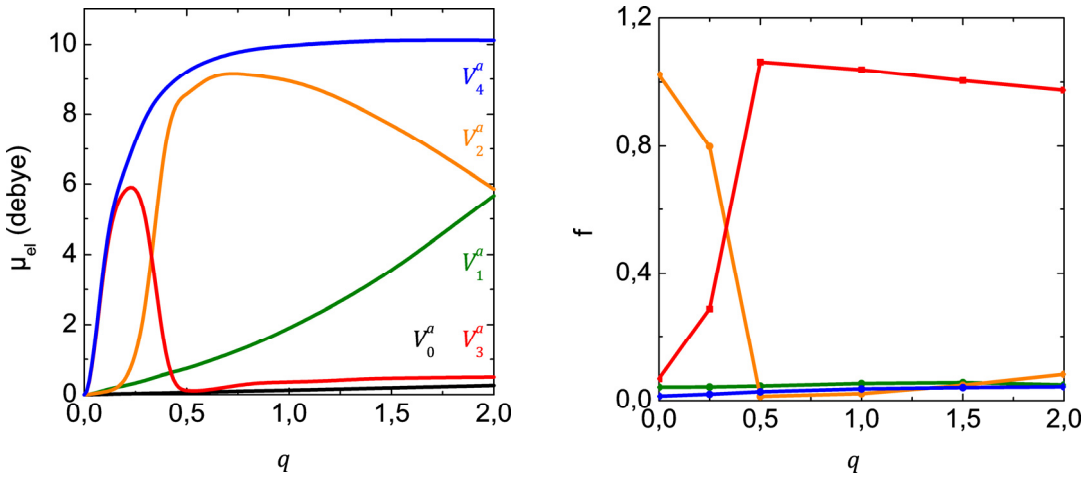


**Figure 17: Electric permanent dipole moments (left panel) and oscillator strengths f (right panel) are shown for the different excited states, as indicated. The data relies on SCS-CC2/SVP calculations and is determined for a motion of a PBI dimer along the coordinate $q$. The amount of oscillator strength in the $V_2^a$ and $V_3^a$ state is interchanged during the motion. This supports a change in character of both adiabatic states, which is in line with the derived diabatization scheme. The permanent dipole moment supports the diabatization scheme as well. At small $q$ values the $V_3^a$ state possesses a significant dipole moment. At larger $q$ values the dipole moments of the states $V_2^a$ and $V_3^a$ interchange similarly to the oscillator strength. This indicates a non-adiabatic coupling between these states. At even larger $q$ the dipole moment in the $V_2^a$ state is shared with the $V_1^a$ state. This indicates a non-adiabatic coupling between these states as well. All findings are in line with the analysis of the CT character of the wave functions of the excited states, which is the basis for the employed diabatization scheme.**

Nuclear wave packet dynamics along the reaction coordinate $q$ were performed by A. Schubert.[256,257] The time-dependent Schrödinger equation was integrated numerically[258] incorporating a potential energy matrix with the diabatic potential curves displayed as dashed lines in Figure 16. The coupling elements $V_{n_d m_d}(q)$ was chosen as Gaussians of various widths and only the couplings $V_{14} = V_{41}, V_{24} = V_{42}$ and $V_{34} = V_{43}$ was taken as non-zero. The diabatic curves are obtained as cubic fits to the *ab initio* potential energy curves outside the coupling regions. The coupling elements are taken to be Gaussians of the form $V_{ij} = A_{ij}\exp\left(-\beta_{ij}\left(q - q_{ij}\right)^2\right)$. The centers $q_{42}$, $q_{43}$ of the couplings $V_{42}$ and $V_{43}$, are determined by the crossing of the charge transfer character curves. The amplitudes $A_{ij}$ are given by half of the potential curve spacing at these points. The width of the coupling curves (i.e. the values of the parameters $\beta_{ij}$), are fitted such, that a diagonalization of the diabatic potential matrix yields perfect agreement with the *ab initio* curves. It has to be noted that the proposed self-trapping mechanism relies on the existence of the couplings which were revealed by means of high level *ab initio* approaches and not on their particular form, so that other diabatization schemes may be employed which do not alter the underlying physics.

The initial wave function was the vibrational function in the electronic ground state derived from the Hamiltonian including the ground-state adiabatic potential $V_0^a(q)$ (not shown in Figure 16). Dissipation was included by adding the operator $H_n^{diss} = -i\lambda H_n$ to the Hamiltonians $H_n$ in the diabatic

state ($n_d$), where $\lambda$ is an adjustable parameter. The wave function was re-normalized after each propagation time-step $\Delta t$ as it is done in stochastic wave function approaches.[259,260] A. Schubert treated the excited state dynamics de-coupled from the dimer ground state because radiative transitions from the excited state manifold occur on a nanosecond time-scale[254] whereas here processes taking place on a femtosecond time-scale are concerned.

In Figure 18, the populations in the diabatic states computed by A. Schubert are shown. In calculating these curves a value of $\lambda$ = 0.07 is employed. For this value, the energy dissipation in the photo-excited diabatic state ($n_d$ = 2), neglecting all couplings, is such that the vibrational ground state is reached in about 200 fs. As can be taken from the figure, the population of the initially prepared state decays on the same time-scale as determined in the experiment. Remarkably, the intermediate CT state ($n_d$ = 4) is populated only to a small amount so that the population is directly transferred to the lower state ($n_d$ = 1) of predominantly Frenkel character. This is consistent with the experimental finding of Lochbrunner and co-workers that no anionic of cationic bands are seen in transient spectra recorded with a white light continuum as broadband probe pulse; e.g., PBIs in complexes exhibiting photoinduced electron transfer lead typically to a pronounced excited state absorption band around 700 nm[261,262] which is not observed here. The effective population transfer to the lowest excited state can be traced back to the broad coupling region (ranging from $q$ = 1 to $q$ = 3.3) between the two lowest diabatic states. The probability densities of the diabatic wave functions in state ($n_d$ = 1) and ($n_d$ = 2) are shown in Figure 18. The initially prepared wave packet moves periodically, thereby loosing energy until its mean energy corresponds to that of the curve crossing. Then, very quickly, the density is transferred via the doorway state ($n_d$ = 4) to the lowest state where it is accumulated around the respective potential well.

The population of the initially populated state does not show the oscillatory behavior which is seen in the wave packet dynamics. There, a period of $T_q$ = 41.3 fs (corresponding to an energy of $\Delta E_q$ = 0.10 eV) can be determined. Compared to the time-resolution of the experiment this is rather fast and difficult to detect. Regarding the spectral width of the experimental pump-pulse (which is about 0.12 eV), vibrational wave packets can only be prepared if states with an energy spacing less than the pulse-width are coherently excited. Thus, e.g., the C-C stretching vibration at 0.175 eV, which is prominent in the monomer absorption spectrum[254] and also in other aggregates[263], cannot be excited. Of course, in the excited state of molecular aggregates, many vibrational levels are found.[264] If vibrations with spacing in the order of the pulse width are indeed excited, quantum beats occur. In the simplest case, a single internal vibration with spacing $\Delta E_x$ is taken into account additional to the vibration in the reaction coordinate.

To see the effect of the incorporation of an internal vibration $\Delta E_q$ = 0.10 eV was used, as determined from the wave packet calculation employing the potentials displayed in Figure 16. Choosing a value of $\Delta E_x$ = 0.11 eV (which approximately corresponds to the fastest high frequency mode which can be excited), leads to the function displayed in the lower left hand panel of Figure 18. It was convoluted with a Gaussian of 50 fs to account for the limited experimental resolution. Furthermore, the damping with a time-constant of 190 fs, as taken from experiment (see Figure 14), is included. The resulting curve very much tracks the oscillatory contribution extracted from the experimental transient absorption signal. A similar curve is obtained by using a low frequency mode with an energy spacing of $\Delta E_x$ = 0.01 eV so that this is another possibility to rationalize the experimentally seen oscillations. Note, however, that the intermolecular torsional motion which is important to explain the emission spectrum,[168] proceeds on a much longer timescale and cannot serve to explain a periodicity of 381 fs.

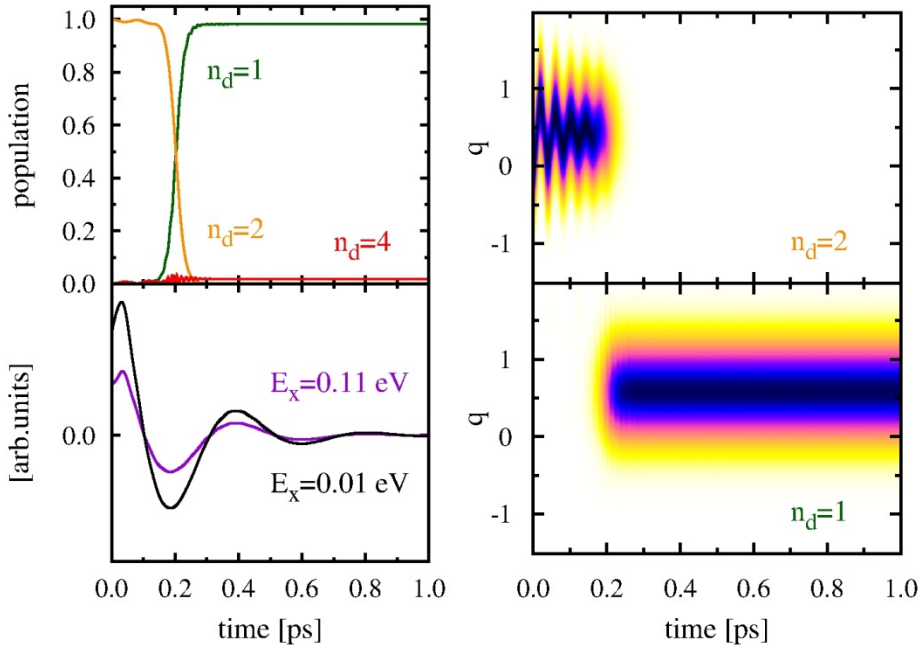


**Figure 18: Left upper panel: Population dynamics in the diabatic electronic states ($n_d$) computed by A. Schubert. Left lower panel: Damped quantum beat signals, obtained from a superposition of vibrations in the reaction coordinate and an additional internal high frequency and low frequency vibration. The right hand panels exhibit the time-dependent probability densities $\left|\psi_{n_d}^{d}(q,t)\right|^2$ in the diabatic states ($n_d$ = 1, 2), as indicated. The pictures are provided with kind permission by A. Schubert.**

To summarize, an exciton self-trapping mechanism is proposed which is based on geometry dependent couplings in excited electronic states. A deformation which does not alter the positions of the atoms significantly and thus could, e.g., be promoted by interactions with the solvent, results in a strong mixing of electronically excited states with Frenkel and CT character. Using quantum chemical-

ly calculated adiabatic potentials, a model was set up which allows for a description of the nuclear quantum dynamics. Including phenomenologically an energy dispersion into modes different from the reaction coordinate (being inter-, intra-molecular or solvent modes), leads to results which are in excellent agreement with the experimental findings, i.e., the fast de-population of the optically bright state and also the quantum beat structure found in the transient absorption signals can be reproduced. It has to be noted that other deformations than the one regarded here can be imagined which influence the couplings between the excited states. Test calculations indicate that the geometry change introduced here, is most significant for the quenching process at the ground state structure of PBI dimers while it is not possible at other aggregation structures where CT states are energetically less favorable. Extensive experimental and theoretical investigations on different molecular aggregates will be necessary in the future to investigate how general the proposed reaction path is.

## 5.2 Exciton self-trapping in crystals

Quantum dynamic calculations were performed by A. Schubert (Universität Würzburg), molecular mechanics calculations by Dr. M. Tafipolski (Universität Würzburg) and experiments by A. K. Topczak together with Prof. Dr. J. Pflaum.

**Abstract**

*The exciton diffusion length (LD) is a key parameter for the efficiency of organic opto-electronic devices and its limitation causes the need of bulk-heterojunction solar cells. Trapping processes which shorten LD significantly were carefully investigated by various experiments, but a comprehensive model providing an atomistic understanding of these processes is still missing. Such a model is proposed which is based on high-level* ab initio *computations and whose predictions are confirmed by temperature dependent exciton transport studies. The model reveals that low exciton diffusion lengths result from self-trapping processes of the optical excitation into an intermolecular immobile state which is populated through a crossing between the participating electronic states (conical intersection) on an ultrafast timescale. As the efficiency of this trapping mechanism depends strongly on molecular arrangement and environment, the model explains the strong dependence of LD on the morphology of the materials and the general shortcoming of perylene based materials for organic solar cells. The investigations are performed for perylene based materials. However, the model is applicable to many other compounds as well and provides therefore general guidelines for material design to achieve improved exciton transfer properties for future applications.*

Organic semiconductors are promising materials for thin film electronic devices, but low charge carrier mobilities and small $L_D$ values strongly limit their efficiencies in general and in particular those of organic solar cells.[13,114,265] The shortcomings are partly solved by bulk-heterojunction cell architectures. However, their complex structures entail many new problems as charge loss, reproducibility, and short durabilities.[20,60] Hence, materials with longer $L_D$, which would enable simpler architectures, are highly desirable. However, their development requires models for the underlying processes with atomic resolution[266,267] since all the tremendous recent progress made by empirical variation of device configuration obviously did not open this road.[14,44,268,269]

Perylene based materials represent one of the most stable materials among organic dyes and combine various favorable properties like intense photoluminescence as well as outstanding n-type semi-conductivity.[10] A more detailed introduction into this class of materials is given in chapter 2.2. However, highly efficient perylene based solar cells were not reported yet. The reason for this lack of

performance is still unclear. Nevertheless, absorption and emission spectra of aggregates, crystals and thin films indicate that the small $L_D$ values result from a fast depopulation of the local excited Frenkel states.[147,158] The interpretation that the population is transferred to spatially extended CT states[270] was questioned by recent experiments on neat organic semiconductors(the characters of the excited states are defined in Figure 13 at chapter 5.1). They indicated that the CT states lie energetically above their Frenkel counterparts.[262,271] Theoretical descriptions supporting the transfer to CT states by simulations based on empirical Hamiltonians[75,272] were queried by high-level *ab initio* calculations which support the recent experiments.[168,209,273] For PBI thin films transient absorption experiments identified a fast relaxation (~100 ps) of the exciton to an intermolecular, long-lived (~20 ns), immobile state which exhibits a red shifted emission spectrum.[147] Time-dependent spectroscopy on PBI doped films showed that dimer states can already be such exciton traps.[166] Raman spectroscopic measurements of $\alpha$-perylene indicated that exciton self-trapping arises from motions of two monomers relative to each other.[158] A corresponding atomistic model was provided in a recent *ab initio* based simulation of PBI aggregates which revealed an efficient self-trapping due to photo-induced intermolecular motions.[168] Related exciton–phonon coupling has also been discussed in theoretical works on exciton confinements[146,274] or relaxations to CT states.[75,211,272]

Recent experiments also provide evidence for a significant influence of the aggregation structure in the solid state on self-trapping processes.[106,167] As an elucidative example, measurements of $L_D$ for single crystalline layers showed large differences between the two perylene derivatives α-PTCDA ($L_D$=22 nm)[77] and DIP ($L_D$=100 nm)[76]. These variations are due to differences in the respective crystallographic packing, because the electronic characters of aggregates[273] and the reorganization energies of both perylene derivatives are comparable: Heinemeyer et al. determined the reorganization energies of DIP to 0.15 eV.[275] Scholz and Schreiber found experimental reorganization energies for PTCDA which varied between 0.14 eV and 0.19 eV.[276] Below, an atomistic picture is provided which explains all these experimental data and enables general guidelines for the design of improved photoactive materials.

A bottom-up approach is pursued which starts with the computation of the PESs of the relevant electronically excited states with high-level *ab initio* methods (see chapter 4 for details). Experiments show that excitons localize rapidly on bimolecular states due to exciton-phonon coupling.[146,147] Therefore, calculations were performed for dimers. They properly represent all electronic interactions including Frenkel and CT states in particular. In the second step the influence of the crystal environment is taken into account in two ways. The dimer approach accurately contains all interactions between both monomers, but neglects electronic non-next neighbor interactions.[208] They are considered via Apéry's constant, which accurately corrects the Davydov splitting from the computed

dimer value to the magnitude expected for stacks.[219] Steric constraints on photo-induced intermolecular motions imposed by the local crystal environment are taken into account by means of a hybrid approach. It combines quantum chemical methods to describe the dimer with molecular mechanics to incorporate steric influences of the local crystal environment (see chapter 4 for details).

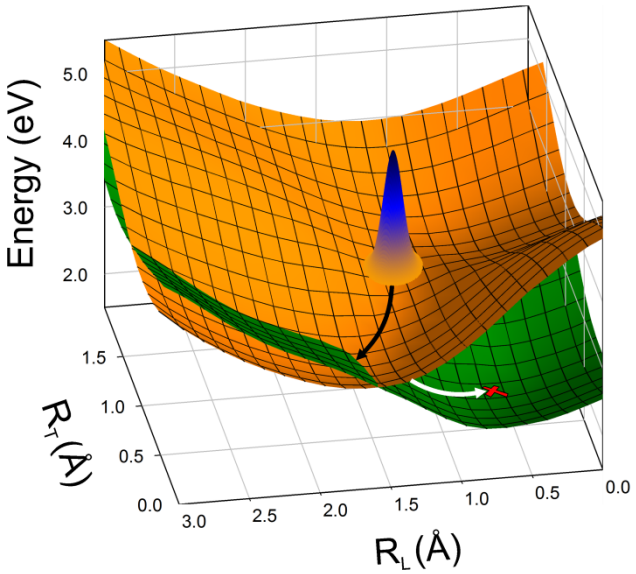


**Figure 19: PESs for the lowest excited Frenkel states of α-PTCDA as a function of longitudinal ($R_L$) and transversal ($R_T$) shifts (see Figure 20). After photo-excitation in $S_2$ (orange) the wave packet reaches a conical intersection and relaxes to the lower $S_1$ state (green).**

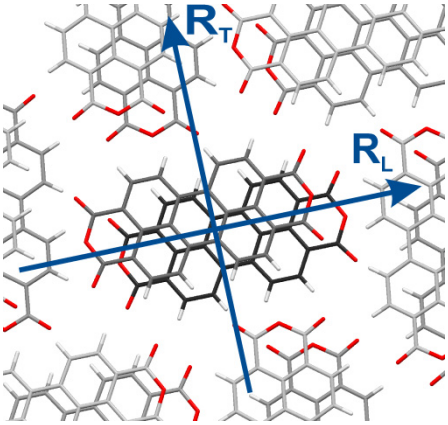


**Figure 20: Definition of $R_T$ and $R_L$ within the α-PTCDA crystal structure.**

Figure 19 shows the PESs of the two lowest excited electronic states of α-PTCDA as a function of the longitudinal ($R_L$) and the transversal shift ($R_T$) as specified in Figure 20. Both states have predominantly Frenkel character. The CT states are omitted for clarity since they are energetically well separated in the important parts of the PESs as shown in Figure 21 and Figure 22.

Due to its high transition probability, the $S_2$ state (Figure 19, orange) is initially populated after photo-excitation. In the Franck-Condon region ($R_L$ = 1.19 Å; $R_T$ = 1.05 Å), indicated as wave packet, the

potential gradient induces a barrier-free intermolecular motion (black arrow), which guides the system towards a conical intersection (CI),[277] with the lower $S_1$ state (Figure 19, green).

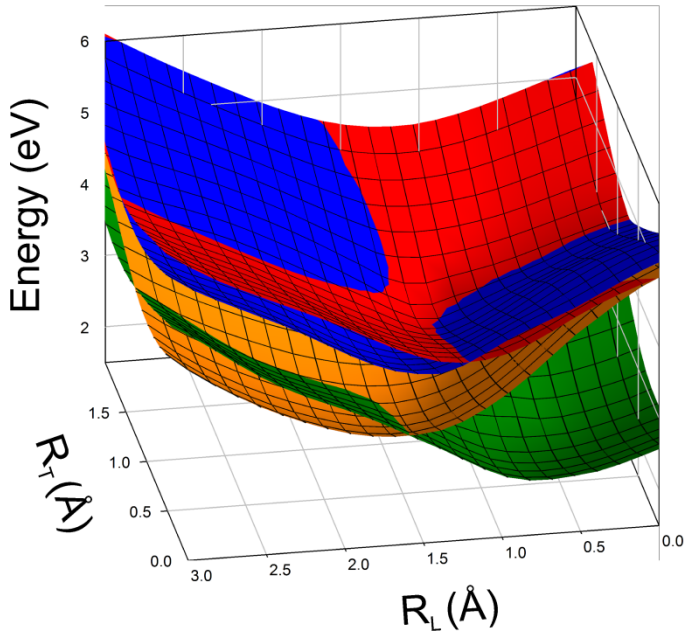


**Figure 21: PESs for the lowest excited electronic states of α-PTCDA including the CT states (red, blue) as a function of longitudinal ($R_L$) and transversal ($R_T$) shifts (see Figure 20).**

The corresponding minimal energy path from the Franck-Condon region of the $S_2$ state to the CI with the $S_1$ state ($R_L$=1.65 Å, $R_T$=0.40 Å) exhibits no barrier and the exciton is stabilized by 0.22 eV at the CI (see Figure 22). Since the transfer through a CI is very fast[277] the exciton passes over to the $S_1$ state and further relaxes to its local minimum (white arrow, red cross in Figure 19) with $R_L$ = 0.51 Å; $R_T$ = 0.47 Å which ends up with an overall energetic loss of the excion by 1.06 eV. At this point the ground state energy is increased by 0.44 eV. Consequently, the exciation energy, which is important for exciton diffusion, shrinks in total by 1.50 eV. This goes in hand with an intermolecular distortion described by the characteristic distances in Table 2. While distance A (see Figure 23) decreases from 2.39 Å to 2.22 Å, the distance D increases from 2.39 Å to 2.62 Å. Both distances are indicators for the transversal shifts, while distance C is mainly affected by the longitudinal shift. It shrinks for the motion from the Franck-Condon region to the CI (from 2.39 Å to 2.27 Å) and expands again during the motion to the minimum of the dark state (to 2.71 Å). Due to the accompanied energy loss and geometrical distortions the exciton is finally trapped.

Figure 22 offers an explanation for the shapes of the involved potential energy curves especially the opposite curvatures of $S_1$ and $S_2$ leading to the CI. The upper part shows the potential energy curves along the lowest energy path on the $S_2$ state (see Figure 19) for the ground and first four excited states. The abscissa gives the travelled distance from the Franck-Condon region (distance = 0 Å)

on the $S_2$ state. The lower plot shows the variation in the amount of CT character for the various states.

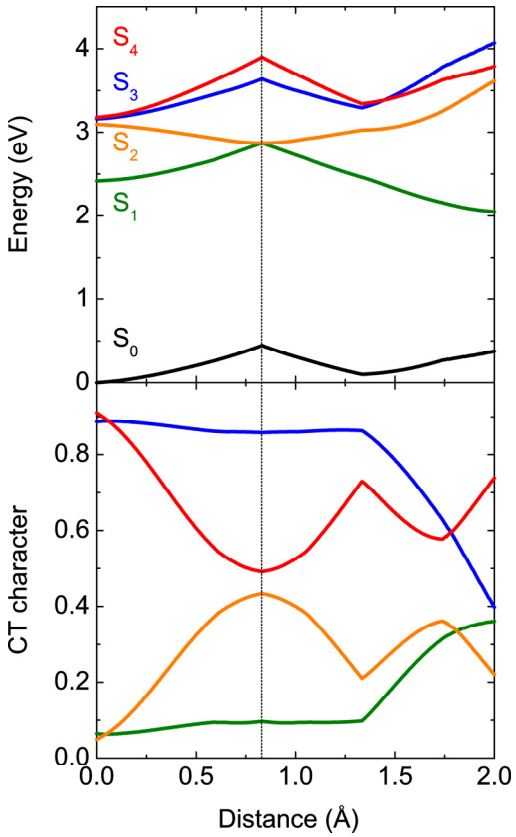


**Figure 22: Cut through the PESs in Figure 19. The abscissa gives the travelled distance along the minimum energy path measured from the Franck-Condon region of the initially populated Frenkel state ($S_2$, orange). Firstly, the graph follows the minimum energy path taken by the wave packet (black arrow in Figure 19) from the Franck-Condon region to the CI, which is indicated by the vertical line at a distance of 0.83Å. After that point the graph follows the minimal energy path in the lower Frenkel state ($S_1$, green) from the CI to its minimum (indicated as white arrow on Figure 19). The lower plot indicates the respective contributions of the diabatic CT states to the overall wave function.**

Figure 22 demonstrates that only the initially populated $S_2$ state is stabilized between the Franck-Condon region (distance = 0 Å) and the CI (distance = 0.83 Å). All other states, including the ground state are destabilized. The destabilizations result from repulsive steric interactions between the dimer molecules and the molecules of the crystal environment. Similar interactions can be assumed for the $S_2$ state. However, they are overcompensated by strong electronic interactions with the $S_4$ state which are reflected in the variations of the CT characters of both states (lower part of Figure 22). In the Franck-Condon region, the $S_2$ state has 95 % Frenkel and 5 % CT character. The opposite ratio is found for the $S_4$ state. Along the way to the CI the CT character of the $S_2$ state increases considerably while that of the $S_4$ state decreases by the same amount. This mixing is allowed because both states belong to the same irreducible representation ($^1A_u$). Due to these interactions the corresponding PESs repel each other leading to a lowering of the $S_2$ state by 0.21 eV while the energy of the $S_4$ state

increases by 0.72 eV. The interactions are also indicated by the fact that the $S_4$ state is more destabilized than the $S_3$ state (0.49 eV). The $S_3$ state can interact with the $S_1$ state (both $^1A_g$). However, the weak variations in their electronic characters indicate that this interaction is small. As a consequence the interactions with the crystal environment lead to a destabilization of both states.

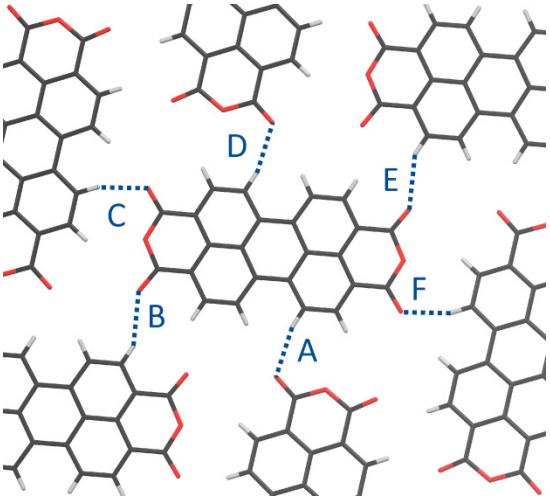


**Figure 23: Illustration of the smallest intermolecular distances in the α-PTCDA crystal structure. More information can be taken from Table 2.**

**Table 2: Smallest intermolecular distances (in Å) are listed for α-PTCDA according to Figure 23 at the Franck-Condon (FC) region, at the CI and at the minimum of the optically dark $S_1$ state.**

| distance | FC region | CI | minimum $S_1$ state |
|---|---|---|---|
| A | 2.39 | 2.24 | 2.22 |
| B | 2.49 | 2.36 | 2.24 |
| C | 2.39 | 2.27 | 2.71 |
| D | 2.39 | 2.50 | 2.62 |
| E | 2.49 | 2.63 | 2.79 |
| F | 2.39 | 2.45 | 2.10 |

The time required for the exciton self-trapping process was estimated by propagating a wave packet on the two-dimensional PES of the $S_2$ state, which was calculated by A. Schubert, from the Franck-Condon region to the CI. His quantum dynamical calculations are performed using grid-based methods. The initial wave function for the nuclear motion, i.e. the vibrational ground state in the $S_0$ state, is determined via a relaxation method.[278] The wave packet after photo excitation is, within the Condon approximation, assumed to be the initial wave function and is placed in the Franck-Condon region of state $S_2$ (see Figure 19). Here, the time-propagation is performed employing the split-operator technique.[258] The Hamiltonian includes the PES $S_2$ spanned by the effective coordinates for the longitudinal and transversal shifts, $q_L$ and $q_T$, as well as the corresponding kinetic energy opera-

tor $T$.[279,280] In the latter the inertias $m_L$ and $m_T$ are regarded separately as effective masses determined by stepwise linearization along the respective coordinate between the calculated relaxed geometries (computed by the mechanically embedded QM/MM approach). As the effective masses do not vary substantially along the axes averaged values are used. The resulting expression for the kinetic operator is:

( 122 ) $T = \frac{-1}{2m_L}\frac{\partial^2}{\partial q_L^2} + \frac{-1}{2m_T}\frac{\partial^2}{\partial q_T^2}$, where $m_{L,T} = \frac{1}{N}\sum_{j_{L,T}=0}^{N-1}\sum_{\alpha} m_\alpha \left|\vec{x}_{\alpha,j_{L,T}+1} - \vec{x}_{\alpha,j_{L,T}}\right|^2$

Here the index $j_L$ and $j_T$ respectively refer to one of the $N$ calculated relaxed crystal geometries, while $j_L + 1$ and $j_T + 1$ indicate the following geometry in the corresponding direction ($q_L$, respectively $q_T$). The coefficient $\alpha$ runs over all atoms of the 250 included PTCDA monomer subunits representing the crystal. The atoms are located at the positions $\vec{x}_{\alpha,j}$ and exhibit the masses $m_\alpha$.

The path taken by the wave packet is indicated as the black arrow in Figure 19. The computations predict that the CI is reached within 400 fs after photo-excitation (corresponds to that instant, when the wave packet crosses the CI for the first time), which is shorter than, or in the same time regime as usual exciton transfer times ($10^3$ – $10^6$ fs).[281] As wave packets are known to change instantaneously between electronic states when reaching a CI,[277] the computations reveal a very efficient trapping mechanism for $\alpha$-PTCDA on an atomistic level.

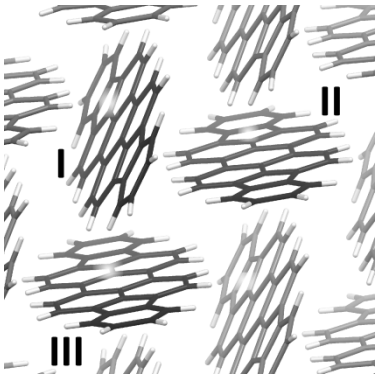


**Figure 24: Geometrical orientations of DIP molecules in the crystal.**

For DIP dimers it can be showen that their electronic structures resemble the ones of PTCDA dimers[273] (see chapter 6) implying that a similar CI also exists in DIP crystals. In the crystal structure of thin films of DIP two symmetrically different dimers (I-II and II-III) coexist (Figure 24). The dimer I-III is equivalent to the I-II one due to the space group of the crystal ($P2_1/a$).

As indicated in Figure 25, for the dimer I-II (II-III) a barrier to the CI of 3.29 eV (1.58 eV) exists in the PES of the $S_2$ state (orange). Therefore, a motion to the CI is strongly hindered and exciton self-

trapping is not expected for both pairs. The barriers result from the strong steric repulsions between the monomers (see Table 3). For both pairs the Franck-Condon region even represents a local minimum so that no reorganization at all is induced by photo-absorption. As a consequence the monomers essentially stick to their positions resulting in efficient exciton transfer.

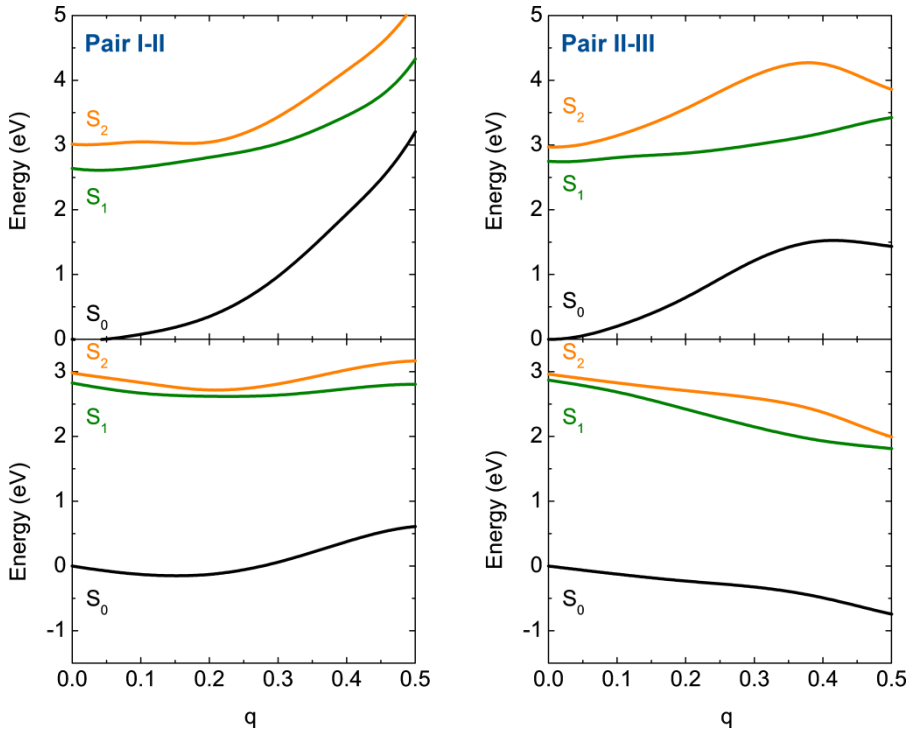


**Figure 25: DIP dimer potential energy curves for the paths from the Franck-Condon region (q = 0.0) of the respective pairs (see Figure 24) towards the CI (q = 1.0). Taking the steric restrictions imposed by the crystal environment into account (upper panels) barriers appear which are not present if steric restrictions are lifted (lower panels).**

In the lower panels of Figure 25 the same PESs are shown for a dimer without any steric restraints. Now, the point of the CI (q = 1) – which is identical for both dimers (I-II and II-III) – is the energetic minimum for all studied states. For the dimer I-II (Figure 25, left) a barrier exists (0.19 eV) on the pathway from the Franck-Condon region (q = 0) to the CI (q = 1), which is apparently not the case for the dimer II-III (Figure 25, right). Here, the final point is 1.46 eV lower in energy than the Franck-Condon region. Therefore, without steric interactions the computations predict an efficient exciton self-trapping for the dimer II-III.

Since without steric restrictions the reaction paths to the CI are barrier-free, efficient exciton self-trapping is predicted for DIP e.g. at grain boundaries or crystallographic defects. To verify this prediction A. K. Topczak and J. Pflaum performed temperature dependent photoluminescence studies on the exciton transport in DIP as well as complementary structural analysis. These experiments verify

the predictions since they reveal that excitons can actually travel across the long-range DIP crystallites without considerable loss, while they are efficiently trapped at their grain boundaries.

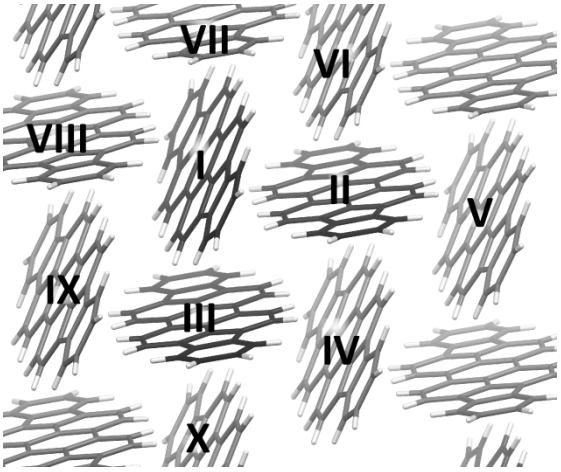


**Figure 26: Numeration scheme of the thin film structure of DIP which is used for the classification of shortest intermolecular distances (see Table 3).**

**Table 3: Shortest intermolecular distances (in Å) for DIP at the Franck-Condon (FC) region and at q = 0.4 for both dimers (see Figure 24). The numeration of the molecules is given in Figure 26.**

| distance | FC region | q=0.4 (I-II) | q=0.4 (II-III) |
|---|---|---|---|
| I-II | 2.86 | 2.22 | 2.80 |
| I-III | 2.86 | 2.78 | 2.90 |
| I-VI | 2.86 | 2.26 | 3.00 |
| I-VII | 2.86 | 2.52 | 2.77 |
| I-VIII | 2.86 | 2.93 | 4.10 |
| I-IX | 2.86 | 2.86 | 3.40 |
| II-III | 2.86 | 2.52 | 3.12 |
| II-IV | 2.86 | 3.08 | 4.70 |
| II-V | 2.86 | 3.12 | 3.05 |
| II-VI | 2.86 | 2.37 | 2.77 |
| III-IV | 2.86 | 2.84 | 2.56 |
| III-IX | 2.86 | 3.26 | 3.29 |
| III-X | 2.86 | 2.92 | 2.67 |

The exciton self-trapping model suggests the following guidelines for the design of materials exhibiting improved exciton transfer properties: Exciton trapping in organic materials is diminished if the packing motifs of the constituting monomers hinder intermolecular motions towards CIs. This is achieved either by crystal structures as for DIP, or by bulky substituents, as already indicated experimentally.[106,167] Alternatively, crystals with relatively large distances between adjacent molecules should exhibit larger $L_D$ values since the CI being responsible for the fast transfer to the trapping state in the case of $\alpha$-PTCDA vanishes for monomer distances exceeding 3.8 Å (see Figure 27).

According to the exciton self-trapping model, efficient trapping results from an initial population of higher lying states in combination with barrierless relaxation pathways to CIs with lower lying ones which feature nearby local minima with a different equilibrium geometry than the ground state. It can be expected that these preconditions are fulfilled for most organic semiconductors with π-stacks in the crystallite structures that give rise to H-aggregates. For such aggregates the higher lying Frenkel states are initially populated after photo-absorption.[114,247] Additionally, as shown below, such aggregates exhibit a high density of electronically excited states which due to topologically quite complex PESs exhibit various CIs. As a consequence, a relaxation path to them without a barrier will always be available if the required rearrangement of the monomers is not restrained by steric restrictions imposed by the environment.

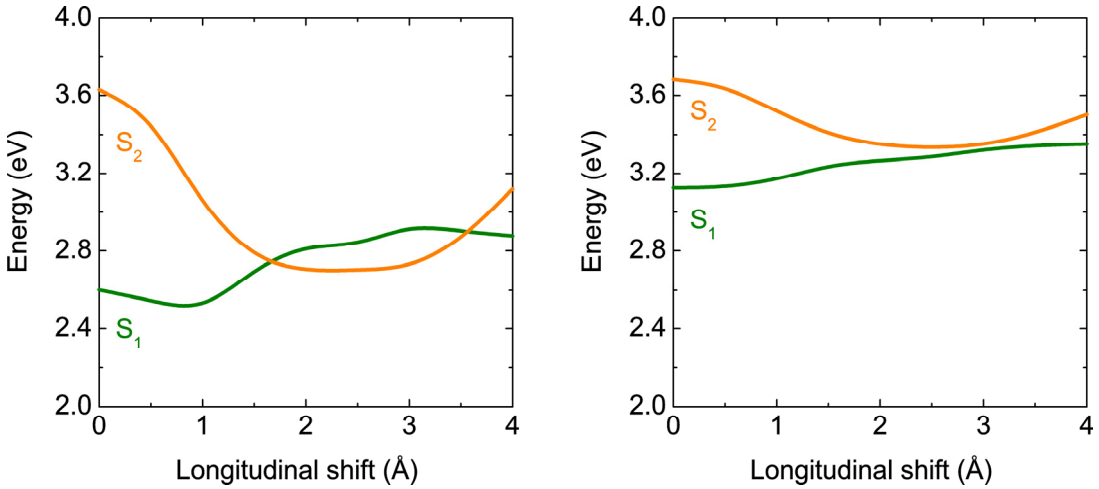


**Figure 27: This figure demonstrates that the region, in which the energetic order of the bright (orange) and dark (green) Frenkel state is inverted, depends on the vertical shift of the monomers in the PTCDA dimer (at 0 Å transversal shift). On the left a PEC of the excitation energies with varied longitudinal shift is shown for a vertical intermolecular distance of 3.35 Å and on the right for an intermolecular distance of 3.75 Å. While for the shorter distance CIs are found at 1.7 Å and 3.6 Å, the features are not found for the larger distance.**

Barrier-less relaxation paths to CIs between the initially populated upper state and lower lying states represent a second required ingredient for the efficiency of the suggested trapping mechanism. The necessary CIs are expected to be present in most aggregates due to the mutual interactions between the close lying electronic states leading to PES which vary strongly as a function of the aggregate orientation. As shown in many investigations Frenkel and CT states couple through electronic coupling elements which are large in comparison to the energy splitting of the underlying diabatic states.[209,272] In recent studies on perylene based compounds it was showed that these couplings are even strong enough to determine the shapes of the PESs.[230,273] Since the strengths of the couplings depend on the mutual orientation of the aggregates the shapes of the PES become quite irregular and several CIs result. Please note that most of these CIs do not correspond to the switch of the

Frenkel states expected for the transition from an H- to a J-aggregate but result from the various interactions between the states in combination with their small energy differences. Barrierless relaxation paths towards one of these CIs will always be available if the surrounding does not strongly hamper the necessary rearrangement of the aggregate monomers. This indicates that also for organic materials CIs are the rule rather than the exception.

# 6. Comparison of the electronic structure in perylene based materials

A part of this chapter was communicated in: V. Settels, W. Liu, J. Pflaum, R. F. Fink, B. Engels, *J. Comput. Chem.* **2012**, *33*, 1544.

**Abstract**

*Aggregates of functionalized polycyclic aromatic molecules like perylene derivatives differ in important opto-electronic properties such as absorption and emission spectra or exciton diffusion lengths. While those differences are well known it is not fully understood if they are caused by variations in the geometrical orientation of the molecules within the aggregates, variations in the electronic structures of the dye aggregates or interplay of both. Since this knowledge is of interest for the development of materials with optimized functionalities, this question is investigated by comparing the electronic structures of dimer systems of representative perylene based chromophores. The study comprises dimers of perylene, 3,4,9,10-perylene tetracarboxylic bisimide (PBI), 3,4,9,10-perylene tetracarboxylic dianhydride (PTCDA) and diindeno perylene (DIP). Potential energy curves (PECs) and characters of those electronic states are investigated which determine the optoelectronic properties. The computations employ the spin-component-scaled approximate coupled-cluster second order (SCS-CC2) method which describes electronic states of predominately Frenkel or neutral excited (NE) and charge transfer (CT) character equally well. The results show that the characters of the excited states change significantly with the intermolecular orientation and often represent significant mixtures of NE and CT characters. However, PECs and electronic structures of the investigated perylene derivatives are almost independent of the substitution patterns of the perylene core indicating that the observed differences in the optoelectronic properties mainly result from the geometrical structure of the dye aggregate. It also hints at the fact that optical properties can be computed from less-substituted model compounds if a proper aggregate geometry is chosen.*

Till now trapping mechanisms were presented, which are valid for PBI aggregates in solution and crystalline $\alpha$-PTCDA. It remains unclear whether trapping is an effect based on intrinsic properties of the single dye or if a more general understanding could be gained. A direct comparison of both studied cases is difficult till they differ in the specific perylene based dye and the geometric orientation of the molecular within the aggregate. Since this knowledge is of interest for the development of mate-

rials with optimized functionalities for optoelectronic devices, the electronic structures of dimer systems of representative perylene based chromophores in similar geometric arrangements are compared. The study presented in this chapter comprises dimers of perylene, PBI, PTCDA and DIP. Potential energy curves (PECs) and characters of those electronic states which determine the optoelectronic properties are investigated. The computations employ the spin-component-scaled approximate coupled-cluster second order (SCS-CC2) method which describes electronic states of predominately Frenkel excited (NE), which are also called Frenkel excited, and charge transfer (CT) character equally well. It will be shown that the characters of the excited states change significantly with the intermolecular orientation and often represent significant mixtures of Frenkel and CT characters. However, PECs and electronic structures of the investigated perylene derivatives are almost independent of the substitution patterns of the perylene core indicating that the observed differences in the optoelectronic properties mainly result from the geometrical structure of the dye aggregate.

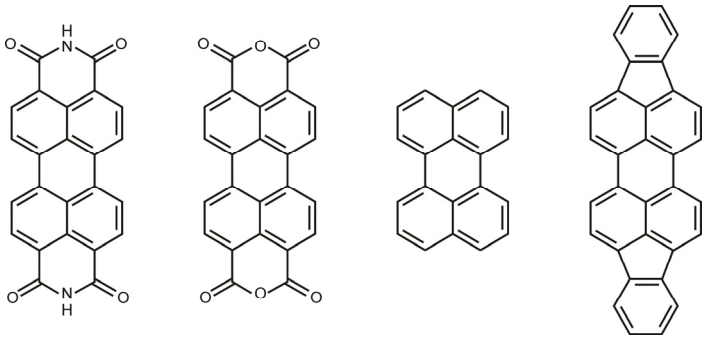

**Figure 28: Perylene based molecules considered in this work. From left to right: 3,4,9,10-perylene tetracarboxylic bisimide (PBI), 3,4,9,10-perylene tetracarboxylic dianhydride (PTCDA), perylene and diindeno perylene (DIP).**

The strong influence of the relative orientation of monomers in the respective crystal on the absorption spectra of PBI derivatives has been shown by several investigations.[74,211,272,276,282,283] Klebe et al. found for differently substituted PBI derivates that in the crystalline state the absorption maxima are spread over a wide spectral range, while in the dispersed phase, where interaction between the monomers can be neglected, all molecules possess essentially identical absorption spectra.[74] Similar effects were also shown by other investigations.[168,219,262,284-286] The influence of the crystal structure was also underlined by Engel et al.[287] They reported nearly identical absorption and flourescence spectra for PTCDA and PBI monomers in solutions, but different spectra for the corresponding aggregates. Furthermore, their computations revealed only small differences in the vertical excitation energies of the PTCDA and PBI monomer which was also suggested by other studies.[272,288]

Variations in the electronic structure of the involved dyes were also underlined by several studies.[75,211,289-295] For example Gisslen and Scholz emphasize such differences between the electronic

structures of PTCDA and DIP on one side and PBI compounds on the other.[272] Recent computations on PBI dimers also predict that the strong interaction between both types of diabatic states lead to adiabatic states with strongly mixed characters.[230] However, in contrast to the previous studies, the computed Frenkel states were computed to be lower in energy than the related CT states. The model introduced in chapter 5.1 of this thesis, which explains femtosecond time-resolved experiments for PBI aggregates in solution as well as the corresponding absorption and emission spectra, also underlines strong interactions between both types of states.[168,255]

In this chapter differences are investigated in the electronic structures of perylene based dyes. For this the ground state PES and potential energy curves of several low lying electronic states of two prototypes of dimer aggregates of PTCDA, PBI, perylene, DIP are compared (see Figure 10 in chapter 4). The first one is a rotated π-stacked dimer in combination with torsional motion along φ (definition see Figure 10). The torsional motion was selected since it was found to be essential for the explanation of the emission spectra of PBI aggregates (see chapter 5.1).[168,255] As second model aggregate, shifted π-stacked dimers are investigated since in most crystal structures the molecular entities within the unit cell are shifted with respect to each other.[74] For this prototype a shift along the longitudinal axis is investigated (see Figure 10). On the other hand, this is a generalization of the trapping mechanism in crystals introduced in chapter 5.2.[296] The basic feature of this mechanism is a seam of conical intersections. If this seam exists in other perylene dyes besides PTCDA as well, an interchange of the optically bright and dark state should appear for longitudinal shifted dimers at certain shifts.

The molecules under study represent a well-chosen set of model compounds as they define important prototypes for organic dyes, possess considerably different exciton diffusion lengths and have proven their potential in organic electronic applications. The described approach by *ab initio* computations of aggregates allows for a comparison of the electronic structure for different geometrical arrangements. Molecular dimers are used to model the dye aggregates since computations for even larger aggregates with the required accuracy in energy of approximately 0.1-0.2 eV are very demanding. Additionally dimers are important sub-units of aggregates as after excitation, the related energy is localized very fast on these sub-units.[147]

## 6.1 Differences in global minima of the electronic ground state

First, shapes of the PECs of ground and excited states as a function of the twist motion is studied to elucidate differences between the electronic structures of perylene derivatives. Some information about the differences in the ground state equilibrium structures is needed to identify possible connections to aggregate and crystal structures. PBI, PTCDA and DIP represent derivatives of perylene with different substitution patterns (Figure 28).

The different substituents modify the electrostatic potentials (Figure 29) which may influence the position of the global minimum structure of the dimers. In recent studies on PBI derivatives, Fink et al.[168] and Zhao et al.[219] have shown that the ground state PES of the PBI dimer possesses at least seven minima in an energy range of about 0.5 eV. The global minimum corresponds to a *twisted* orientation with R = 3.31 Å, X = 0.00 Å, Y = 0.00 Å, and $\varphi$ = 31.5°. Here, R symbolizes a horizontal, X a longitudinal and Y a transversal shift (see Figure 10). The next higher lying minimum has a *shifted* orientation R = 3.26 Å, X = 0.93 Å, Y = 1.41 Å, and $\varphi$ = 0.1°. It is only 0.13 eV higher in energy than the global minimum. The results of the present computations are summarized in Table 4. The slight deviations within the computed geometries and relative energies to the former published ones are caused by differences in the empirical dispersion correction.[219] Beside twisted and shifted structures, Table 4 also lists some additional minima. The relative energies are given with respect to the geometry optimized staggered conformation of the dye dimers (R = 3.56 Å, X = Y = 0 Å, $\varphi$ = 0°).

The related structures also represent minima on the PESs of PTCDA and DIP, but Table 4 shows that the relative energies are influenced by the substitution pattern as expected. The approach predicts an energy difference of about 0.14 eV between the energetically lowest twisted and the shifted orientations for PBI. For PTCDA the lowest shifted (R = 3.31 Å, X = 3.46 Å, Y = 1.13 Å, $\varphi$ = 0°) and the twisted (R = 3.28 Å, X = 1.29 Å, Y = 0.60 Å, $\varphi$ = 43.8°) orientations are more or less isoenergetic. For this dye dimer the ten lowest structures are within an energy range of 0.1 eV.

The differences between the global minima of PBI and PTCDA dimer can be explained by the electrostatic potentials of these dyes as mentioned above (Figure 29). Both molecules show significant negative charges located at the carbonyl oxygen atoms, but the electrostatic potentials differ in the region between the carbonyl groups. While the imide group gives rise to a positive region at the hydrogen in PBI, the electrostatic potential around the corresponding anhydride oxygen in PTCDA is negatively charged. Another difference appears in the center of the six-membered ring formed from the anhydride or the imide group. This region is positively charged in both molecules but for PTCDA the charge is considerably more pronounced than for PBI. Similarly, the perylene core of PTCDA is more positively charged than its PBI counterpart.

**Table 4: Energies and key structural parameters are given for the four lowest minima of the PBI, PTCDA and DIP dimers in the electronic ground states. The energies are given with respect to a geometry optimized staggered conformation (PBI, PTCDA, DIP: R = 3.56 Å, X = Y = 0 Å, φ = 0°). Values for R, X and Y correspond to the middle of the central benzene rings of the two monomers. The energies are given in eV, the distances in Ångströms, and the angles in degrees.**

| | ΔE | R | X | Y | φ | structure |
|---|---|---|---|---|---|---|
| PBI | -0.572 | 3.31 | 0.00 | 0.00 | 31.5 | twisted |
| | -0.437 | 3.26 | 0.93 | 1.41 | 0.1 | shifted |
| | -0.366 | 3.28 | 3.43 | 1.20 | 0.1 | |
| | -0.362 | 3.26 | 0.66 | 1.19 | 60.9 | |
| PTCDA | -0.522 | 3.28 | 1.29 | 0.60 | 43.8 | twisted |
| | -0.518 | 3.35 | 1.80 | 0.60 | 33.4 | |
| | -0.515 | 3.31 | 3.46 | 1.13 | 0.0 | shifted |
| | -0.498 | 3.36 | 3.14 | 0.34 | 14.0 | |
| DIP | -0.478 | 3.27 | 0.00 | 0.02 | 34.7 | twisted |
| | -0.434 | 3.24 | 0.82 | 1.38 | 0.1 | shifted |
| | -0.375 | 3.29 | 0.51 | 1.01 | 56.4 | |
| | -0.351 | 3.34 | 2.07 | 0.52 | 26.0 | |

For the global minimum of PBI (twisted structure) the negatively charged cloud around the carboxyl oxygen of one monomer is closely spaced to the positively charged cloud around the imide group of the other monomer. In PTCDA the largest positive charge is located in the center of the anhydride ring (see Figure 29Figure 29). Thus, an additional shift along the X and Y direction is necessary to locate the negative charge cloud at the carbonyl oxygen next to the positive charge.

The analysis shows that the differences between the electrostatic potentials of PBI and PTCDA influence the equilibrium geometries of the ground state. In terms of energy the differences are quite small but since the ground state PES is very flat, the geometrical parameters change significantly. Due to the flatness of the PESs, the crystal structures of these perylene dyes are considerably influenced by packing effects. As already mentioned in a recent work[219] this explains the strong variation in the crystal structures of PBI derivatives. The crystal structure of α-PTCDA[297] (R = 3.36 Å, X = 1.14 Å, Y = 1.05 Å, φ = 0.0°) can be assigned to a local minimum of the dimer (R = 3.27 Å, X = 1.12 Å, Y = 1.29 Å, φ = 0.1°), which is only 0.09 eV higher in energy than the global one.

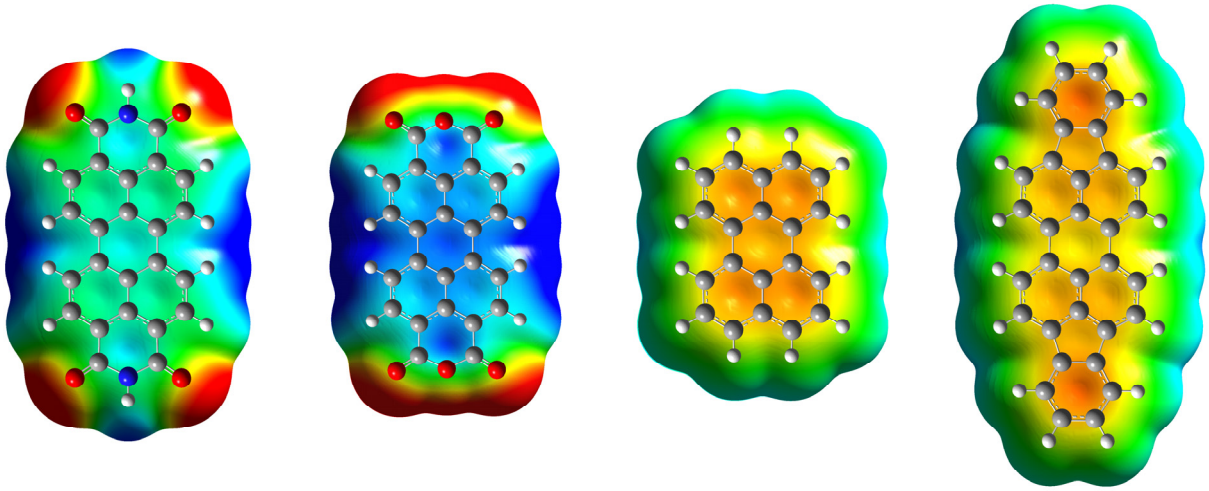

**Figure 29: From left to right: Electrostatic potentials of PBI, PTCDA, perylene and DIP plotted at the surface of an isovalue of 0.001 a.u. of the BLYP/6-311G** total electron density using Gaussian03.[220] The color code ranges from -0.025 a.u. (blue) to 0.025 a.u. (red).**

The global minimum of the DIP dimer has a twisted structure (R = 3.27 Å, X = 0.0 Å, Y = 0.02 Å, φ = 34.7°) with similar parameters as PBI. It is about 0.04 eV lower in energy than the shifted structure (R = 3.24 Å, X = 0.82 Å, Y = 1.38 Å, φ = 0.1°). The stabilization of the twisted structure can also be explained by electrostatic interactions of the molecules. The largest negative charge can be found above the center of the indeno benzene ring. In the twisted global minimum structure (φ = 34.7°) the positively charged hydrogen atoms of the indeno group are located close to the largest negative charge. A similar arrangement is found in the shifted structure. In this arrangement the electrostatic attraction is smaller than in the twisted structure, destabilizing this structure to be 0.04 eV higher in energy despite a stronger dispersive stabilization of 0.05 eV. For DIP a crystal structure with T-stacked dimers was found.[81] A geometry optimized symmetric T-stacked dimer has a lower energy in DIP (0.174 eV) than in PBI (0.246 eV) or PTCDA (0.257 eV). As before, the energies are given with respect to a staggered dimer arrangement. This finding could be one reason for the differences in the crystal structure of DIP compared to the other two dyes.

## 6.2 Energies of the first excited states as a function of a torsion motion

The PECs of the ground and the six lowest lying electronically excited singlet states of PTCDA, PBI, perylene and DIP as a function of the coordinate φ are given in Figure 30. The obvious similarities in the PECs indicate strong resemblance in the electronic structures which is also visible in the shapes of the involved orbitals (Figure 31).

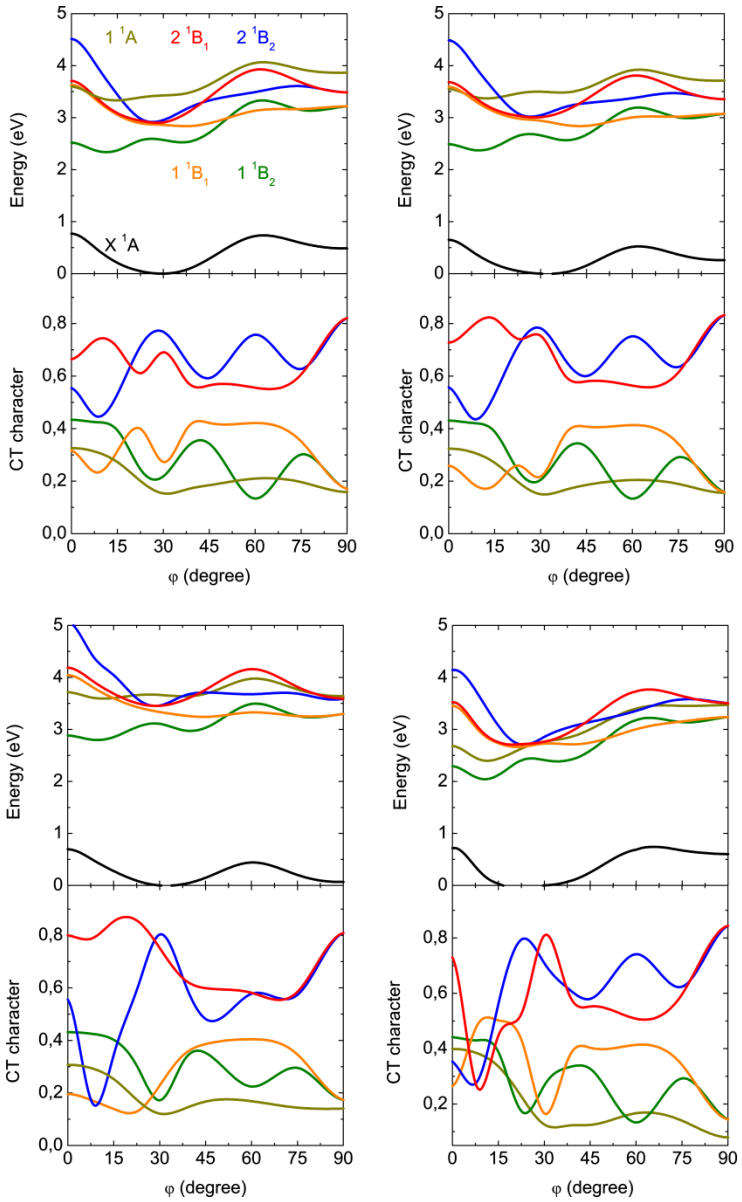


**Figure 30: Comparison of the potential energy curves computed for the torsional motion. The upper plot shows the potential energy curves (PECs) of the ground and the five low lying excited singlet states of the dimers as a function of the torsional coordinate φ. PECs of states with mainly Frenkel (CT) character are indicated by solid (dashed-dotted) lines. The lower plot shows the amount of CT character in the respective wave functions. Upper row: PBI and PTCDA. Lower row: Perylene and DIP.**

The ground state PEC of PTCDA shows maxima at torsion angles of 0° and about 62°. Minima are found for 32° and 90°. The maximum at 0° (62°) lies energetically 0.65 eV (0.53 eV) above the global minimum which is found at 32°. The ground state PEC of PBI is almost identical to that of PTCDA with maxima at 0° and 63°, which lie 0.76 eV and 0.74 eV, respectively, above the minimum at 29°. The similarity in the position of the global minima at about 30° is owing to the similarities of the electrostatic potentials of these molecules.

However, the interactions differ slightly and result in changes of the relative energies. The difference between the depth of the global minimum in PTCDA and PBI at $\varphi \approx 30°$ can be qualitatively explained by the electrostatic interactions of the charge distributions shown in Figure 29. For the PBI structure there is a significant attractive interaction between the positively charged hydrogen atoms of one monomer and the carbonyl groups of the other one. This attraction seems to be stronger than the interaction between the positive charge in the center of the anhydride group and the negative charges of the anhydride groups of the other monomer.

As shown in Figure 30 (upper row), the shapes of the PECs of the six energetically lowest lying excited singlet states of PTCDA and PBI and the corresponding relative energies are almost identical. The vertical excitation energies into the bright $1^1B_1$ state at the twisted minima of the ground states of PTCDA and PBI differ only by 0.06 eV (2.92 eV and 2.86 eV, respectively). The similarities in vertical excitation energies hold for the whole PEC: The vertical excitation energies of PTCDA ($1^1B_1 \leftarrow X^1A_1$) are shifted up by 0.081±0.003 eV with respect to the corresponding vertical excitation energies in PBI. Therefore, the shapes of the PEC's of the excited states mirror the differences found within the PEC's of the ground states.

Similar trends are found for all other computed excited states. Let us take the $1^1B_2$ state as another example, which represents the lowest lying electronic state for the region around the minimum of the ground state ($\varphi \approx 30°$). The PECs of PTCDA and PBI are quite flat between 0° and 45°. In this region two shallow minima are predicted for PTCDA (10°, 39°) and for PBI (11°, 36°). For both compounds they are separated by a small barrier at about 26°. The energies of the global minima of the $1^1B_2$ state at around 10° with respect to $\varphi = 0°$ are -0.13 eV (PTCDA) and -0.19 eV (PBI). The relative energies of the barriers between both minima are 0.20 eV for PTCDA while 0.08 eV is predicted for PBI. The energies of the maxima at about 60° relative to $\varphi$=0° are 0.71 eV (PTCDA) and 0.82 eV (PBI). The relative energies for the higher minima at about 78° are 0.49 eV and 0.61 eV.

The similarities in the shapes of the corresponding PECs might be interpreted as a result of similar electronic structures of the PBI and PTCDA dimers. However, a recent study showed that similar shapes of the PECs of the energetically related excited adiabatic states do not necessary imply that electronic states with similar PECs also agree in their characters.[230] Thus, the similarities of the PTCDA

and PBI potential energy curves may arise although diabatic CT and Frenkel states are energetically interchanged. However, Figure 30 (upper row), which compares the character of the excited adiabatic singlet states of PBI and PTCDA, confirms that this is not the case. Let us take the $1^1B_2$ state as an example. For the PBI dimer it possesses a mixed character (42 % CT vs. 58 % Frenkel) for $\varphi = 0°$, while it is predominantly Frenkel (20 % CT vs. 80 % Frenkel) for $\varphi \approx 30°$. For $\varphi > 30°$ it remains predominantly Frenkel but the amount of CT character rises again to about 32 % at 45° and 28% at 80°. For PTCDA the variations in the character of the $1^1B_2$ state strongly resemble the behavior found for PBI. The similarity between PBI and PTCDA is also reflected in the characters of the configurations which dominate the characters of the excited states (see Table 5 and Table 6).

For the optically bright $1^1B_1$ state the characters of the PBI and PTCDA dimers are also very much alike. This state is predominantly Frenkel between $0° < \varphi < 40°$. For $40° < \varphi < 75°$ the CT character increases to about 40%. It decreases again for $\varphi > 75°$. The variations found for the $2^1B_1$ and the $2^1B_2$ states which represent the CT dominated counterparts to the $1^1B_1$ and $1^1B_2$ states, respectively, are also very similar. The same holds for the $1^1A$ and $1^1B_3$ states. All these similarities strongly support the conception that the PBI and the PTCDA dimer possess indeed very similar electronic structures. Hence, the discussions about the nature and the size of the interactions which was presented recently for the PBI dimer can be transferred to the PTCDA dimer. A more detailed discussion about the character mixing can be found in a recent paper.[230]

The similarity between the electronic structures of PTCDA and PBI may result since they are dominated by the perylene core while the influence of the substitution is less important. To investigate this possibility the corresponding PECs of the perylene dimer were computed. They are summarized in Figure 30 (lower row left). The similarities between the PECs of the perylene dimer on one hand and the corresponding ones computed for the PBI or the PTCDA dimers on the other hand are obvious. As found for PBI and PTCDA the PEC of the ground state of the perylene dimer possesses two minima at torsion angles of about 32° and 90° as well as two maxima at 0° and 61°. But some quantitative differences are predicted. Relative to the global minimum at about 32° the maximum for perylene at 61° is lower in energy than the corresponding ones for PBI or PTCDA (PBI: 0.76 eV and 0.74 eV; PTCDA: 0.65 eV and 0.53 eV; perylene: 0.70 eV and 0.45 eV). However, while the lower maximum in PTCDA results since the minimum at $\varphi \approx 30°$ is destabilized due to a repulsive interaction between the substituent, the lower maximum for perylene results from the much weaker electrostatic interaction. The negative charge is centered in the middle of the aromatic rings of the naphthalene units, while the hydrogen atoms are positively charged (see Figure 29). At $\varphi = 32°$ the negative charge at the naphthalene aromatic rings is located at the middle of the naphthalene and in close proximity to the hydrogen atoms. At the maximum of $\varphi = 61°$ the negatively charged aromatic rings

of the two monomers are located directly above each other. At 90° the aromatic rings are again spaced next to hydrogen atoms and this structure presents a second minimum on the ground state PEC. In contrast to the other dyes this second minimum is almost isoenergetic to the global one at 32° (ΔE = 0.07 eV). The global minimum structure is stabilized by 0.06 eV with respect to the structure at 90° by dispersion interactions. Therefore electrostatics seems to influence the two minimum structures almost equally in contrast to the other dyes.

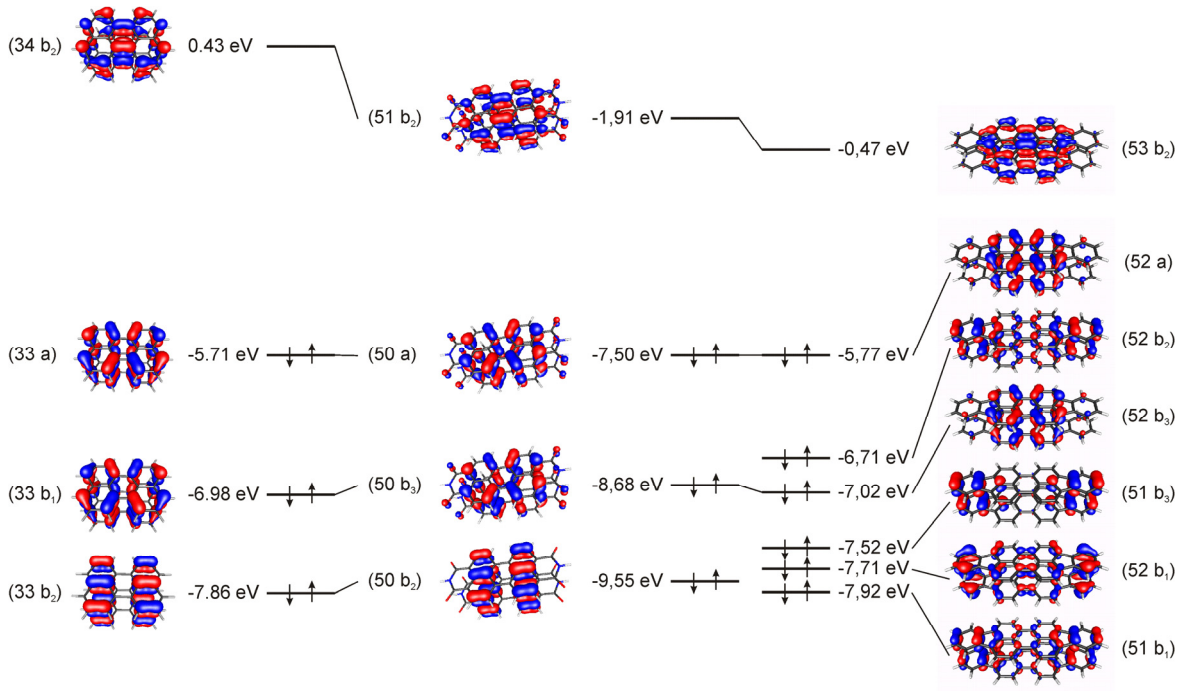


**Figure 31: Orbitals of dimers of perylene (left), PBI (middle) and DIP (right) at a torsion angle of 0°.**

While energetic positions and shapes of the PECs of the PBI and the PTCDA dimer nearly coincide, the perylene counterparts differ to some extent. Most obviously, the vertical excitation energy to the bright $1^1B_1$ state at $\varphi = 30°$ increases from 2.86 eV (PBI dimer) and 2.94 eV (PTCDA dimer) to 3.33 eV for the perylene dimer. This indicates that the imide and anhydride groups induce a red shift of the absorption band. These red shifts are proportional to the shifts in the HOMO to LUMO+1 gap of the monomers, which increases from 6.77 eV (PBI) and 6.90 eV (PTCDA) to 7.44 eV for perylene. For all systems the proportional factor is around 0.7 ($E_{ex}(1^1B_1) \sim 0.7 \cdot [E(\text{LUMO+1}) - E(\text{HOMO})]$). The configuration which is obtained from the ground state configuration by a HOMO $\rightarrow$ LUMO+1 transition represents the main configuration of the $1^1B_1$ state. Its contribution to the wave function is 0.8 while a value of about 0.15 is computed for the configuration connected with the HOMO-1 to LUMO transition (see Table 5). All these orbitals in perylene agree nicely with the corresponding PBI orbitals (see Figure 31). The difference in orbital energies for the transition with the minor contribution is propor-

tional by the same factor to the excitation energy. This explains why the approximation of excitation energies by orbital energy differences is well suited to describe trends within the absorption spectra of this class of organic dyes.

**Table 5: Dominating single excited configurations of selected singlet transitions for dimers of perylene, PBI, PTCDA and DIP at a rotation angle of 30° (H: HOMO, L: LUMO). The contribution of a given configuration to the wave function (square of its amplitude) is given for all configurations where this value is larger than 0.1.**

| transition | perylene | PBI | PTCDA | DIP |
|---|---|---|---|---|
| $1^1A$ | H → L+3 (0.23) | H-3 → L+1 (0.39) | H-3 → L+1 (0.39) | H-2 → L+1 (0.56) |
| | H-1 → L+2 (0.22) | H-2 → L (0.22) | H-2 → L (0.21) | H-3 → L (0.39) |
| | H-3 → L+1 (0.18) | | H-7 → L (0.10) | |
| | H-2 → L (0.12) | | | |
| $1^1B_1$ | H → L+1 (0.81) | H → L+1 (0.87) | H → L+1 (0.80) | H → L+1 (0.69) |
| | H-1 → L (0.14) | H-1 → L (0.09) | H-1 → L (0.16) | H-1 → L (0.25) |
| $2^1B_1$ | H-1 → L (0.83) | H-1 → L (0.90) | H-1 → L (0.83) | H-1 → L (0.70) |
| | H → L+1 (0.15) | | H → L+1 (0.15) | H → L+1 (0.28) |
| $1^1B_2$ | H → L (0.72) | H → L (0.81) | H → L (0.79) | H → L (0.87) |
| | H-1 → L+1 (0.26) | H-1 → L+1 (0.17) | H-1 → L+1 (0.19) | H-1 → L+1 (0.10) |
| $2^1B_2$ | H-1 → L+1 (0.72) | H-1 → L+1 (0.82) | H-1 → L+1 (0.80) | H-1 → L+1 (0.87) |
| | H → L (0.26) | H → L (0.16) | H → L (0.19) | H → L (0.11) |
| $1^1B_3$ | H → L+2 (0.28) | H-3 → L (0.39) | H-3 → L (0.39) | H-2 → L (0.74) |
| | H-1 → L+3 (0.20) | H-2 → L+1 (0.17) | H-2 → L+1 (0.17) | H-3 → L+1 (0.22) |
| | H-3 → L (0.16) | H → L+6 (0.10) | H → L+6 (0.12) | |
| | H-2 → L+1 (0.11) | | | |

The energy spacing between the excited states represents another difference between the analyzed perylene derivatives. At $\varphi = 30°$ the energy difference between the predominantly Frenkel $1^1B_1$ state and its CT dominated counterpart $2^1B_1$ increases from 0.05 eV (PBI dimer) and 0.07 eV (PTCDA dimer) to 0.12 eV for the perylene dimer. Actually, the energy separation between these states is slightly increased along the whole PEC of perylene if compared with PBI and PTCDA. For the first two $^1B_2$ states the change of the energetic separation is less obvious (PBI: 0.38 eV; PTCDA: 0.39 eV; perylene: 0.35 eV), but again the excitation energies of both states are proportional to the energy of the fundamental orbital transitions (HOMO to LUMO and HOMO-1 to LUMO+1, see Figure 31). For small rotation angles ($\varphi < 40°$) the states of perylene seem to be less mixed than their PTCDA or PBI counterparts. At a parallel alignment of both monomers ($\varphi = 0°$) the $1^1B_1$ state of perylene possesses 80 % Frenkel character while the $2^1B_1$ state exhibits 80 % CT character. The corresponding states in PBI ($1^1B_1$: 68 % Frenkel; $2^1B_1$ 66 % CT) and PTCDA ($1^1B_1$: 74 % Frenkel; $2^1B_1$ 72 % CT) are stronger mixed. However, although the $1^1B_1$ state of the perylene dimer possesses less CT character than its counterpart in PBI or PTCDA, the computed oscillator strength is in average 0.25±0.09 smaller than

the values predicted for the PBI dimer (see Figure 32). This underlines the strong influence of the substituents on this property. It was already noticed that the excited states of the perylene dimer are up-shifted in comparison to their PBI and PTCDA counterparts. For the case of the $1^1$A state this is less obvious and for $\varphi > 50°$ the $1^1$A state of the perylene dimer even becomes red shifted compared to the corresponding state in the PBI dimer. These differences result from considerable changes of the contributions of the leading orbital configurations to the wave functions. At 0° the state $1^1$A of PBI is dominated by the two single excitations HOMO-2 → LUMO (orbital energy difference $\Delta\varepsilon$ = 7.5 eV) and HOMO → LUMO+4 ($\Delta\varepsilon$ = 8.2 eV) which contribute to the wave function with weights of 0.72 and 0.17, respectively. For perylene the corresponding squares of the intermediate normalized amplitudes are 0.27 (HOMO-2 → LUMO; $\Delta\varepsilon$ = 8.3 eV) and 0.60 (HOMO → LUMO+2; $\Delta\varepsilon$ = 7.8 eV). However, the exceptional behavior of the $1^1$A state is of minor importance since its transition dipole moment vanishes and its energy position renders him less favorable for any possible quenching processes.

The differences between the PTCDA, PBI, and perylene dimers discussed above are rather small suggesting that the characters and properties of the low lying electronic states are mostly determined by the perylene core while substituent effects seem to be less important. This can be traced back to the fact that all orbitals which are involved in the considered excitations in PBI or PTCDA are mostly located at the perylene core (Figure 31). In their study Gisslen and Scholz[272] came to the conclusion that DIP is more similar to PTCDA than to PBI derivatives. However, as shown recently DIP has a considerably larger exciton diffusion length than PTCDA or PBI derivatives (DIP: ~100 nm; PTCDA: 22 nm).[76,77] Information about the electronic structure of the DIP dimer can be taken from Figure 30 (lower row) which shows the PECs of the ground and the six lowest lying excited states as a function of the torsion motion. Overall, the PEC of the ground state of DIP resembles the corresponding PECs of the other perylene based dyes, but some differences exist. In comparison to the other dimers the global minimum of the ground state PEC is shifted to a smaller angle ($\varphi$ = 21°) and the valley around the minimum is considerably broader than for the other dimers. Between $16° < \varphi < 33°$ the energy increases only by 0.05 eV. Furthermore the barrier height computed for $\varphi$ = 90° is larger than the value computed for the PBI dimer (0.60 eV vs. 0.48 eV). This difference is caused by the additional stabilization of the DIP dimer at small angles due to additional dispersion interactions of the indeno groups. Related interactions are missing in the other dyes considered in this work. The dispersion correction of the BLYP-D approach estimates the difference in the dispersion interaction for $\varphi$ = 0° and $\varphi$ = 90° to 0.97 eV for the DIP dimer which is almost twice as large as for the PBI (0.52 eV) and PTCDA dimers (0.45 eV). For smaller rotation angles the energy rises again due to electrostatic inter-

actions. The maximum of the ground state energy at a torsion angle of 66° closely resembles the PBI dimer situation.

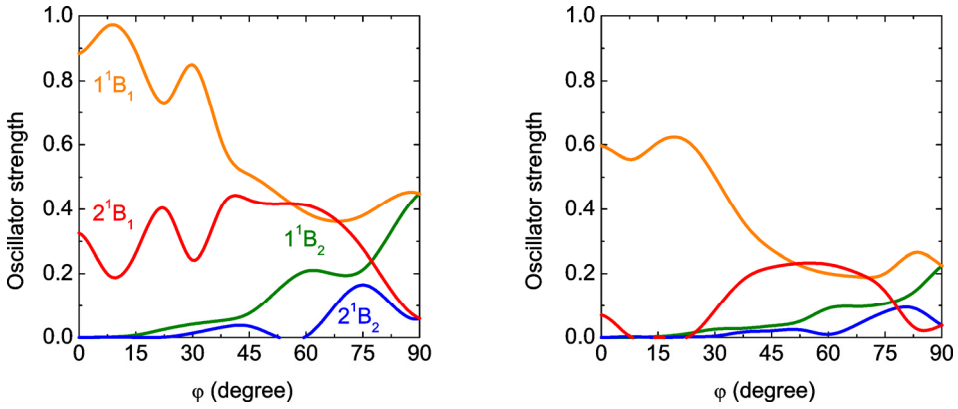


**Figure 32: Comparison of the oscillator strength of PBI (left) and perylene (right). States with mainly Frenkel (CT) character are colored as orange and green (red and blue).**

The vertical excitation energy is 2.69 eV to the optically bright 1 $^1B_1$ state for φ = 21°. It is red shifted compared to PTCDA (2.93 eV) and PBI (2.84 eV). A similar trend is found for the bright excitation in the dye monomers as well (DIP: 2.74 eV, PTCDA: 2.92 eV, PBI: 2.85 eV). The red shift results from the +M effect of the auxochrome indeno group in combination with the missing -M effect of the antiauxochrome carbonyl group.[283] Although red-shifted by about 0.3 eV the shapes of the PECs of the excited $^1B_1$ and $^1B_2$ states are very similar to the corresponding ones of PTCDA, PBI or perylene. The character analysis yields comparable results as well.

One obvious difference is found for the characters of both $^1B_1$ states for 10° < φ < 20°. According to the computed characters in this region the adiabatic states of the DIP dimer represent complete mixings between the diabatic Frenkel and CT states. Please note that the sum of CT ratio does not add up to 1 at this point since also mixings with even higher lying states occur. For the PBI and the PTCDA dimer the $^1B_1$ states are also very close in energy in this region but the mixings are considerably smaller. The small spacing of these adiabatic states indicates that for PBI and PTCDA the underlying diabatic states are close in energy but their interaction through the electronic Hamilton operator is small. For DIP the interaction seems to be small as well, but since the underlying diabatic states are even closer in energy the small interaction is already sufficient to lead to a complete mixing. For φ < 10° the energy splitting between both computed adiabatic states $1^1B_1$ and $2^1B_1$ of the DIP dimer increases accompanied by a change into almost pure Frenkel and CT characters. This indicates that the energy splitting of the underlying diabatic states increases while the interaction remains small. Moreover at φ ~ 10° the formal CT state mixes with a higher lying state as well. Summarizing, the qualitative differences between DIP on one hand and PTCDA as well as PBI on the other hand are

small, but since both $^1B_1$ states are so close in energy in this region the resulting influence on the character of the states is strong. For $\varphi > 40°$ the $^1B_1$ states of the DIP dimer show the same behavior as those of the PTCDA and the PBI dimer. Both $^1B_2$ states behave very similar as their counterparts in the PTCDA and the PBI dimer.

**Table 6: Dominating single excited configurations of selected singlet transitions for perylene, PBI, PTCDA and DIP dimers at a rotation angle of 0° (H: HOMO, L: LUMO). The contribution of the configurations to the wave function is depicted in brackets if it is larger than 0.1.**

| transition | perylene | PBI | PTCDA | DIP |
|---|---|---|---|---|
| $1^1A$ | H → L+2 (0.60) | H-2 → L (0.72) | H-2 → L (0.71) | H-1 → L (0.95) |
| | H-2 → L (0.27) | H → L+4 (0.17) | H → L+4 (0.18) | |
| $1^1B_1$ | H-1 → L (0.77) | H-1 → L (0.91) | H-1 → L (0.86) | H-2 → L (0.84) |
| | H → L+1 (0.18) | | H → L+1 (0.11) | H → L+1 (0.10) |
| $2^1B_1$ | H → L+1 (0.79) | H → L+1 (0.93) | H → L+1 (0.88) | H → L+1 (0.86) |
| | H-1 → L (0.20) | | H-1 → L (0.11) | H-2 → L (0.12) |
| $1^1B_2$ | H → L (0.98) | H → L (0.98) | H → L (0.98) | H → L (0.98) |
| $2^1B_2$ | H-3 → L+1 (0.96) | H-1 → L+1 (0.97) | H-1 → L+1 (0.98) | H-1 → L+3 (0.39) |
| | | | | H-8 → L (0.32) |
| $1^1B_3$ | H-4 → L (0.79) | H-4 → L (0.52) | H-4 → L (0.63) | H-4 → L (0.83) |
| | H → L+4 (0.15) | H → L+3 (0.45) | H → L+3 (0.33) | |

While the differences for $^1B_1$ and $^1B_2$ are small, larger variations can be found for the PECs of the excited $1^1A$ and $1^1B_3$ states. At $\varphi = 0°$ they differ strongly from the corresponding states in the other perylene based dyes. The $1^1B_3$ state which is considerably higher in energy for PTCDA (0.56 eV) and PBI (0.55 eV) lies only slightly above the $1^1B_1$ state for DIP (0.18 eV). The $1^1A$ state even crosses the $1^1B_1$ state at $\varphi = 24°$. Although considerably red shifted, the shapes of both states resemble the ones of the corresponding states in PTCDA or PBI. Also their natures in terms of CT or Frenkel characters behave very similar (Figure 30).

To rationalize the strong shift found for $1^1A$ and $1^1B_3$ states, Table 6 analyses the characters of the states of the PBI and the DIP dimer with the help of these configurations which dominate the wave functions of the excited states. The configurations are characterized by the excitations which transfers the closed shell ground state configuration into the respective configurations. Additionally, their weights in the corresponding wave functions are given. Figure 31 correlates the involved canonical orbitals of the PBI and the DIP dimer. For clarity Table 6 and Figure 31 depict the situation for $\varphi = 0°$. For larger $\varphi$ values the characters of the MOs remain but the picture becomes more complex.

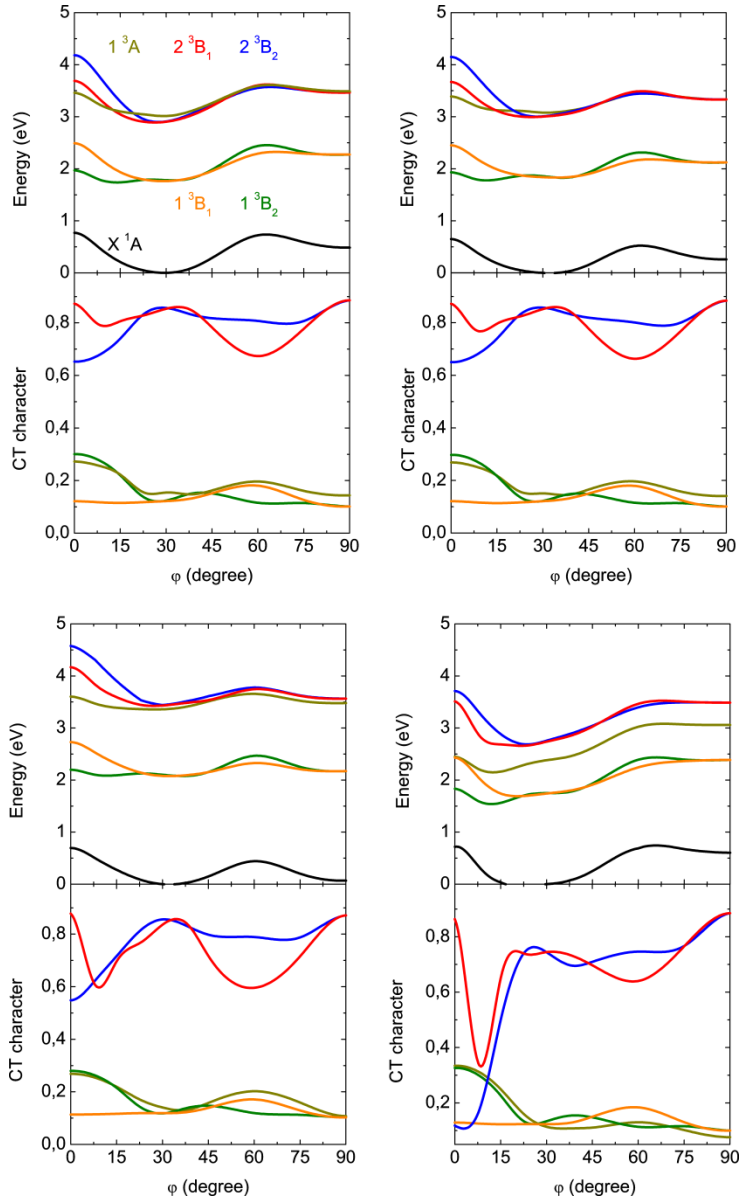


**Figure 33: Comparison of the potential energy curves computed for the torsional motion. The upper plot shows the potential energy curves (PECs) of the ground and the five low lying excited triplet states of the dimers as a function of the torsional coordinate φ. PECs of states with mainly Frenkel (CT) character are indicated by solid (dashed-dotted) lines. The lower plot shows the amount of CT character in the respective wave functions. From left to right: PBI, PTCDA, perylene and DIP.**

It was already mentioned that the MOs which mainly influence the energetically lower electronic excitations of the PBI dimer are primarily located on the perylene core. The HOMO-1, HOMO and LUMO of the PBI dimer possess only negligible contributions from the diimide substituent (Figure 31). This is also found for PTCDA and explains the small differences between PBI, PTCDA and perylene dimers. The MOs of the DIP dimer (LUMO, HOMO, HOMO-2) which dominate the excited $^1B_1$ and $^1B_2$ states (Table 6) strongly resemble the corresponding ones in the other perylene based dyes. This explains the strong similarities between PTCDA, PBI, perylene and DIP dimers for these states. However, the HOMO-1 and the HOMO-4 which are involved in the excitations describing the

$1^1B_3$ and $1^1A$ state are mainly located at the indeno substituents (Table 6 and Figure 31). MOs with comparable shapes and orbital energies do not exist for PBI or PTCDA as the orbitals which are localized on the diimide or anhydride substituent are found at much lower energies. Hence the low lying $1^1A$ and $1^1B_3$ states found for the DIP dimer have to be looked upon as two states which have no counterparts in the PBI, PTCDA or perylene dimers.

The PECs of the corresponding triplet states of all dimers are shown in Figure 33. Positioned below their singlet counterparts they possess similar shapes although the various features are less pronounced. The Frenkel triplet states ($1^3B_1$ and $1^3B_2$) are considerably stabilized in energy compared to their singlet counterparts, because of additional exchange integrals, which lower the energy of Frenkel triplet states. Since exchange integrals vanish quite rapidly as a function of the distance of the involved orbitals, singlet and triplet CT states possess nearly the same energy. As a result the energy splitting between the triplet Frenkel and CT states increased compared to the singlet states. The larger energy gap is accompanied by a reduced mixing of Frenkel and CT diabatic states. While the CT contributions to the predominantly Frenkel singlet states vary between 20% and 45% the contribution to the predominantly Frenkel triplet states amounts to 20% for most orientations.

**Table 7: Dominating single excited configurations of selected triplet transitions for dimers of perylene, PBI, PTCDA and DIP at a rotation angle of 30° (H: HOMO, L: LUMO). The contribution of a given configuration to the wave function (square of its amplitude) is given for all configurations where this value is larger than 0.1.**

| transition | perylene | PBI | PTCDA | DIP |
|---|---|---|---|---|
| $1^1A$ | H-1 → L+2 (0.23) | H-2 → L (0.31) | H-2 → L (0.29) | H-2 → L+1 (0.47) |
| | H-3 → L (0.23) | H-1 → L+2 (0.14) | H-1 → L+2 (0.12) | H-3 → L (0.38) |
| | H → L+8 (0.11) | H → L+4 (0.12) | H-8 → L+1 (0.11) | |
| | H-1 → L+4 (0.10) | H-8 → L+1 (0.11) | | |
| $1^1B_1$ | H → L+1 (0.48) | H → L+1 (0.56) | H → L+1 (0.50) | H → L+1 (0.48) |
| | H-1 → L (0.43) | H-1 → L (0.43) | H-1 → L (0.42) | H-1 → L (0.43) |
| $2^1B_1$ | H-1 → L (0.51) | H-1 → L (0.54) | H-1 → L (0.54) | H-1 → L (0.48) |
| | H → L+1 (0.46) | H → L+1 (0.45) | H → L+1 (0.45) | H → L+1 (0.41) |
| $1^1B_2$ | H → L (0.46) | H → L (0.53) | H → L (0.52) | H → L (0.57) |
| | H-1 → L+1 (0.42) | H-1 → L+1 (0.39) | H-1 → L+1 (0.40) | H-1 → L+1 (0.34) |
| $2^1B_2$ | H-1 → L+1 (0.52) | H-1 → L+1 (0.56) | H-1 → L+1 (0.55) | H-1 → L+1 (0.55) |
| | H → L (0.47) | H → L (0.43) | H → L (0.44) | H → L (0.35) |
| $1^1B_3$ | H → L+2 (0.26) | H-2 → L+1 (0.29) | H-2 → L+1 (0.28) | H-2 → L (0.59) |
| | H-2 → L+1 (0.20) | H → L+2 (0.22) | H → L+2 (0.24) | H-3 → L+1 (0.27) |
| | H → L+4 (0.10) | H-8 → L (0.11) | H-8 → L (0.13) | |

The reduced mixing of CT and Frenkel character can also be understood by the analysis of the amplitudes of the configurations contributing to the excited state wave function. If a single configuration is dominating the excited state, a 50 to 50 mixture of Frenkel and CT character is expected. If

two configurations with equal weight dominate the excited state wave function, a pure Frenkel or CT state should result. This understanding relies on the one determinant description of the hydrogen molecule. Accordingly, it is expected that the triplet states trend to the first case while the singlet states can be assigned to the second one. By comparing Table 5 with Table 7 this assumption can be verified. For the perylene dimer at a rotation angle of 30° the bright $1^1B_1$ state is described by a HOMO to LUMO+1 (80 %) and a HOMO-1 to LUMO (14 %) transition. This mixture is increased to 50 % and 44 % in the case of the $1^3B_1$ state. A HOMO to LUMO (72 %) and HOMO-1 to LUMO+1 (26 %) transition contribute to the dark $1^1B_2$ state, while the corresponding triplet state is again described by an increased mixture of both transitions (46 % and 42 %). Same conclusions can be derived for all other dye dimers and at a rotation angle of 0° as well (Table 6 and Table 8).

**Table 8: Dominating single excited configurations of selected triplet transitions for perylene, PBI, PTCDA and DIP dimers at a rotation angle of 0° (H: HOMO, L: LUMO). The contribution of the configurations to the wave function is depicted in brackets if it is larger than 0.1.**

| transition | perylene | PBI | PTCDA | DIP |
|---|---|---|---|---|
| $1^1A$ | H → L+2 (0.28)<br>H → L+3 (0.26)<br>H-5 → L (0.21)<br>H-2 → L (0.10) | H → L+2 (0.41)<br>H-5 → L (0.41) | H → L+2 (0.47)<br>H-5 → L (0.34) | H-1 → L (0.87) |
| $1^1B_1$ | H-1 → L (0.50)<br>H → L+1 (0.44) | H-1 → L (0.48)<br>H → L+1 (0.44) | H-1 → L (0.48)<br>H → L+1 (0.44) | H-2 → L (0.47)<br>H → L+1 (0.44) |
| $2^1B_1$ | H → L+1 (0.51)<br>H-1 → L (0.49) | H → L+1 (0.51)<br>H-1 → L (0.48) | H → L+1 (0.52)<br>H-1 → L (0.48) | H → L+1 (0.51)<br>H-2 → L (0.49) |
| $1^1B_2$ | H → L (0.86) | H → L (0.88) | H → L (0.88) | H → L (0.89) |
| $2^1B_2$ | H-1 → L+1 (0.50)<br>H-2 → L+2 (0.16)<br>H → L (0.10) | H-1 → L+1 (0.79) | H-1 → L+1 (0.78) | H-9 → L (0.32)<br>H-3 → L+1 (0.31)<br>H-5 → L+2 (0.12)<br>H-1 → L+6 (0.12) |
| $1^1B_3$ | H-4 → L (0.79)<br>H → L+4 (0.15) | H-4 → L (0.49)<br>H → L+3 (0.35) | H-4 → L (0.48)<br>H → L+3 (0.35) | H-4 → L (0.49)<br>H → L+2 (0.33) |

Furthermore the energy related to the Davydov splitting between the Frenkel triplet states is reduced compared to the singlet states. This can be rationalized by the fact that the splitting of the triplet states is determined by Dexter terms, whereas for singlet states Förster terms are relevant which are significantly larger in magnitude.[298] As for the singlet states, strong similarities in the shapes of the triplet state PECs can be observed for all molecular compounds under study. Due to similar origins, from a detailed discussion is refrained.

## 6.3 Energies of the first excited states as a function of a shift motion

Most crystal structures of perylene dyes are arranged such that the constituting molecular entities within the unit cell are shifted with respect to each other (Figure 10). To characterize variations in the electronic structure as a function of a translational motion I computed the PECs of the ground state and five electronically excited singlet states of PTCDA, PBI, perylene, and DIP dimers as a function of longitudinal shifts along the X-axis (see Figure 34).

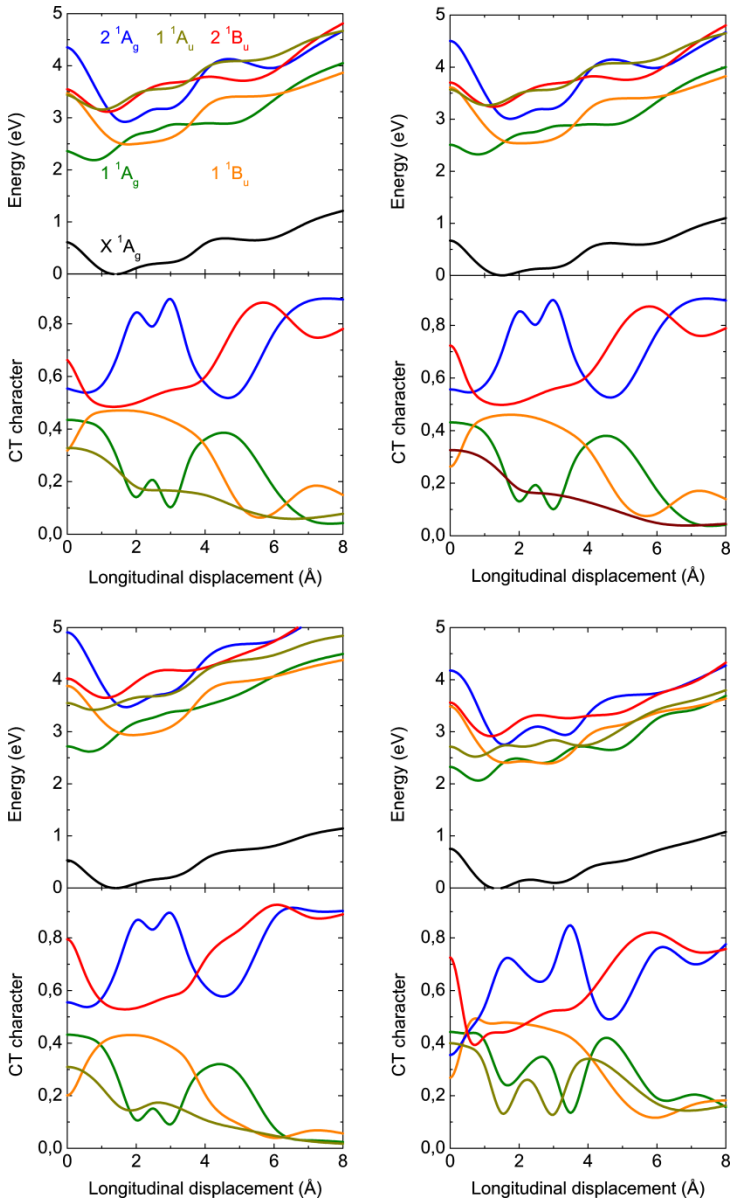


**Figure 34: Comparison of the potential energy curves (upper row) computed for the shift motion along the X-axis (see Figure 10). The graphs are arranged according to Figure 30. From left to right: PBI, PTCDA, perylene and DIP. The lower row indicates the respective contribution of the CT state to the overall wave function.**

The PECs of the corresponding triplet states are imaged in Figure 35. To characterize the states both figures also highlight the amount of CT character for each state as a function of linear longitudinal displacement X (Figure 13). The most important orbitals are displayed in Figure 31 while Table 6 and Table 9 contain the dominating excited configurations of the computed singlet states for X = 0 Å and 1.5 Å, respectively. The irreducible representations for the $D_2$-symmetric rotated dimers correspond to the $C_i$ symmetric shifted dimers as follows: A to $A_u$, $B_1$ to $B_u$, $B_2$ to $A_g$.

**Table 9: Dominant configurations of selected singlet excited states of perylene, PBI, PTCDA and DIP dimers at shifts of 1.5 Å (H: HOMO, L: LUMO). The contribution of the respective configurations to the wave function is depicted in brackets if it is larger than 0.1 (the order of the irreducible representations matches that in Table 5 and Table 6 for the torsional motion).**

| transition | perylene | PBI | PTCDA | DIP |
|---|---|---|---|---|
| $1^1A_u$ | H-3 → L (0.41)<br>H-1 → L+2 (0.23)<br>H → L+3 (0.18) | H-3 → L (0.70) | H-3 → L (0.41) | H-2 → L+1 (0.47)<br>H-3 → L (0.47) |
| $1^1B_u$ | H → L (0.96) | H → L (0.97) | H → L (0.97) | H → L (0.96) |
| $2^1B_u$ | H-1 → L+1 (0.95) | H-1 → L+1 (0.96) | H-1 → L+1 (0.96) | H-1 → L+1 (0.92) |
| $1^1A_g$ | H-1 → L (0.88)<br>H → L+1 (0.10) | H-1 → L (0.88)<br>H → L+1 (0.10) | H-1 → L (0.88)<br>H → L+1 (0.10) | H-1 → L (0.84)<br>H → L+1 (0.13) |
| $2^1A_g$ | H → L+1 (0.88)<br>H-1 → L (0.10) | H → L+1 (0.89) | H → L+1 (0.89) | H → L+1 (0.84)<br>H-1 → L (0.14) |
| $1^1B_g$ | H → L+2 (0.40)<br>H-2 → L (0.12)<br>H-3 → L+1 (0.12)<br>H-1 → L+3 (0.12) | H-2 → L (0.69) | H-2 → L (0.69) | H-2 → L (0.91) |

Obvious similarities in the electronic structures of PBI and PTCDA dimers are again reflected in the shapes of the PECs as well as in the characters of the individual states (Figure 34 and Figure 35, upper row, as well as Table 6 and Table 9). As for the torsional motion the two lower lying states ($1^1A_g$, $1^1B_u$) have a predominantly Frenkel character, while for the two higher lying ones ($2^1A_g$, $2^1B_u$) the CT character predominates. Along the longitudinal displacement $1^1A_g$ and $1^1B_u$ cross each other several times. In the case of the PBI dimer the $1^1A_g$ state, which corresponds to the $1^1B_2$ state of the torsional motion, represents the lowest lying singlet excited state for 0 Å < X < 1.6 Å and 3.6 Å < X < 6.3 Å. The $1^1B_u$ state, which represents the bright state, corresponds to the $1^1B_2$ state of the torsional motion. The vertical excitation energy of the bright $1^1B_u$ state at the lowest energy configuration of the ground state is 2.54 eV and 2.60 eV for PBI and PTCDA, respectively. As for the torsional motion the similarities in vertical excitation energies hold for the whole PEC. Again, differences in the topology of the PECs mainly originate from differences in the shape of the ground state PECs. Similar effects

are found for the predominantly CT states ($2^1B_u$, $2^1A_g$). For the PBI dimer the energy differences between predominantly Frenkel and CT $^1B_u$ states (0.62 eV in average) are considerably larger in average than for the torsional motion 0.17 eV). Despite the larger energy gap between the Frenkel and CT states, the character mixings are comparable to those found along the torsional motion.

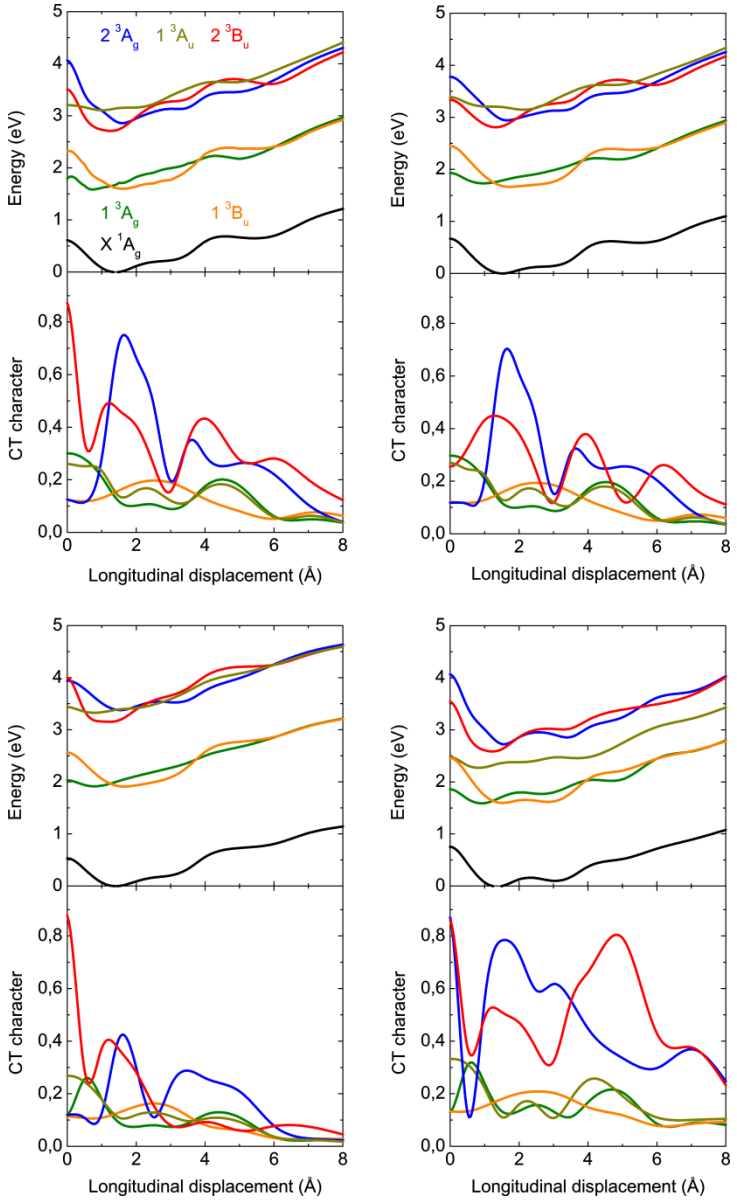


**Figure 35: Potential energy curves (PECs) of the ground and five low lying excited triplet states of the dimers as a function of the translational motion along the longitudinal axis. The graphs are composed like in Figure 30. From left to right: PBI, PTCDA, perylene and DIP.**

The deviations between PBI and PTCDA dimers on one hand and perylene and DIP dimers on the other also resemble the variations that have been previously discussed for the torsional motion. Accordingly, for perylene dimers the energies of the $1^1A_g$ and $1^1B_u$ states are shifted by 0.5 eV in average compared to the PBI dimer, i.e. by the same value as for the torsional motion. Overall, the

shapes of the PECs and characters of the states compare well to the PBI and PTCDA counterparts. The $^1A_u$ state which corresponds to the $^1A$ state of the torsional motion differs from its PBI counterpart for the same reasons as discussed above (Table 6 and Table 9). For DIP dimer the $1^1A_g$ and $1^1B_u$ states are again red shifted in comparison to their PBI counterparts. As for the torsional motion the $1^1B_u$ and $2^1B_u$ DIP dimer states are nearly isoenergetic for 0 Å $\leq$ X $\leq$ 0.5 Å. However, this is not the case for PBI or PTCDA dimers. The reasons are identical to those discussed for the torsional motion. The $^1A_u$ crosses the $1^1B_u$ at about 2.6 Å for the same reasons as discussed for the $^1A$ - $1^1B_1$ crossing at a torsional coordinate of $\varphi$ = 25°. However, despite this crossing the $^1A_u$ state remains less important for the exciton energy transfer since its minimum is located 0.5 eV above the minimum of the $^1A_g$ state.

**Table 10: Dominating single excited configurations of selected triplet transitions for perylene, PBI, PTCDA and DIP dimers at shifts of 1.5 Å (H: HOMO, L: LUMO). The contribution of the configurations to the wave function is depicted in brackets if it is larger than 0.1 (the irreducible representations are sorted in a way to match the order for the rotational motion).**

| transition | perylene | PBI | PTCDA | DIP |
|---|---|---|---|---|
| $1^1A_u$ | H → L+4 (0.17) | H → L+3 (0.24) | H → L+2 (0.28) | H-2 → L+1 (0.42) |
| | H-8 → L (0.16) | H-3 → L (0.14) | H-9 → L (0.19) | H-3 → L (0.41) |
| | H-3 → L (0.14) | H-9 → L (0.14) | H-1 → L+2 (0.16) | |
| | H-1 → L+6 (0.12) | H-7 → L+1 (0.14) | H-7 → L+1 (0.14) | |
| | | H-1 → L+4 (0.11) | H-3 → L (0.11) | |
| $1^1B_u$ | H → L (0.68) | H → L (0.71) | H → L (0.71) | H → L (0.71) |
| | H-1 → L+1 (0.24) | H-1 → L+1 (0.22) | H-1 → L+1 (0.22) | H-1 → L+1 (0.22) |
| $2^1B_u$ | H-1 → L+1 (0.38) | H-1 → L+1 (0.49) | H-1 → L+1 (0.47) | H-1 → L+1 (0.56) |
| | H-3 → L (0.18) | H → L (0.15) | H-4 → L (0.15) | H → L (0.17) |
| | H → L (0.13) | H-4 → L (0.14) | H → L (0.14) | |
| $1^1A_g$ | H-1 → L (0.58) | H-1 → L (0.60) | H-1 → L (0.61) | H-1 → L (0.58) |
| | H → L+1 (0.32) | H → L+1 (0.32) | H → L+1 (0.31) | H → L+1 (0.33) |
| $2^1A_g$ | H → L+1 (0.25) | H → L+1 (0.54) | H → L+1 (0.50) | H → L+1 (0.59) |
| | H → L+5 (0.17) | H-1 → L (0.30) | H-1 → L (0.27) | H-1 → L (0.35) |
| | H-1 → L (0.16) | | | |
| | H-7 → L (0.15) | | | |
| | H-4 → L+1 (0.12) | | | |
| $1^1B_g$ | H → L+6 (0.16) | H-7 → L (0.23) | H-7 → L (0.25) | H-2 → L (0.77) |
| | H-1 → L+4 (0.15) | H-1 → L+3 (0.19) | H-1 → L+2 (0.22) | H-3 → L+3 (0.11) |
| | H-6 → L (0.14) | H-5 → L (0.22) | H → L+4 (0.21) | |
| | H-5 → L (0.13) | H → L+4 (0.12) | H-9 → L+1 (0.12) | |
| | H → L+2 (0.11) | | | |
| | H-8 → L+1 (0.10) | | | |

The corresponding PECs of the triplet states for all dimers are shown in Figure 35 and the analysis of the dominating single excited configurations in Table 10. As for the torsional motion the PECs are

positioned below their singlet counterparts. Shapes of the involved states are again very similar and the underlying reasons correspond to those already discussed for the torsional motion. The Frenkel excited triplet states ($1\ ^3A_g$, $1\ ^3B_u$) are mostly well separated from all higher lying excited states. This is not the case for the CT triplet states ($2\ ^3A_g$, $2\ ^3B_u$), where states with the same symmetry are close. This explains the strong variations in the character analysis in Figure 35 for the different materials. Expect for DIP, the $2\ ^3A_g$ and $2\ ^3B_u$ states are mostly Frenkel in character for shifts larger than 3 Å. The CT states should be found for higher lying states possessing the same symmetry.

These similarities again strongly indicate that the differences in optical properties of perylene based dyes (e.g. absorption and emission spectra, exciton diffusion lengths) do not result from difference in the electronic structures of the involved dyes but from the relative orientation of monomers in the respective crystal, or thin film structures.

# 7. Solvatochromic shifts for perylene based materials

**Abstract**

*For a further improvement of organic solar cells an understanding of microscopic processes determining the device efficiency is crucial. Most theoretical approaches concern bulk effects only partly. Especially, the influence of a polarizable surrounding is often neglected which could affect the order of local Frenkel and charge transfer (CT) excited states. On the example of perylene based materials, a TD-HF approach is used in combination with a polarizable continuum model (PCM) to question the properties of photo-excited states in the bulk. Only higher order methods like the spin-component-scaled approximate coupled-cluster-approach at 2$^{nd}$ order (SCS-CC2) can provide an accurate description of both kinds of excited states, for which a PCM procedure is not feasible. Linear relations between the transition dipole moment and the solvatochromic shifts are applied parameterized on TD-HF level of theory to extrapolate SCS-CC2 results for a polarizable surrounding. The reliability of the results was proven on a system with a small molecular solvent shell, for which SCS-CC2 calculations are possible. For perylene based materials a significant solvatochromic red shift of Frenkel states is predicted which always exceeds the one of the CT states. As a result, the lowest excited states are predicted to be Frenkel ones even in the bulk.*

Functionalized polycyclic aromatic molecules extensively applied in the field of organic optoelectronic devices like thin film transistors[299], photovoltaics[49] or light emitting diodes.[300,301] For a further development of such organic materials the understanding of the basic processes of charge and energy transport and the predictability of optoelectronic properties is crucial. This aim is hard to achieve not only due to a strong dependence of these properties on intermolecular interactions but also due to an influence of the polarizable surrounding on them.[168,219,262,284-286] The task becomes even more complicated due to the existence locally excited Frenkel-type and charge-transfer (CT) states (see Figure 36) which interact differently with a polarizable environment.[75,273,294,302] While Frenkel states can interact via Förster and Dexter couplings, only Dexter coupling is possible for CT states.[114-116,207] Furthermore, Frenkel states interact only with their transition densities to the environment, while a polarizable surrounding can stabilize local charges of CT states.

The influence of a polarizable surrounding on PBI aggregates was studied by Veldman et al., who performed time-resolved photoluminescence and photoinduced absorption experiments on a J-aggregate like structure of a PBI-molecule bound to a perylene monoimid.[303] They found that the

Frenkel and CT states are almost isoenergetic. While in toluene the CT state is 0.06 eV lower in energy than the lowest Frenkel excited state, in cyclohexane the reversed order was measured.

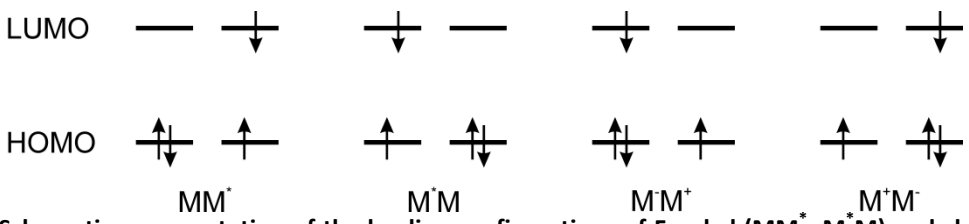


**Figure 36: Schematic representation of the leading configurations of Frenkel ($MM^*$; $M^*M$) and charge transfer ($M^+M^-$; $M^-M^+$) excited states of a dimer. Each configuration is represented by four orbitals, the two LUMOs (upper lines) and the two HOMOs (lower lines) which are localized on the two monomers.**

In the case of 3,4,9,10-perylene tetracarboxylic dianhydride (PTCDA), Scholz and co-workers suggested that environmental effects shift a CT state 1.5 eV below the bright Frenkel state.[211,272] This estimation is based on computations of the ionization potential, the electron affinity and the polaronic stabilization of an anion and cation in a crystal at infinite distance. For most systems considerably weaker effects are expected as a complete charge separation is unlikely and CT states strongly mix with their Frenkel counterparts.[230,273] As a consequence, in CT states a dipole rather than independent charges exists and the suggested stabilization can be understood as an upper limit for the solvatochromic shift.

This view is supported by Heinz et al., who modelled experimental solvatochromic shifts of perylene in solid and liquid *n*-alkane matrixes by using an empirical approach.[304] The shifts are in the range from 0.14 eV to 0.21 eV. For PBI monomers Munoz-Losa et al. studied transition dipole moments and electronic coupling parameters, which are defined as half of the energy splitting of the Frenkel states (Davydov splitting).[120,305] They simulated the influence of a surrounding by CIS/6-31G(d) in combination with a PCM description for toluene. This approach predicts a lowering of the electronic coupling parameter by 0.05 eV and an increase of the transition dipole moment by 0.9 Debye. Curutchet et al.[306] and Neugebauer et al.[307] studied a PBI dimer solvated in water in a face-to-face alignment with an intermolecular distance of 3.5 Å. They also used CIS/6-31G(d), but within the QM/MMpol approach. This approach takes into account the polarization interaction between MM charges and induced dipoles. A lowering of the excitation energy by 0.13 eV was found, while a shift of 0.12 eV were predicted by the PCM method.[306] For both approaches the electronic coupling parameter is decreased by 0.04 eV, while the transition dipole moment is increased by 0.8 Debye predicted bye QM/MMpol method and 0.7 Debye by the PCM procedure. This is in line with the findings of Munoz-Losa et al. for the monomer.[305]

All these studies focused on effects on the two lowest Frenkel states for a fixed PBI dimer. In the present work the investigations are extended on the first excited Frenkel and CT states and their

shapes of potential energy curves (PECs) including important intermolecular degrees of freedom. This extension is essential because intermolecular motions strongly influence the absorption as well as emission spectra and are responsible for exciton self-trapping.[168,255,296]

In computations, intermolecular interactions between adjacent molecules can be properly included by using a super-molecular approach. The influence of a polarizable surrounding can be included with a polarizable continuum model (PCM). However, such approaches can only be combined with methods like CIS, time-dependent Hartree-Fock theory (TD-HF) or time-dependent density functional theory (TD-DFT), which have serious problems in describing excited states of aggregates correctly. CIS and TD-HF overestimate the excitation energies of CT states, while most TD-DFT approaches give a wrong energy order of Frenkel and CT states and often produce wrong shapes of PECs.[172,230,308] Higher order methods describe the excited states accurately like the spin-component-scaled approximate Coupled Cluster method 2nd order (SCS-CC2), which are not feasible in combination with PCM due to the computationally very demanding iterative procedure.

## 7.1 Solvent effects on the ground and first excited states

PECs of the ground and first excited states are shown Figure 37 for the studied torsional motion under vacuum conditions and for both considered solvents. The ground state is energetically stabilized almost constantly due to solvation. The averaged effect for 13 dimer arrangements is larger in water (2.18±0.06 eV) than in cyclohexane (0.71±0.06 eV). In the case of the shift motion 14 dimer arrangements with longitudinal shifts between 0 Å and 8 Å were calculated. Also for these structures the ground state is lowered to a larger extend in water (2.07±0.09 eV) than in cyclohexane (0.67±0.04 eV). This trend between the different solvents can be explained by the fact that its influence on the ground state energy is mediated by the dielectric constant.

In Table 11 excitation energies under vacuum conditions and in both solvents are listed for a dimer arrangement at $\varphi$ = 30°. The solvatochromic shifts are larger in cyclohexane than in water due to the larger refractive index $n$ of cyclohexane. By using TD-HF in combination with IEFPCM it results that the excitation energies of the optically bright Frenkel state ($1^1B_1$, water: 0.11 eV, cyclohexane: 0.14 eV) are always stabilized to a larger extent than the ones of the dark Frenkel state ($1^1B_2$, water: 0.04 eV, cyclohexane: 0.06 eV). According to Bayliss' law the solvatochromic shift of the excitation energy depends on the magnitude of the transition dipole moment which explains the larger shifts in the bright state.[242] The electronic coupling parameter is equal to half of the energy splitting of the Frenkel states. Consequently, it shrinks by 0.03 eV (0.04 eV) in water (cyclohexane) for the rotated dimer. This is in line with the findings of Curutchet et al. who found a value of 0.04 eV in water for a different dimer arrangement.[306] The excitation energies of the CT states ($2^1B_1$, $2^1B_2$) are almost not changed due to solvation. This leads to the conclusion that a solvent stabilizes the excitation energies to Frenkel states to a larger extent than the one to CT states. The CT states have only a small transition density, which explains the limited influence of the solvent on its excitation energies according to Bayliss' law.[242] Due to the high symmetry of the PBI dimer, charge separation on different monomers is inhibited after excitation into CT states. Thus, the CT states are not significantly stabilized by the solute, which could change if symmetry breaking effects are considered.

The transition dipole moment rises for all states by solvation which is in agreement with Chako's law.[244] For the optically bright Frenkel state ($1^1B_1$) a larger increase was found for cyclohexane (1.89 Debye) than for water (1.74 Debye), which was expected due the larger refractive index of cyclohexane. However, the increase of the transition dipole moment is larger than the one reported by Curutchet et al. who reported an increase of 0.7 Debye for water.[306] The dark Frenkel state ($1^1B_2$) gains only limited transition dipole moment by solvation (water: 0.42 Debye, cyclohexane: 0.47 De-

bye) due to its small transition dipole moment under vacuum conditions which holds also for the CT states.

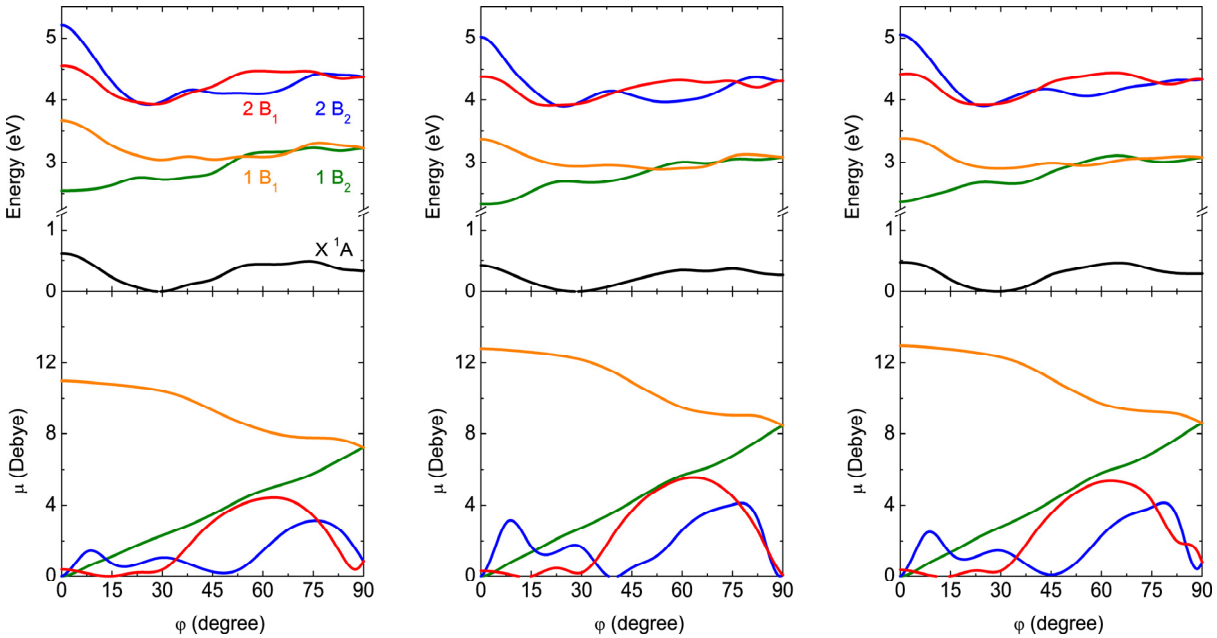


**Figure 37: PECs of the PBI dimer at the TD-HF-D/6-311G** level for the ground and first excited states as a function of the torsional motion (upper panels). The curves were calculated for different solvents (from left to right: vacuum conditions, water, cyclohexane). The lower panels show the corresponding transition dipole moments.**

**Table 11: Excitation energies (in eV) of the first excited states and in brackets transition dipole moments (in Debye) are listed on TD-HF-D/6-311G** level of theory in combination with IEFPCM. A face-to-face stacked dimer is considered which is rotated around the stacking axis by φ = 30°. The solvents are ordered by increasing refractive index.**

| State | Vacuum | | Water | | Cyclohexane | |
|---|---|---|---|---|---|---|
| $1\,^1B_2$ | 2.72 | (2.30) | 2.68 | (2.73) | 2.66 | (2.77) |
| $1\,^1B_1$ | 3.04 | (10.43) | 2.94 | (12.17) | 2.90 | (12.32) |
| $2\,^1B_1$ | 3.94 | (0.37) | 3.95 | (0.20) | 3.95 | (0.31) |
| $2\,^1B_2$ | 3.97 | (1.07) | 3.98 | (1.66) | 3.97 | (1.47) |

Similar conclusions for the solvatochromic shift can be gained from other intermolecular arrangements. Corresponding data for a shifted dimer arrangement along the longitudinal axis can be found in Figure 38 and Table 12. The excitation energy of the optically bright Frenkel state ($1\,^1B_u$) is lowered by 0.08 eV (0.13 eV) in water (cyclohexane), while the one of the dark Frenkel state ($1\,^1A_g$) is reduced by only 0.03 eV (0.05 eV). The electronic coupling parameter shrinks by 0.03 eV (0.04 eV). This is still in line with the findings of Curutchet et al. who found a value of 0.04 eV in water for a different dimer arrangement.[306] The transition dipole moment rises due to the solvation for all

states. For the optically bright Frenkel state a larger increase was found for cyclohexane (2.01 Debye) than for water (1.85 Debye) which is in agreement with Chako's law.[244]

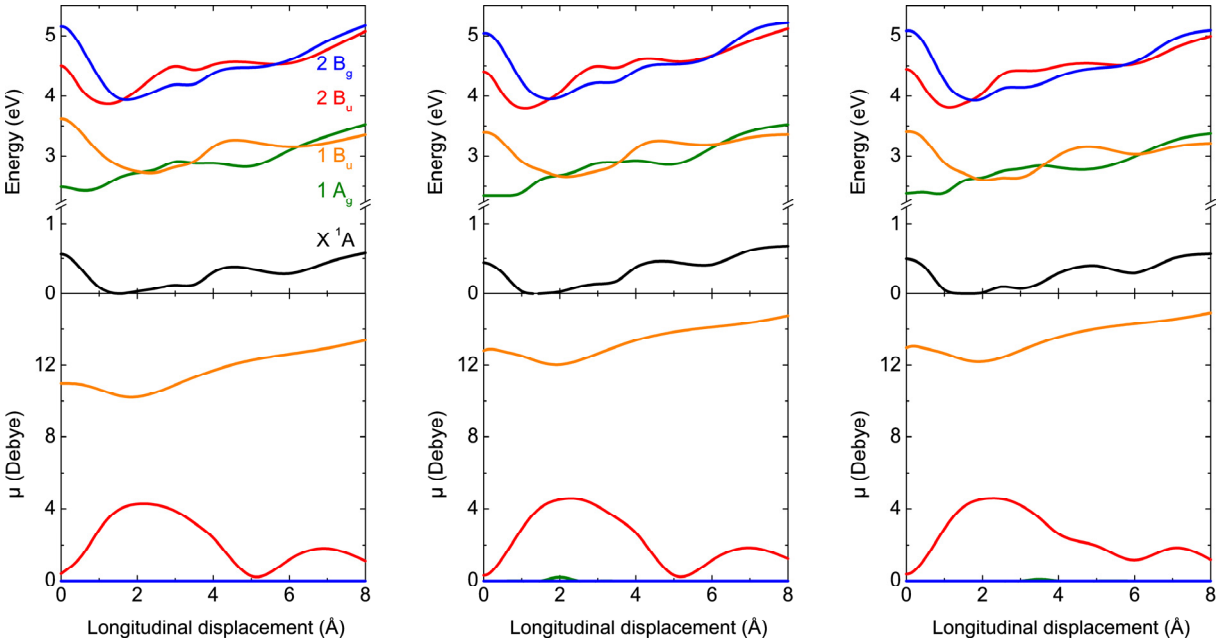


**Figure 38: PECs of the PBI dimer at the TD-HF-D/6-311G** level for the ground and first excited states as a function of the shift motion (upper panels). The curves were calculated for different solvents (from left to right: vacuum conditions, water, cyclohexane). The lower panels show the corresponding transition dipole moments.**

**Table 12: Excitation energies (in eV) of the first excited states and in brackets transition dipole moments (in Debye) are listed on TD-HF-D/6-311G** level of theory in combination with IEFPCM. A face-to-face stacked dimer is considered which is shifted along the longitudinal axis by 1.5 Å. The ground state energies are given relative to its value in vacuum for a PBI dimer rotated by φ = 30°. The excited states are ordered to match the series in Table 11.**

| State | Vacuum | | Water | | Cyclohexane | |
|---|---|---|---|---|---|---|
| $1^1A_g$ | 2.64 | (0.00) | 2.61 | (0.00) | 2.59 | (0.00) |
| $1^1B_u$ | 2.84 | (10.30) | 2.76 | (12.15) | 2.72 | (12.30) |
| $2^1B_u$ | 3.90 | (3.92) | 3.87 | (4.07) | 3.87 | (4.10) |
| $2^1A_g$ | 3.97 | (0.00) | 3.92 | (0.00) | 3.97 | (0.00) |

Very similar results can be found for PTCDA as shown in Table 13 and Table 14. This is in line with the literature, where very similar electronic structures of the first excited states were reported for a large range of perylene based materials.[273] Consequently, the findings for the solvatochromic shifts should hold for this class of materials as well.

**Table 13: Excitation energies (in eV) of the first excited states of PTCDA and in brackets transition dipole moments (in Debye) are listed on TD-HF-D/6-311G** level of theory in combination with IEFPCM. A face-to-face stacked dimer is considered which is rotated around the stacking axis by φ = 30°.**

| State | Vacuum | | Water | | Cyclohexane | |
|---|---|---|---|---|---|---|
| $1\,^1B_2$ | 2.82 | (2.28) | 2.77 | (2.71) | 2.76 | (2.74) |
| $1\,^1B_1$ | 3.13 | (10.20) | 3.02 | (12.00) | 2.99 | (12.07) |
| $2\,^1B_1$ | 4.06 | (0.36) | 4.06 | (0.14) | 4.06 | (0.29) |
| $2\,^1B_2$ | 4.08 | (1.08) | 4.08 | (1.89) | 4.08 | (1.55) |

**Table 14: Excitation energies (in eV) of the first excited states of PTCDA and in brackets transition dipole moments (in Debye) are listed on TD-HF-D/6-311G** level of theory in combination with IEFPCM. A face-to-face stacked dimer is considered which is shifted along the longitudinal axis by 1.5 Å. The ground state energies are given relative to its value in vacuum for a PBI dimer rotated by φ = 30°. The excited states are ordered to match the series in Table 11.**

| State | Vacuum | | Water | | Cyclohexane | |
|---|---|---|---|---|---|---|
| $1^1A_g$ | 2.73 | (0.00) | 2.71 | (0.00) | 2.69 | (0.00) |
| $1^1B_u$ | 2.93 | (10.08) | 2.86 | (11.97) | 2.81 | (12.04) |
| $2^1B_u$ | 4.02 | (3.76) | 3.98 | (3.97) | 3.99 | (3.96) |
| $2^1A_g$ | 4.09 | (0.00) | 4.09 | (0.00) | 4.09 | (0.00) |

## 7.2 Linear model to estimate solvatochromic shifts

According to Bayliss' and Chako's laws, there exist linear relations between $\Delta E^{ex}$ and $\mu^2$ as well as between $f^{vac}$ and $f^{sol}$. Figure 39 plots the corresponding linear relations for the considered rotated PBI dimers. It is evident that the linear relations still hold for the complex cavities of IEFPCM. In Table 15 fitted values are listed for the slopes and intercepts according to the equations ( 121 ) and ( 120 ). For the Frenkel states the slope $c^{ex}$ is larger in cyclohexane than in water, because the solvatochromic shift of the excitation energies increases faster with $\mu^2$ in cyclohexane due to the larger refractive index. A solvatochromic shift of the excitation energy at zero transition dipole moment $\Delta E_0^{ex}$ of 31 meV (47 meV) was found in water (cyclohexane). As mentioned before, this is caused by the remaining transition density despite the cancelation of the dipole moments in the dark Frenkel state. Again the magnitude of $\Delta E_0^{ex}$ is larger in cyclohexane than in water due to its larger polarizability (and refractive index).

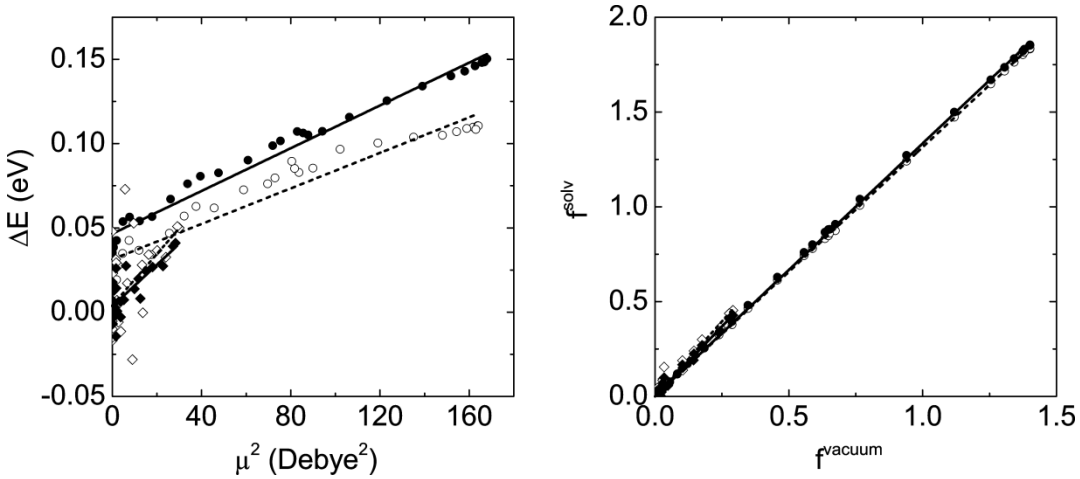


**Figure 39: Solid points and diamonds correspond to cyclohexane and non-filled ones to water as solvent for a PBI dimer. Points represent the predominantly Frenkel states (1 $^1B_1$, 1 $^1B_2$), whereas diamonds stands for states (2 $^1B_1$, 2 $^1B_2$) with dominating CT character. Solid lines correspond to extrapolations for cyclohexane and dashed ones for water. Left: A linear dependency is shown of the solvatochromic red shift of the excitation energy ΔE on the squared transition dipole moment $\mu^2$ in solution. Right: The oscillator strengths $f^{solv}$ of the solvated dimers are proportional to the corresponding oscillator strengths $f^{vac}$ in vacuum.**

In the case of the CT states $c^{ex}$ is larger for water than for cyclohexane. Additionally, the solvatochromic shift of the excitation energies into CT states increase faster with $\mu^2$ than the ones of the Frenkel states, but show almost no shift at vanishing transition dipole moment. However, $\Delta E_0^{ex}$ of the Frenkel states is roughly in the same magnitude as the largest observed shift of the excitation energies to CT states (see Figure 39). Therefore, larger solvatochromic shifts are expected for the Frenkel compared to the CT states.

Large standard deviations are obtained in the linear fits for the CT states which are caused by the noise of the data resulting from mixing in character and avoided crossings with close lying higher states. Such states could possess a significant transition dipole which causes a significant stabilization in solution. Consequently, couplings and avoiding crossings with other states occur in solution but not under vacuum conditions. In contrast to this, the studied Frenkel states are well separated from all other states and such complications do not affect the interpolation. Much smaller standard deviations result for the fitted values (see Table 15). However, the small solvatochromic shift of less than 0.1 eV is by far smaller than its upper limit of around 1.5 eV estimated in the literature.[272]

**Table 15: Parameters for a PBI dimer derived from the linear fits in Figure 39 are listed for the linear model to estimate solvatochromic shifts in PBI dimers. The standard deviations resulting from the linear fit are given as well. The parameters are defined according to the linear relations ( 121 ) and ( 120 ).**

| | Water | | Cyclohexane | |
|---|---|---|---|---|
| | Frenkel | CT | Frenkel | CT |
| $c^{ex}$ ($10^{-4}$ eV/Debye²) | 5.3±0.3 | 15±4 | 6.3±0.2 | 12±2 |
| $\Delta E_0$ ($10^{-2}$ eV) | 3.1±0.2 | 0.4±0.5 | 4.7±0.2 | 0.3±0.2 |
| $c^f$ | 1.314±0.001 | 1.58±0.05 | 1.334±0.003 | 1.47±0.03 |

The oscillator strength in solution is proportional to its magnitude in vacuum (see right graph in Figure 39) which is in agreement with Chako's law.[244] For the oscillator strength of the Frenkel states the slope $\boldsymbol{c^f}$ is larger for cyclohexane than for water due to the different refractive indices of the solvents (see Table 15). The ratio of both slopes (1.02) is slightly smaller than the ratio of the corresponding ones in Chako's formula (1.06). This is a reasonable agreement with the data because the formula is valid only for spherical cavities. A similar linear dependence can be derived for the CT states. Again, the corresponding gradient is larger in water than in cyclohexane. According to the large noise of the data, this trend is not unambiguous.

Similar linear dependencies are found for the solvatochromic shifts of the excitation energies and oscillator strength of PTCDA dimers (see Table 16). Only minor deviations to the fitted PBI values are found. These results demonstrate that the solvatochromic shifts of the excitation energies and transition dipole moments are very similar for both materials. According to the strong similarity of the electronic structure of the first excited states in a wide range of perylene based materials,[273] it is expected that the linear model for the solvatochromic shifts can be transferred to these molecules as well.

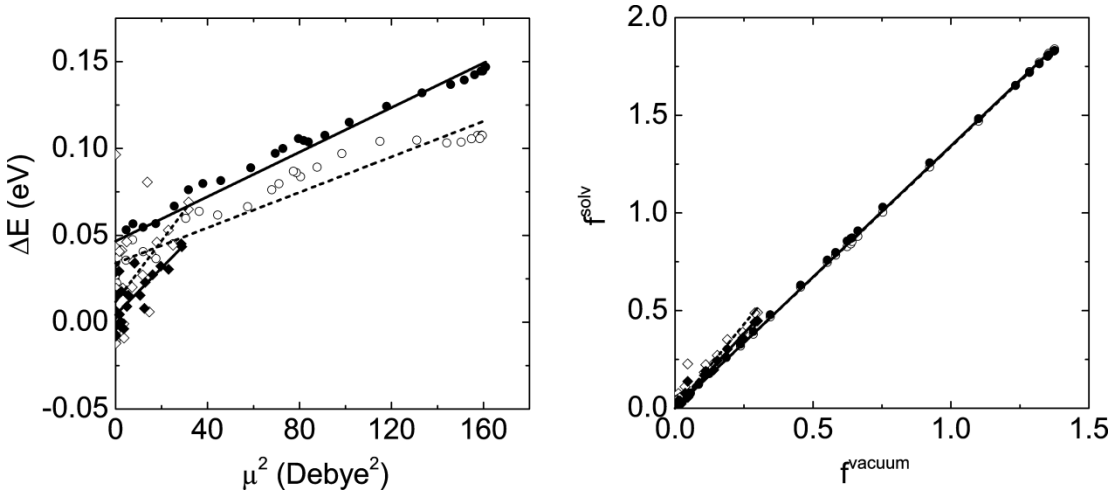


**Figure 40: Solid points and diamonds correspond to cyclohexane and non-filled ones to water as solvent for a PTCDA dimer. Points represent the predominantly Frenkel states (1 $^1B_1$, 1 $^1B_2$), whereas diamonds stands for states (2 $^1B_1$, 2 $^1B_2$) with dominating CT character. Solid lines correspond to extrapolations for cyclohexane and dashed ones for water. Left: A linear dependency is shown of the solvatochromic red shift of the excitation energy ΔE on the squared transition dipole moment $\mu^2$ in solution. Right: The oscillator strengths $f^{solv}$ of the solvated dimers are proportional to the corresponding oscillator strengths $f^{vac}$ in vacuum.**

**Table 16: Parameters for a PTCDA dimer derived from the linear fits in Figure 40 are listed for the linear model to estimate solvatochromic shifts in PBI dimers. The standard deviations resulting from the linear fit are given as well. The parameters are defined according to the linear relations ( 121 ) and ( 120 ).**

| | Water | | Cyclohexane | |
|---|---|---|---|---|
| | Frenkel | CT | Frenkel | CT |
| $c^{ex}$ ($10^{-4}$ eV/Debye²) | 5.1±0.3 | 18±5 | 6.4±0.2 | 14±2 |
| $\Delta E_0$ ($10^{-2}$ eV) | 3.4±0.3 | 1.2±0.5 | 4.7±0.2 | 0.4±0.2 |
| $c^f$ | 1.339±0.001 | 1.72±0.06 | 1.343±0.003 | 1.53±0.03 |

## 7.3 Solvent effects for SCS-CC2

A recent study showed that TD-HF and SCS-CC2 predictions differ in the energetic separation of Frenkel and CT states, but closely resemble each other in the character of the states and the corresponding transition dipole moments.[230] Even the shapes of the computed PECs are very similar which are very sensitive to couplings between the states. Consequently, the influence of a polarizable surrounding on the excitation energies and transition dipole moments is expected to be very similar as well. In a first attempt the solvatochromic shifts calculated with TD-HF//IEFPCM are simply transferred to SCS-CC2 results under vacuum conditions. Table 17 lists the resulting excitations energies for a PBI dimer arrangement at ϕ = 30°. Corresponding PECs for the complete torsional motion are in Figure 41. As mentioned before, the solvatochromic shift of the bright Frenkel state ($1^1B_1$) exceeds the one of the CT states ($2^1B_1$, $2^1B_2$) in the TD-HF//IEFPCM description. The energetic separation of the Frenkel and CT states increases from 0.04 eV under vacuum conditions to 0.15 eV (0.18 eV) in water (cyclohexane). As a result, the energetic order of the Frenkel and CT states does not change due to a polarizable surrounding predicted by a simple transfer of solvatochromic shifts.

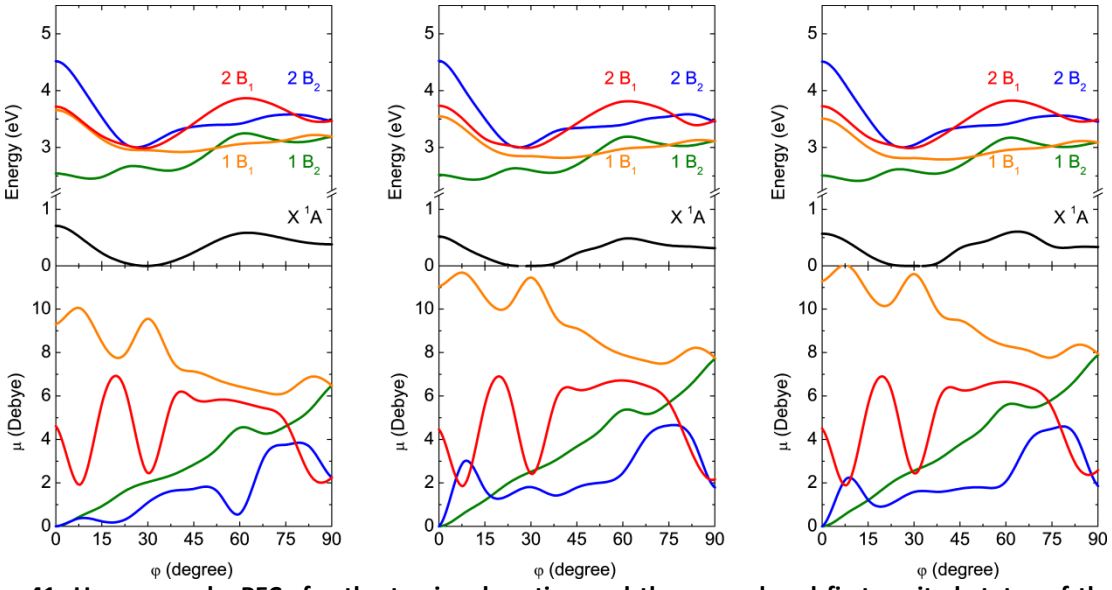


**Figure 41: Upper panels: PECs for the torsional motion and the ground and first excited states of the PBI dimer at SCS-CC2/TZV(P) level of theory by a direct transfer of the TD-HF solvatochromic shift to the SCS-CC2 data under vacuum conditions. The curves were calculated for different solvents (from left to right: vacuum conditions, water, cyclohexane). Lower panels: Corresponding transition dipole moments.**

**Table 17: Excitation energies (in eV) of the first excited states of a PBI dimer and in brackets transition dipole moments (in Debye) are listed on SCS-CC2/TZV(P) level of theory by a direct transfer of the TD-HF solvatochromic shift to the SCS-CC2 data under vacuum conditions. A face-to-face stacked dimer is considered which is rotated around the stacking axis by φ = 30°.**

| State | Vacuum | | Water | | Cyclohexane | |
|---|---|---|---|---|---|---|
| $1^1B_2$ | 2.64 | (2.04) | 2.60 | (2.51) | 2.59 | (2.56) |
| $1^1B_1$ | 2.95 | (9.56) | 2.85 | (11.45) | 2.81 | (11.61) |
| $2^1B_1$ | 2.99 | (2.45) | 3.00 | (2.42) | 2.99 | (2.44) |
| $2^1B_2$ | 3.05 | (1.09) | 3.05 | (1.81) | 3.05 | (1.58) |

This first attempt to get solvatochromic shifts for SCS-CC2 can be validated by using the linear relations for the solvatochromic shifts parameterized before. The estimation of solvent effects is done by first calculating the the oscillator strengths in solution $f_{solv}$ by equation ( 120 ). They are subsequently used to get the excitation energy in solution $E_{solv}^{ex}$ via:

$$E_{solv}^{ex} = \frac{1}{2}(E_{\mathrm{vac}}^{ex} - \Delta E_0^{ex}) + \sqrt{\frac{1}{4}(E_{\mathrm{vac}}^{ex} - \Delta E_0^{ex})^2 - \frac{3}{2}\frac{\hbar^2 e^2}{m_e} c^{ex} f_{solv}} \quad (123)$$

This equation is derived from ( 121 ) together with ( 118 ) and the definition of the solvatochromic shift of the excitation energy $\Delta E^{ex} = E_{vac}^{ex} - E_{solv}^{ex}$. The relative ground state energies are unchanged. A global energy shift is expected because an obvious trend associated with the dimer arrangement was not observed in the TD-HF-D//IEFPCM calculations. Finally, the transition dipole moments in solution are calculated via ( 118 ) with the excitation energies and oscillator strengths in solution.

In this second attempt, the excitation energies into the optically bright Frenkel state ($1^1B_1$) is stabilized by 0.10 eV (0.13 eV) in water (cyclohexane), whereas the one into dark Frenkel state ($1^1B_2$) is stabilized by 0.03 eV (0.05 eV). Consequently the electronic coupling parameter shrinks by 0.03 eV (0.04 eV) which is still in line with the findings of Curutchet et al.[306] Due to smaller transition dipole moments calculated with SCS-CC2, the solvent effects are slightly smaller than the ones predicted by TD-HF. Under vacuum conditions the excitation energies of the optically bright Frenkel state ($1^1B_1$) are closely below the one of the lowest CT state ($2^1B_1$). The linear relations predict that the energy gap increases in solution (vacuum: 0.04 eV, water: 0.12 eV, cyclohexane: 0.15 eV) to a smaller amount than for the direct transfer of the TD-HF//IEFPCM solvatochromic shifts. This is caused by a strong mixing between Frenkel and CT character in all considered states in the SCS-CC2 picture. This is indicated by a larger transition dipole moment of the CT states compared to the TD-HF ones which induces some solvatochromic shifts also for the CT states. In Figure 42 PECs for the ground and first

excited states are shown calculated by SCS-CC2 and corrected for solvent effect by the linear relations. The increase of the energetic separation of the bright Frenkel state ($1^1B_1$) and the lowest CT state ($2^1B_1$) in solution holds for the complete torsional motion. As for the PECs calculated with TD-HF//IEFPCM (see Figure 37), a solvent induces only minor changes on the PECs. Therefore, curves calculated under vacuum conditions should keep valid also for a polarizable surrounding.

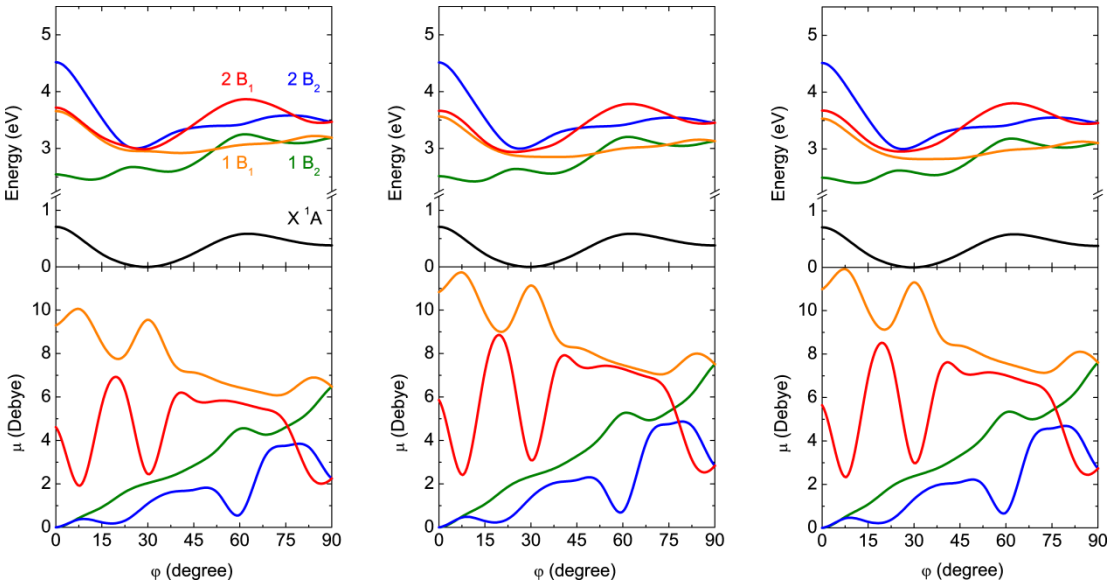


**Figure 42: PECs for the torsional motion and the ground and first excited states of the PBI dimer at scaled SCS-CC2/TZV(P) level by using the linear model (upper panels). The curves were calculated for different solvents (from left to right: vacuum conditions, water, cyclohexane). The lower panels show the corresponding transition dipole moments.**

**Table 18: Excitation energies (in eV) of the first excited states of a PBI dimer and in brackets transition dipole moments (in Debye) are listed on SCS-CC2/TZV(P) level of theory using the linear model. A face-to-face stacked dimer is considered which is rotated around the stacking axis by φ = 30°.**

| State | Vacuum | | Water | | Cyclohexane | |
|---|---|---|---|---|---|---|
| $1^1B_2$ | 2.64 | (2.04) | 2.61 | (2.35) | 2.59 | (2.38) |
| $1^1B_1$ | 2.95 | (9.56) | 2.86 | (11.14) | 2.82 | (11.30) |
| $2^1B_1$ | 2.99 | (2.45) | 2.97 | (3.09) | 2.98 | (2.98) |
| $2^1B_2$ | 3.05 | (1.09) | 3.04 | (1.37) | 3.04 | (1.33) |

In conclusion, the stabilization of the Frenkel states relative to the CT states is less pronounced by using the linear relations rather the direct transfer of the solvatochromic shifts. However, despite minor differences both methods agree well. Also, a direct transfer of the solvatochromic shifts calculated by TD-HF//IEFPCM to SCS-CC2 results should be reliable.

## 7.5 Molecular solvation

A PBI dimer is studied, which is rotated by $\varphi$ = 30° and solvated by a small molecular solvent shell of twelve methane molecules as a model for cyclohexane (see Figure 12). For such a system SCS-CC2 calculations are demanding but still possible. Since a small solvent shell is taken into account, bulk effects are only partly covered in these test computations. Nevertheless, it should reveal shortcomings of the PCM results due to molecular solvation effects. Different solvations of both monomers could lead to a further stabilization of CT states due to induced charge localizations.

First, TD-HF//IEFPCM results for a PBI dimer in cyclohexane (see Table 11) are compared to TD-HF ones for the molecularly solvated dimer (see Table 19). Some differences are found for the excitation energies of the Frenkel states ($1^1$B, $2^1$B). Especially the excitation energy of the optically bright Frenkel state ($2^1$B) is predicted higher in energy by 0.12 eV for the partly solvated system than for the IEFPCM solvated one. The excitation energy of the dark Frenkel state ($1^1$B) differs only by 0.04 eV. However, if IEFPCM is employed also for the molecularly solvated system, the differences almost vanishes ($1^1$B: 0.01 eV, $2^1$B: 0.03 eV). This indicates shortcomings of the small solvation shell. Especially the solvatochromic shift of the bright state is underestimated. However, both CT states are stabilized by only 0.01 eV due to the implicit solvation with and without an additional IEFPCM procedure. Consequently, symmetry breaking effects are of minor importance in the studied molecularly solvated system.

**Table 19: Excitation energies (in eV) and in brackets transition dipole moments (in Debye) for the 30° rotated PBI dimer with 12 methane molecules calculated with different approaches. Methane was chosen as a model for cyclohexane. Therefore, the latter solvent was taken for the IEFPCM procedure. *Direct transfer of the TD-HF//IEFPCM solvatochromic shifts to the SCS-CC2 data under vacuum conditions.**

| State | TD-HF | | + IEFPCM | | SCS-CC2 | | +IEFPCM* | |
|---|---|---|---|---|---|---|---|---|
| $1^1$B | 2.70 | (2.26) | 2.67 | (2.63) | 2.54 | (2.04) | 2.51 | (2.41) |
| $2^1$B | 3.02 | (11.37) | 2.93 | (12.64) | 2.83 | (9.72) | 2.74 | (10.99) |
| $3^1$B | 3.93 | (0.41) | 3.93 | (0.35) | 2.88 | (4.76) | 2.88 | (4.70) |
| $4^1$B | 3.96 | (1.06) | 3.96 | (1.37) | 2.93 | (1.09) | 2.93 | (1.40) |

On SCS-CC2 level of theory the molecular solvation induces a stabilization of the excitation energy of around 0.1 eV for all considered states compared to the results under vacuum condition. Therefore, a solvatochromic shift is already included in the system by the molecular solvent. For this reason only a transfer of the TD-HF//IEFPCM solvatochromic shifts is possible for this system. The linear model introduced before corrects for the complete solvent shell and would include double counting of solvent effects here. If one compares the SCS-CC2 results by using the linear model for cyclohex-

ane (see Table 18) with the SCS-CC2 results with the TD-HF//IEFPCM solvatochromic shifts for the molecularly solvated system, larger shifts of around 0.1 eV are found for the molecularly solvated system. However, the energetic separation of the Frenkel and CT states is not affected by this (0.14 eV). As a result, the energetic order of the excited states does not change also if molecular solvent effects are considered. However, this could change if symmetry breaking effects occur.

## 7.6 Influence of solvent effects on exciton self-trapping

The IEFPCM calculations analyzed in this work suggest an energetic stabilization of the bright Frenkel state relative to the dark state. In principal this could have an influence on the exciton self-trapping mechanism in α-PTCDA introduced in chapter 5.2 by changing the underlying potential energy surfaces. Exciton self-trapping was found to happen close to a conical intersection of the bright and dark Frenkel state which is accessible from the crystal structure alignment.[296] In Figure 43 potential energy curves are shown for the minimal energy path from the Franck-Condon region (distance = 0 Å) towards the conical intersection (distance = 0.8 Å), which was introduced before in Figure 22. The curves are calculated for a PTCDA dimer with SCS-CC2/SVP under vacuum conditions and for cyclohexane as a solvent by using the linear model defined in chapter 7.2.

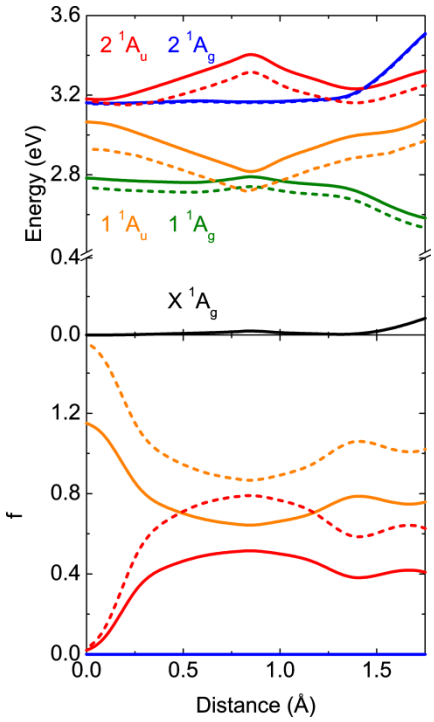


**Figure 43: Potential energy curves (upper panel) and oscillator strength (lower panel) of the ground and first excited states of a PTCDA dimer for the minimal energy path shown in Figure 22. Solid lines correspond to SCS-CC2/SVP calculations under vacuum conditions, while the dashed lines give the corresponding data for cyclohexane as a solvent.**

There are some deviations between Figure 22 and Figure 43, because the first one is calculated by using a QM/MM method and the latter for the dimer. Further deviations originate from the fact that the minimal energy path in Figure 22 is extracted from the splined 2D-plots in Figure 19, while explicit SCS-CC2 calculations where performed for Figure 43.

However, the bright Frenkel state ($1^1A_u$) is stabilized by 0.14 eV by cyclohexane, which is the largest shift among all considered excited states as expected. However, this only minor affects the conical intersection with the dark Frenkel state ($1^1A_g$). It is slightly re-located towards the Frank-Condon region (distance = 0 Å). The influence of PTCDA as a solvent instead of cyclohexane should be comparable due to similar refractive indexes ($n_{cyclohexane}$ = 1.4, $n_{\alpha\text{-PTCDA}}$ = 1.6)[220,309]. Therefore, the polarizable surrounding in the α-PTCDA crystal does not change the exciton self-trapping mechanism in α-PTCDA.

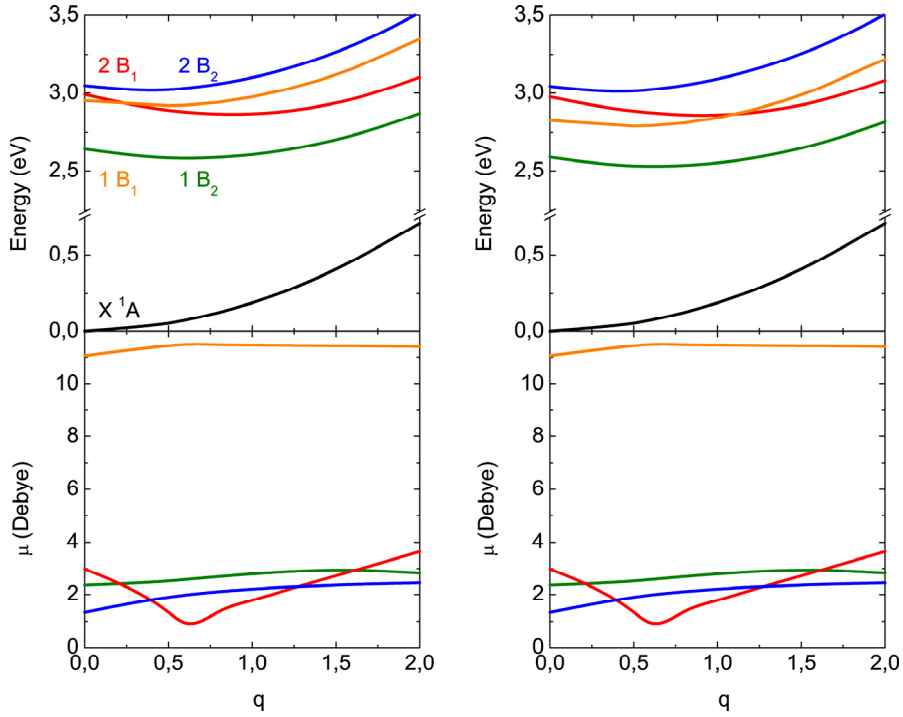


**Figure 44: Extrapolation of SCS-CC2 PECs for the EET trapping motion from a ground state (q = 0) to the anion/cation geometry (q = 1). The curves are splined following the state character (exitonic or CT) not the adiabatic states to make the extrapolation possible. The left graph corresponds to calculations in vacuum, whereas on the right an extrapolation for cyclohexane is shown.**

Solvent effects are also studied for the EET self-trapping mechanism in twisted aggregates of PBI introduced in chapter 5.1. This mechanism is based on a intermolecular motion of the dimer from the ground state structure of the monomers to a structure, where one monomer has the geometry of the anion and the other the one of the cation.[255] This structure stabilizes one of the CT states and destabilizes the other one. The stabilized CT state is populated because it crosses the optically bright Frenkel state via a conical intersection. Afterwards the population is rapidly transferred to the lowest excited state, which is the dark Frenkel state. Finally, emission will take place out of this state.[168] The model is based on SCS-CC2/SVP calculations in the gas phase. The PECs for the trapping motion are adapted for solvent effects by the linear model (see Figure 44). The crossing of the Frenkel and CT

state is shifted upwards in energy such that it is energetically 0.03 eV above the Franck-Condon region. At a first glance this should hamper the population transfer from the Frenkel to the CT state, which is central for the introduced self-trapping mechanism. However, experiments showed that the de-population of the Frenkel state occurs with a time constant of 215 fs. On this time scale a polarization of the solvent environment is expected, which should stabilize the CT state due to symmetry breaking effects. As mentioned in the last chapter these effects are expected to be in the order of 0.05 eV – 0.1 eV which should compensate the upward shift of the crossing point above the Franck-Condon region. As a result, self-trapping is expected to occur even in solution. At the moment of excitation, the Frenkel states are lower in energy than the CT ones and during reorganization of the solvent the CT ones become lower in energy, which should end up in the self-trapping mechanism published before.[255]

In summary solvent effects do not influence exciton self-trapping in twisted PBI aggregates as well as in α-PTCDA. Therefore, the neglect of such effects in the discussion of self-trapping for these materials in chapter 5 was justified.

# 8. Summary

Organic solar cells gain advantage over inorganic ones due to their flexibility and low production costs. However, they possess significantly lower power conversion efficiencies. One reason for this drawback is their low exciton diffusion length ($L_D$), which is defined by the distance an exciton is transported after photo-absorption. Is this distance shorter than the one to the next interface, at which charge separation can occur, the contribution of the exciton to current production gets lost. In the context of this dissertation very long ranged $L_D$ were simulated for perylene-based materials under ideal conditions. This leads to the conclusion that the short $L_D$ values in existing materials result from an extrinsic immobilization, which happens at grain boundaries or impurities, and from an intrinsic immobilization. The latter, which is a specific material property, is based on a relaxation of the exciton into so-called self-trapping states. An in-depth understanding of the atomistic processes defining self-trapping is essential to developing materials with long $L_D$ in the future, in which intrinsic immobilization is prevented.

For the development of such a mechanistic understanding it is crucial that a clear relationship between molecular structure and $L_D$ is available. This is given by single crystals of diindeno perylene (DIP) and $\alpha$-perylene tetracarboxylic anhydride ($\alpha$-PTCDA). An extraordinary large $L_D$ of 90 nm was measured for the first one, while the latter possesses only 22 nm. Part of this thesis was to deliver reasons for this discrepancy. As shown in Figure 45, exciton diffusion is limited by emission and self-trapping. Emission occurs on a much larger time scale than the other two processes and, additionally, the lifetime of the exciton is comparable in DIP and $\alpha$-PTCDA. Consequently, only self-trapping comes into question to explain the different $L_D$ values. For this reason both materials are suited for an example to develop an atomistic understanding of self-trapping.

There was a debate in the literature, whether Frenkel or charge-transfer (CT) states are responsible for self-trapping in perylene-based materials. Therefore, it was necessary to establish a quantum chemical method, which would describe both types of electronic excited states equally well. A method evaluation pointed out that, on the one hand, TD-DFT generally predicted the excitation energy of CT states too low. This results in wrongly shaped potential energy surfaces, which also affects the ones of the Frenkel states. On the other hand, TD-HF overestimates the excitation energy of CT states. As a result, only SCS-CC2 is able to describe Frenkel as well as CT states with sufficient accuracy. The enormous computational cost of the final method limits the quantum chemical system to a dimer. This reduction is justified by the fact that an ultrafast localization of the exciton on a dimer was observed experimentally (see Figure 45).

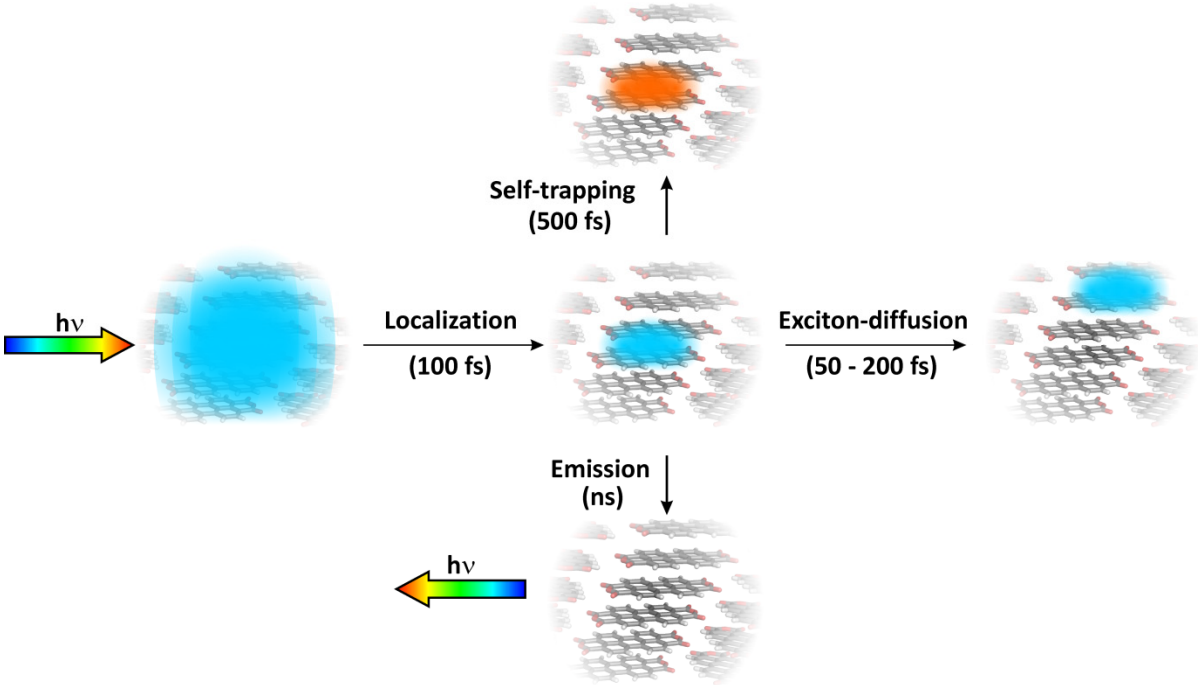


**Figure 45: Illustration of different photo-physical processes after electronic excitation in α-PTCDA.**

One reason for the different self-trapping in DIP and α-PTCDA could lie in the electronic structure. However, it was possible to demonstrate that a wide range of perylene-based materials possess no significant differences in their electronic structures. Consequently, such differences can be neglected for the explanation of immobilization mechanisms for the exciton.

A further possible explanation could be polarization effects in the crystal, which influences the electronic structure of perylene based materials differently. Especially their influence on CT states, which are located above the optically bright Frenkel state, was in question because such states could be stabilized by a polarizable surrounding. A significant influence of polarization effects on all considered states were excluded by using a polarizable continuum model (PCM).

Hence, the small $L_D$ values in α-PTCDA are an evidence for self-trapping, which produces a crystal structure built up by π-stacks, while the one of DIP is of herringbone type. Since polarization effects can be neglected, is the dimer only via steric restrictions influenced by the crystal. Hence, a method describing self-trapping has to consider such effects, so that a mechanical embedding QM/MM approach is sufficient. Now, potential energy surfaces were calculated, on which wave packet dynamics were subsequently performed. In this way, atomistic mechanisms for the immobilization of excitons were described for the first time in organic materials.

As one example, self-trapping was studied in crystals of α-PTCDA by potential energy surfaces, which map an intermolecular shift motion of the dimer in the crystal. An immobilization of excitons occurs within 500 fs, which results from an irreversible energy loss together with a local deformation

of the crystal lattice. This prevents a further transport of the exciton. Self-trapping is based on ultrafast dissipative molecular dynamics (black arrow in Figure 46) in the optically bright Frenkel state (orange), in which the exciton is generated, and towards a conical intersection with a dark Frenkel state (green). Here a transfer of the exciton into the dark state is possible, which leads to a further relaxation of the exciton in the final state (white arrow). In the case of DIP, this immobilization does not proceed due to high barriers, which prevent a dynamic of the molecules towards the conical intersection. These barriers result from the herringbone type packing motif in the DIP crystal. This discrepancy in the dynamics explains the different $L_D$ values in DIP and α-PTCDA.

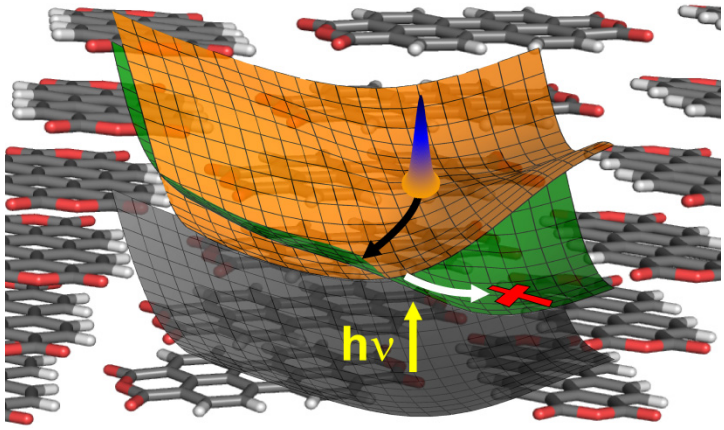


**Figure 46: Potential energy surface of the ground (grey) and first two excited Frenkel states (orange, green) in α-PTCDA. CT states are located well separated above the two Frenkel states and are omitted for this reason. The exciton is generated in the energetically higher Frenkel state (orange) in the Franck-Condon region (blue wave packet).**

In a further example, an exciton immobilization was found in helical π-aggregates of perylene tetracarboxylic bisimide (PBI) molecules (see Figure 47). Self-trapping is caused by a relaxation mechanism, in which the exciton is transferred by asymmetric vibrations of the aggregate from the bright to a dark Frenkel state within 200 fs, whereby the transition is mediated by a CT state. However, the CT state is almost non-populated during the whole mechanism so that its participation could not yet be proven experimentally. This entire procedure is solely possible in helical aggregates, because only for such structures is there a CT state located next to the bright Frenkel state. At the final Frenkel state a torsional motion around the π-stacking axis is possible so that the loss in energy and the local rearrangement of the aggregate structure occurs, which means a self-trapping of the exciton. This mechanism is in perfect agreement with all available experimental data.

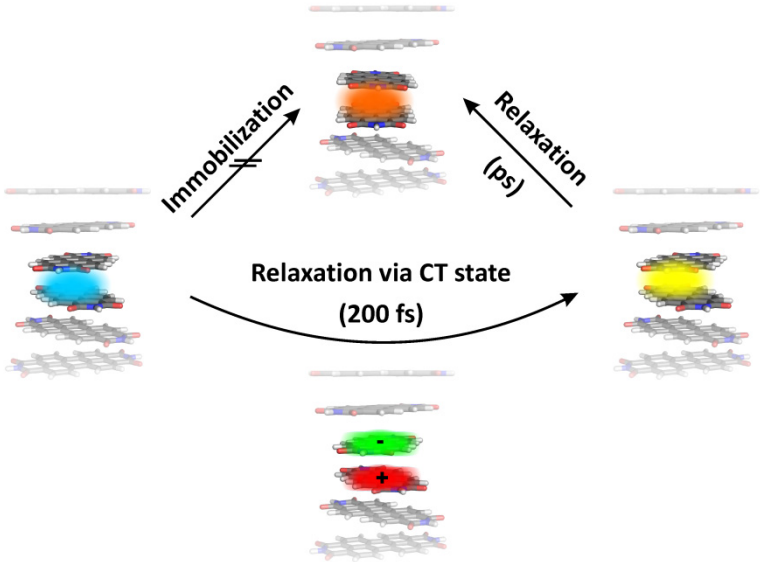


**Figure 47: Illustration of the immobilization of an exciton in helical PBI aggregates. Self-trapping does not occur directly, but is mediated by a CT state.**

These insights allow the conclusion that in future materials for organic solar cells an irreversible and ultrafast deformation of aggregates after photo-absorption must be avoided. Only in this way long $L_D$ values can be achieved and exciton self-trapping can be prevented. However, small $L_D$ values are always predicted in helical aggregates of perylene-based materials, because exciton immobilization occurs already due to small molecular motions. For this reason such aggregates are inappropriate for the use in organic solar cells. Long $L_D$ values are expected for aggregate structures with long intermolecular shifts or molecules with bulky substituents.

# Zusammenfassung

Organische Solarzellen sind ihren anorganischen Pendants aufgrund ihrer Flexibilität und ihren geringen Produktionskosten überlegen. Allerdings besitzen sie eine deutlich geringere Energieumwandlungseffizienz. Eine Ursache dafür ist die geringe Exzitonen-Diffusionslänge ($L_D$), die angibt, wie weit ein durch Photoabsorption erzeugtes Exziton im Material transportiert wird. Ist die Distanz zu einer Grenzfläche, an der Ladungstrennung stattfinden kann, größer als $L_D$, geht der Energiebeitrag des Exzitons für die Stromerzeugung verloren. Im Rahmen dieser Dissertation wurden sehr lange $L_D$ für Perylen-basierte Materialien unter idealen Bedingungen simuliert. Auf diese Weise konnte gezeigt werden, dass die sehr kurzen $L_D$ in realen Materialien aus einer extrinsischen Immobilisierung von Exzitonen an Korngrenzen und Verunreinigungen sowie aus einer intrinsischen Immobilisierung resultieren. Eine intrinsische Immobilisierung, deren Effektivität materialspezifisch ist, basiert auf einer Relaxation in sogenannten Self-Trapping-Zuständen. Ein tieferes Verständnis der dem Self-Trapping zugrunde liegenden atomistischen Prozesse ist notwendig, um zukünftig Materialien mit langen $L_D$ entwickeln zu können, bei denen eine intrinsische Exzitonen-Immobilisierung verhindert wird.

Für die Entwicklung eines solchen mechanistischen Verständnisses ist das Vorliegen einer eindeutigen Korrelation zwischen der molekularen Anordnung und der $L_D$ unabdingbar. Diese weisen Einkristalle von Diindenoperylen (DIP) und α-Perylen-tetracarboxyl-anhydrid (α-PTCDA) auf. Bei ersteren wurde eine außergewöhnlich lange $L_D$ von 90 nm und bei letzteren nur von 22 nm gemessen. Teil dieser Arbeit war es, Gründe für diese unterschiedlich langen $L_D$ zu finden. Wie in Abbildung 45 dargestellt, kann Exzitonen-Diffusion durch Emission und Self-Trapping eingeschränkt werden. Die Emission findet in einem viel größeren Zeitrahmen statt als die beiden anderen Prozesse. Da sich zudem die Lebensdauer des Exzitons in DIP und α-PTCDA nicht signifikant unterscheidet, kommt nur Self-Trapping als Ursache für die unterschiedlichen $L_D$ in Frage. Aus diesem Grund eignen sich diese beiden Materialien, um ein atomistisches Verständnis des Self-Trappings exemplarisch an ihnen zu erarbeiten.

Bisher wurde in verschiedenen Publikationen diskutiert, ob Frenkel- oder Ladungstrennungs- (CT-) Zustände für das Self-Trapping in Perylen-basierten Materialien verantwortlich sind. Deshalb musste zuerst eine quantenchemische Methode gefunden werden, die beide Typen von elektronisch angeregten Zuständen verlässlich beschreibt. Eine Methodenevaluation zeigte einerseits, dass TD-DFT die Anregungsenergien von CT-Zuständen generell zu niedrig angibt. Daraus resultieren falsch geformte Potentialflächen, wovon sogar die Frenkel-Zustände betroffen sind. Andererseits überschätzt TD-HF die Anregungsenergien von CT-Zuständen. Daher ist nur SCS-CC2 in der Lage, beide Zustandstypen

mit ausreichender Genauigkeit wiederzugeben. Der erhebliche Rechenaufwand dieser Methode lässt aber nur ein Dimer als quantenchemisches System zu. Diese Reduktion des Systems ist allerdings auch durch die gemessene ultraschnelle Lokalisierung des Exzitons auf ein Dimer gerechtfertigt (siehe Abbildung 45).

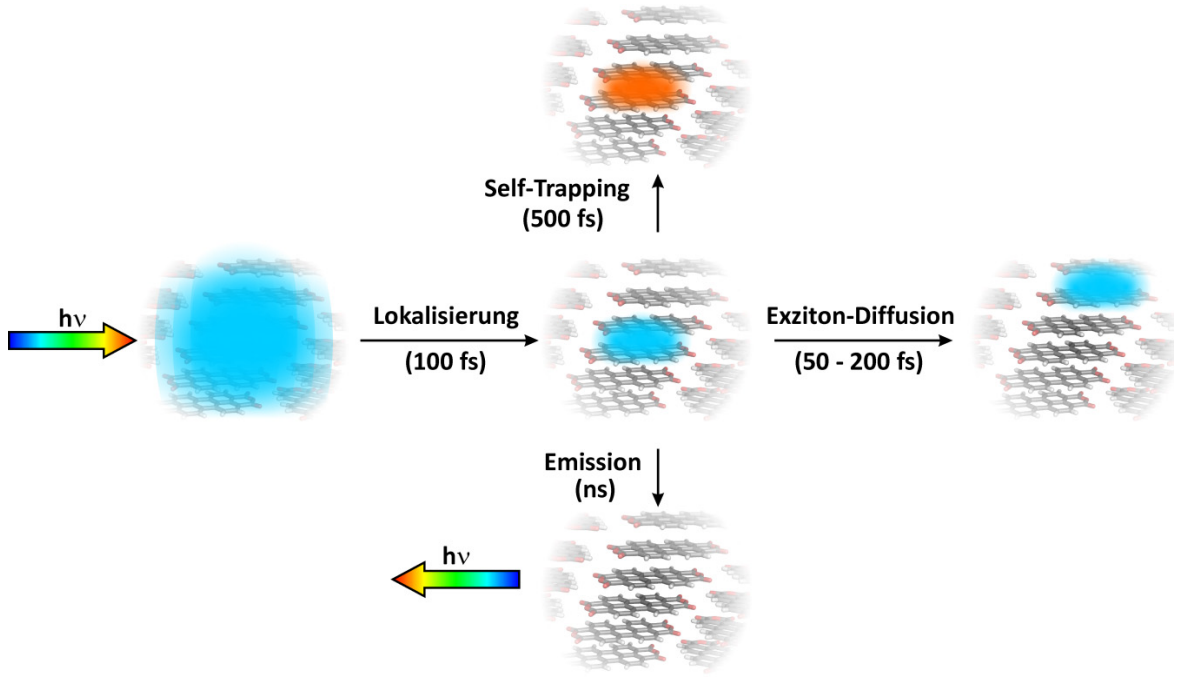


**Abbildung 45: Darstellung verschiedener photophysikalischer Prozesse nach der elektronischen Anregung in α-PTCDA.**

Mutmaßlich könnten Differenzen in der elektronischen Struktur in DIP und α-PTCDA für das unterschiedliche Self-Trapping verantwortlich sein. Allerdings konnte gezeigt werden, dass es für viele Perylen-basierte Materialien keine signifikanten Unterschiede in der elektronischen Struktur gibt, wodurch diese für die Aufklärung von Immobilisierungsmechanismen zu vernachlässigen waren.

Eine weitere mögliche Begründung wäre in Polarisationseffekten im Kristall zu suchen, welche die elektronische Struktur in Perylen-basierten Materialien unterschiedlich beeinflussen. Vor allem ihr Einfluss auf CT-Zustände, die oberhalb des optisch hellen Frenkel-Zustandes liegen, war fraglich, weil sie durch eine polarisierbare Umgebung energetisch abgesenkt werden könnten. Ein signifikanter Einfluss von Polarisationseffekten konnte aber für alle Zustände mittels eines polarisierbaren Kontinuum-Modells (PCM) ausgeschlossen werden.

Die geringe $L_D$ im α-PTCDA ist folglich ein Indiz für ein Self-Trapping, das durch die Kristallstruktur aus π-Stapeln evoziert wird, welche in DIP fischgrätenartig ist. Da Polarisationseffekte auszuschließen sind, übt der Kristall lediglich durch sterische Restriktionen einen Einfluss auf das Dimer aus. Daher musste die Methode für die Beschreibung von Self-Trapping nur diese Effekte berücksichtigen, so

dass sich für den Einsatz des *mechanical embedding* QM/MM-Ansatzes entschieden wurde. Nun konnten Potentialflächen berechnet werden, auf denen anschließend eine Wellenpaketdynamik durchgeführt wurde. Diese Vorgehensweise erlaubt es, Mechanismen der Exzitonen-Immobilisierung in organischen Materialien auf einer atomistischen Ebene erstmals zu beschreiben.

Beispielsweise dienten als Erklärung für Self-Trapping in α-PTCDA Potentialflächen, die eine intermolekulare Verschiebung des Dimers im Kristall abbilden. So wurde eine Exzitonen-Immobilisierung innerhalb von 500 fs gefunden (siehe Abbildung 46), die aus einem irreversiblem Energieverlust und einer lokalen Verzerrung der Kristallstruktur resultiert und auf diese Weise den weiteren Transport des Exzitons verhindert. Dahinter verbirgt sich eine ultraschnelle dissipative Molekulardynamik (schwarzer Pfeil in Abbildung 46) im optisch hellen Frenkel-Zustand (orange), in dem das Exziton gebildet wird, zu einer konischen Durchschneidung mit einem dunklen Frenkel-Zustand (grün). Dort findet ein Transfer des Exzitons in den dunklen Zustand statt, in dem es zu einer weiteren Relaxation (weißer Pfeil) kommt. Im Fall von DIP kann diese Immobilisierung aufgrund hoher Energiebarrieren nicht stattfinden. Die Barrieren resultieren aus der fischgrätenartigen Kristallstruktur des DIP und verhindern die Molekulardynamik zur konischen Durchschneidung. Diese Diskrepanzen in der Dynamik erklären die unterschiedlichen $L_D$-Werte für DIP und α-PTCDA.

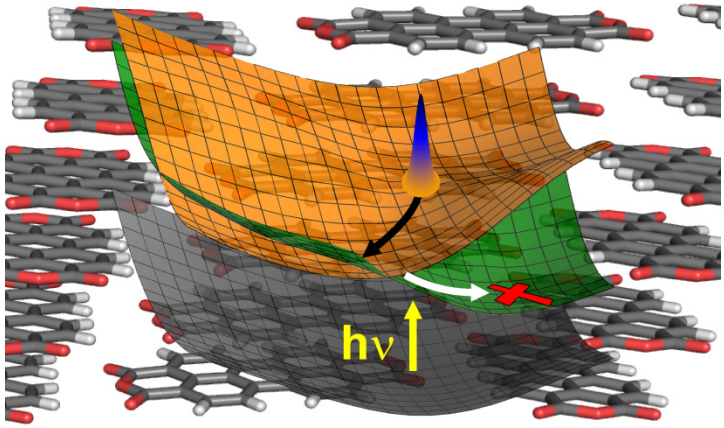


**Abbildung 46: Potentialflächen des Grundzustandes (grau) und der ersten beiden angeregten Frenkel-Zustände (orange, grün) in α-PTCDA. CT-Zustände liegen wohl separiert über den beiden Frenkel-Zuständen und sind daher hier nicht gezeigt. Das Exziton wird im energetisch höheren Frenkel-Zustand (orange) in der Franck-Condon-Region (blaues Wellenpaket) gebildet.**

In einem weiteren Fall wurde eine Exzitonen-Immobilisierung in helikalen π-Aggregaten von Perylen-tetracarboxyl-bisimid (PBI) Molekülen untersucht (siehe Abbildung 47). Hier wird Self-Trapping durch einen Relaxationsmechanismus verursacht, in dem das Exziton durch geringe asymmetrische Schwingungen des Aggregats innerhalb von 200 fs von dem hellen Frenkel- in den dunklen Frenkel-Zustand transferiert wird, wobei dieser Übergang allerdings von einem CT-Zustand vermittelt wird.

Nun wird der CT-Zustand während des gesamten Mechanismus aber kaum populiert, so dass er bisher experimentell nicht nachgewiesen wurde. Der gesamte Vorgang ist nur bei helikalen Aggregaten möglich, weil nur hier CT-Zustände sehr dicht bei dem hellen Frenkel-Zustand liegen. Im finalen Frenkel-Zustand tritt eine Torsionsbewegung um die π-Stapelachse ein, so dass ein Energieverlust und eine lokale Änderung der Aggregatstruktur erfolgt – also ein Self-Trapping des Exzitons. Dieser modellierte Mechanismus steht im Einklang zu allen vorliegenden experimentellen Daten.


**Abbildung 47: Darstellung der Exzitonen Immobilisierung in helikalen PBI-Aggregaten. Self-Trapping geschieht nur indirekt, da ein CT-Zustand den Übergang vom optisch hellen in den dunklen Frenkel-Zustand ermöglicht, in dem eine Immobilisierung stattfindet.**

Diese Erkenntnisse lassen die Schlussfolgerung zu, dass in künftigen Materialen für organische Solarzellen eine irreversible und ultraschnelle Deformation des Aggregats nach der Photoanregung vermieden werden sollte. Nur so kann Self-Trapping von Exzitonen verhindert und lange $L_D$ erreicht werden. Weil eine Exzitonen-Immobilisierung in helikalen Aggregaten von Perylen-basierten Materialien bereits aufgrund kleiner molekularer Bewegungen stattfindet, werden für sie stets kleine $L_D$ vorhergesagt. Solche Aggregate sind daher sie für den Einsatz in organischen Solarzellen ungeeignet. Lange $L_D$ sind dagegen bei Materialien mit stark verschobenen Aggregatstrukturen, das heißt großen intermolekularen Translationen, oder mit sterisch anspruchsvollen Substituenten zu erwarten.

# Bibliography

All cited webpages were lastly accessed around 20 pm at the 8th October 2012.


(1) World Engineers' Convention: http://www.swissengineering-stz.ch/pdf/stz1020114882.pdf, 2011.
(2) National Science Academies of the G8: http://www.nationalacademies.org/onpi/06072005.pdf, 2005.
(3) TU Graz: http://portal.tugraz.at/portal/page/portal/Files/i3070/downloads/skripten/Sonnenenergienutzung/Teil2_Grundlagen.pdf.
(4) BP: http://www.bp.com/liveassets/bp_internet/globalbp/globalbp_uk_english/reports_and_publications/statistical_energy_review_2011/STAGING/local_assets/pdf/statistical_review_of_world_energy_full_report_2011.pdf, 2011.
(5) Energy Information Administration: http://www.eia.gov/oiaf/aeo/electricity_generation.html, 2010; Vol. 2012.
(6) Green, M. A.; Emery, K.; Hishikawa, Y.; Warta, W.; Dunlop, E. D. *Prog. Photovoltaics* **2012**, *20*, 12.
(7) Heliatek GmbH: http://www.heliatek.com/?page_id=119; Vol. 2012.
(8) Li, B.; Wang, L.; Kang, B.; Wang, P.; Qiu, Y. *Sol. Energy Mat. Sol. C.* **2006**, *90*, 549.
(9) Rohr, S. In *Pressemitteilung*; Heliatek GmbH: http://www.heliatek.com/wp-content/uploads/2012/09/120427_PI_Heliatek-Weltrekord-10_7-Prozent-Effizienz.pdf , 2012; Vol. 2012.
(10) Li, C.; Wonneberger, H. *Adv. Mater.* **2012**, *24*, 613.
(11) Nunzi, J. M. *C. R. Physique* **2002**, *3*, 523.
(12) Guenes, S.; Neugebauer, H.; Sariciftci, N. S. *Chem. Rev.* **2007**, *107*, 1324.
(13) Peumans, P.; Yakimov, A.; Forrest, S. R. *J. Appl. Phys.* **2003**, *93*, 3693.
(14) Bredas, J.-L.; Norton, J. E.; Cornil, J.; Coropceanu, V. *Acc. Chem. Res.* **2009**, *42*, 1691.
(15) Bach, U.; Lupo, D.; Comte, P.; Moser, J. E.; Weissortel, F.; Salbeck, J.; Spreitzer, H.; Gratzel, M. *Nature* **1998**, *395*, 583.
(16) Gratzel, M. *Nature* **2001**, *414*, 338.
(17) Nazeeruddin, M. K.; Kay, A.; Rodicio, I.; Humphrybaker, R.; Muller, E.; Liska, P.; Vlachopoulos, N.; Gratzel, M. *J. Am. Chem. Soc.* **1993**, *115*, 6382.
(18) Oregan, B.; Gratzel, M. *Nature* **1991**, *353*, 737.
(19) Hagfeldt, A.; Gratzel, M. *Acc. Chem. Res.* **2000**, *33*, 269.
(20) Mishra, A.; Bäuerle, P. *Ang. Chem.* **2012**, *124*, 2060.
(21) Potscavage, W. J., Jr.; Sharma, A.; Kippelen, B. *Acc. Chem. Res.* **2009**, *42*, 1758.
(22) Shockley, W.; Queisser, H. J. *J. Appl. Phys.* **1961**, *32*, 510.
(23) Pagliaro, M.; Palmisano, G.; Ciriminn, R. *Flexible Solar Cells*; Wiley-VCH: Weinheim, 2008.
(24) Minnaert, B.; Burgelman, M. *Prog. Photovoltaics* **2007**, *15*, 741.
(25) Conibeer, G.; Green, M.; Corkish, R.; Cho, Y.; Cho, E. C.; Jiang, C. W.; Fangsuwannarak, T.; Pink, E.; Huang, Y. D.; Puzzer, T.; Trupke, T.; Richards, B.; Shalav, A.; Lin, K. L. *Thin Solid Films* **2006**, *511*, 654.
(26) Kim, J. Y.; Lee, K.; Coates, N. E.; Moses, D.; Nguyen, T.-Q.; Dante, M.; Heeger, A. J. *Science* **2007**, *317*, 222.
(27) Schueppel, R.; Timmreck, R.; Allinger, N.; Mueller, T.; Furno, M.; Uhrich, C.; Leo, K.; Riede, M. *J. Appl. Phys.* **2010**, *107*.
(28) Miranda, P. B.; Moses, D.; Heeger, A. J. *Phys. Rev. B* **2001**, *64*, 081201.
(29) Brabec, C. J.; Zerza, G.; Cerullo, G.; De Silvestri, S.; Luzzati, S.; Hummelen, J. C.; Sariciftci, S. *Chem. Phys. Lett.* **2001**, *340*, 232.

(30) Parker, I. D. *J. Appl. Phys.* **1994**, *75*, 1656.
(31) Shoaee, S.; An, Z.; Zhang, X.; Barlow, S.; Marder, S. R.; Duffy, W.; Heeney, M.; McCulloch, I.; Durrant, J. R. *Chem. Commun.* **2009**, 5445.
(32) Deibel, C.; Strobel, T.; Dyakonov, V. *Phys. Rev. Lett.* **2009**, *103*.
(33) Mozer, A. J.; Sariciftci, N. S. *C. R. Chimie* **2006**, *9*, 568.
(34) Koster, L. J. A.; Smits, E. C. P.; Mihailetchi, V. D.; Blom, P. W. M. *Phys. Rev. B* **2005**, *72*.
(35) Baumann, A. PhD thesis, Universität Würzburg, 2011.
(36) Kiess, H.; Rehwald, W. *Sol. Energy Mat. Sol. C.* **1995**, *38*, 45.
(37) Bao, Z.; Locklin, J. *Organic Field-Effect Transistors*; Crc Pr Inc: New York, 2007.
(38) Sirringhaus, H.; Brown, P. J.; Friend, R. H.; Nielsen, M. M.; Bechgaard, K.; Langeveld-Voss, B. M. W.; Spiering, A. J. H.; Janssen, R. A. J.; Meijer, E. W.; Herwig, P.; de Leeuw, D. M. *Nature* **1999**, *401*, 685.
(39) Mihailetchi, V. D.; Koster, L. J. A.; Blom, P. W. M.; Melzer, C.; de Boer, B.; van Duren, J. K. J.; Janssen, R. A. J. *Adv. Funct. Mater.* **2005**, *15*, 795.
(40) Mihailetchi, V. D.; van Duren, J. K. J.; Blom, P. W. M.; Hummelen, J. C.; Janssen, R. A. J.; Kroon, J. M.; Rispens, M. T.; Verhees, W. J. H.; Wienk, M. M. *Adv. Funct. Mater.* **2003**, *13*, 43.
(41) Ioffe Institute: http://www.ioffe.rssi.ru/SVA/NSM/Semicond/Si/electric.html, 2012; Vol. 2012, p Electrical properties of silicon.
(42) Bredas, J. L.; Beljonne, D.; Coropceanu, V.; Cornil, J. *Chem. Rev.* **2004**, *104*, 4971.
(43) Coropceanu, V.; Cornil, J.; da Silva Filho, D. A.; Olivier, Y.; Silbey, R.; Bredas, J.-L. *Chem. Rev.* **2007**, *107*, 926.
(44) Deibel, C.; Dyakonov, V. *Rep. Prog. Phys.* **2010**, *73*, 096401.
(45) Petrova-Koch, V. *Springer Ser. Optical Sci.* **2009**, *140*, 1.
(46) Shaheen, S. E.; Ginley, D. S.; Jabbour, G. E. *MRS Bull.* **2005**, *30*, 10.
(47) Tang, C. W.; Albrecht, A. C. *J. Chem. Phys.* **1975**, *62*, 2139.
(48) Hill, I. G.; Kahn, A.; Soos, Z. G.; Pascal, R. A. *Chem. Phys. Lett.* **2000**, *327*, 181.
(49) Tang, C. W. *Appl. Phys. Lett.* **1986**, *48*, 183.
(50) Peumans, P.; Forrest, S. R. *Appl. Phys. Lett.* **2001**, *79*, 126.
(51) Yoo, S.; Potscavage, W. J., Jr.; Domercq, B.; Han, S.-H.; Li, T.-D.; Jones, S. C.; Szoszkiewicz, R.; Levi, D.; Riedo, E.; Marder, S. R.; Kippelen, B. *Solid-State Electron.* **2007**, *51*, 1367.
(52) Hains, A. W.; Liang, Z.; Woodhouse, M. A.; Gregg, B. A. *Chem. Rev.* **2010**, *110*, 6689.
(53) Xue, J. G.; Rand, B. P.; Uchida, S.; Forrest, S. R. *Adv. Mater.* **2005**, *17*, 66.
(54) Xue, J. G.; Rand, B. P.; Uchida, S.; Forrest, S. R. *J. Appl. Phys.* **2005**, *98*.
(55) Rand, B. P.; Li, J.; Xue, J. G.; Holmes, R. J.; Thompson, M. E.; Forrest, S. R. *Adv. Mater.* **2005**, *17*, 2714.
(56) Hiramoto, M.; Fujiwara, H.; Yokoyama, M. *Appl. Phys. Lett.* **1991**, *58*, 1062.
(57) Maennig, B.; Drechsel, J.; Gebeyehu, D.; Simon, P.; Kozlowski, F.; Werner, A.; Li, F.; Grundmann, S.; Sonntag, S.; Koch, M.; Leo, K.; Pfeiffer, M.; Hoppe, H.; Meissner, D.; Sariciftci, N. S.; Riedel, I.; Dyakonov, V.; Parisi, J. *Appl. Phys. A* **2004**, *79*, 1.
(58) Service, R. F. *Science* **2011**, *332*, 293.
(59) Athanasopoulos, S.; Emelianova, E. V.; Walker, A. B.; Beljonne, D. *Phys. Rev. B* **2009**, *80*.
(60) Würthner, F.; Meerholz, K. *Chem. Eur. J.* **2010**, *16*, 9366.
(61) Hadipour, A.; de Boer, B.; Blom, P. W. M. *Org. Electron.* **2008**, *9*, 617.
(62) Li, C.; Liu, M.; Pschirer, N. G.; Baumgarten, M.; Muellen, K. *Chem. Rev.* **2010**, *110*, 6817.
(63) Figueira-Duarte, T. M.; Muellen, K. *Chem. Rev.* **2011**, *111*, 7260.
(64) Brabec, C. J.; Heeney, M.; McCulloch, I.; Nelson, J. *Chem. Soc. Rev.* **2011**, *40*, 1185.
(65) Graetzel, M. *Acc. Chem. Res.* **2009**, *42*, 1788.
(66) Ning, Z.; Fu, Y.; Tian, H. *Energy Environ. Sci.* **2010**, *3*, 1170.
(67) Herrmann, A.; Muellen, K. *Chem. Lett.* **2006**, *35*, 978.
(68) Würthner, F. *Chem. Commun.* **2004**, 1564.
(69) Jones, B. A.; Facchetti, A.; Wasielewski, M. R.; Marks, T. J. *J. Am. Chem. Soc.* **2007**, *129*, 15259.

(70) Herbst, W.; Hunger, K. *Industrial Organic Pigments, 3rd ed.*; Wiley-VCH: Weinehim, 2006.
(71) Smith, H. *High Performance Pigments*; Wiley-VCH: Weinheim, 2003.
(72) Weil, T.; Vosch, T.; Hofkens, J.; Peneva, K.; Müllen, K. *Angew. Chem. IE* **2010**, *49*, 9068.
(73) Langhals, H. *Heterocycles* **1995**, *40*, 477.
(74) Klebe, G.; Graser, F.; Hadicke, E.; Berndt, J. *Acta Cryst. B* **1989**, *45*, 69.
(75) Hoffmann, M.; Schmidt, K.; Fritz, T.; Hasche, T.; Agranovich, V. M.; Leo, K. *Chem. Phys.* **2000**, *258*, 73.
(76) Kurrle, D.; Pflaum, J. *Appl. Phys. Lett.* **2008**, *92*, 133306.
(77) Lunt, R. R.; Benziger, J. B.; Forrest, S. R. *Adv. Mater.* **2010**, *22*, 1233.
(78) Stubinger, T.; Brutting, W. *J. Appl. Phys.* **2001**, *90*, 3632.
(79) Durr, A. C.; Schreiber, F.; Munch, M.; Karl, N.; Krause, B.; Kruppa, V.; Dosch, H. *Appl. Phys. Lett.* **2002**, *81*, 2276.
(80) Tripathi, A. K.; Pflaum, J. *Appl. Phys. Lett.* **2006**, *89*.
(81) Heinrich, M. A.; Pflaum, J.; Tripathi, A. K.; Frey, W.; Steigerwald, M. L.; Siegrist, T. *J. Phys. Chem. C* **2007**, *111*, 18878.
(82) Durr, A. C.; Nickel, B.; Shan-Fia, V.; Taffner, U.; Dosch, H. *Thin Solid Films* **2006**, *503*, 127.
(83) Brutting, W. *Physics of Organic Semiconductors*; Wiley-VCH: Weinheim, 2005.
(84) Schreiber, F. *Phys. Status Solidi A* **2004**, *201*, 1037.
(85) Meiss, J.; Hermenau, M.; Tress, W.; Schuenemann, C.; Selzer, F.; Hummert, M.; Alex, J.; Lackner, G.; Leo, K.; Riede, M. *Phys. Rev. B* **2011**, *83*.
(86) Wagner, J.; Gruber, M.; Hinderhofer, A.; Wilke, A.; Broeker, B.; Frisch, J.; Amsalem, P.; Vollmer, A.; Opitz, A.; Koch, N.; Schreiber, F.; Bruetting, W. *Adv. Funct. Mater.* **2010**, *20*, 4295.
(87) Huang, C.; Barlow, S.; Marder, S. R. *J. Org. Chem.* **2011**, *76*, 2386.
(88) Rogovik, V. I.; Gutnik, L. F. *Zh. Org. Khim.* **1988**, *24*, 635.
(89) Seybold, G.; Wagenblast, G. *Dyes Pigments* **1989**, *11*, 303.
(90) Fan, L. Q.; Xu, Y. P.; Tian, H. *Tetrahedron Lett.* **2005**, *46*, 4443.
(91) Lu, X.; Guo, Z.; Sun, C.; Tian, H.; Zhu, W. *J. Phys. Chem. B* **2011**, *115*, 10871.
(92) Posch, P.; Thelakkat, M.; Schmidt, H. W. *Synt. Met.* **1999**, *102*, 1110.
(93) Schneider, M.; Müllen, K. *J. Chem. Mater.* **2000**, *12*, 352.
(94) Eversloh, C. L.; Li, C.; Muellen, K. *Org. Lett.* **2011**, *13*, 4148.
(95) Schmidt, R.; Oh, J. H.; Sun, Y.-S.; Deppisch, M.; Krause, A.-M.; Radacki, K.; Braunschweig, H.; Koenemann, M.; Erk, P.; Bao, Z.; Wuerthner, F. *J. Am. Chem. Soc.* **2009**, *131*, 6215.
(96) Wuerthner, F.; Stolte, M. *Chem. Commun.* **2011**, *47*, 5109.
(97) Sharma, G. D.; Suresh, P.; Mikroyannidis, J. A.; Stylianakis, M. M. *J. Mater. Chem.* **2010**, *20*, 561.
(98) Holtrup, F. O.; Muller, G. R. J.; Quante, H.; Defeyter, S.; DeSchryver, F. C.; Müllen, K. *Chem. Eur. J.* **1997**, *3*, 219.
(99) Quante, H.; Müllen, K. *Angew. Chem. IE* **1995**, *34*, 1323.
(100) Avlasevich, Y.; Li, C.; Muellen, K. *J. Mater. Chem.* **2010**, *20*, 3814.
(101) Li, C.; Liu, Z.; Schöneboom, J.; Eickemeyer, F.; Pschirer, N. G.; Erk, P.; Herrmann, A.; Müllen, K. *J. Mater. Chem.* **2009**, *19*, 5405.
(102) Nakazono, S.; Easwaramoorthi, S.; Kim, D.; Shinokubo, H.; Osuka, A. *Org. Lett.* **2009**, *11*, 5426.
(103) Nakazono, S.; Imazaki, Y.; Yoo, H.; Yang, J.; Sasamori, T.; Tokitoh, N.; Cedric, T.; Kageyama, H.; Kim, D.; Shinokubo, H.; Osuka, A. *Chem. Eur. J.* **2009**, *15*, 7530.
(104) Battagliarin, G.; Li, C.; Enkelmann, V.; Muellen, K. *Org. Lett.* **2011**, *13*, 3012.
(105) Teraoka, T.; Hiroto, S.; Shinokubo, H. *Org. Lett.* **2011**, *13*, 2532.
(106) Kamm, V.; Battagliarin, G.; Howard, I. A.; Pisula, W.; Mavrinskiy, A.; Li, C.; Muellen, K.; Laquai, F. *Adv. Energy Mater.* **2011**, *1*, 297.
(107) Peumans, P.; Uchida, S.; Forrest, S. R. *Nature* **2003**, *425*, 158.
(108) Halls, J. J. M.; Walsh, C. A.; Greenham, N. C.; Marseglia, E. A.; Friend, R. H.; Moratti, S. C.; Holmes, A. B. *Nature* **1995**, *376*, 498.

(109) Sun, Y. R.; Giebink, N. C.; Kanno, H.; Ma, B. W.; Thompson, M. E.; Forrest, S. R. *Nature* **2006**, *440*, 908.
(110) Friend, R. H.; Gymer, R. W.; Holmes, A. B.; Burroughes, J. H.; Marks, R. N.; Taliani, C.; Bradley, D. D. C.; Dos Santos, D. A.; Bredas, J. L.; Logdlund, M.; Salaneck, W. R. *Nature* **1999**, *397*, 121.
(111) Williams, R. T.; Song, K. S. *J. Phys. Chem. Solids* **1990**, *51*, 679.
(112) Busby, E.; Carroll, E. C.; Chinn, E. M.; Chang, L.; Moule, A. J.; Larsen, D. S. *J. Phys. Chem. Lett.* **2011**, *2*, 2764.
(113) Barford, W.; Boczarow, I.; Wharram, T. *J. Phys. Chem. A* **2011**, *115*, 9111.
(114) May, V.; Kühn, O. *Charge and Energy Transfer Dynamics in Molecular Systems*; Wiley-VCH: Weinheim, 2004.
(115) Förster, T. *Ann. Phys.* **1948**, *2*, 55.
(116) Fink, R. F.; Pfister, J.; Zhao, H. M.; Engels, B. *Chem. Phys.* **2008**, *346*, 275.
(117) Pfister, J. PhD thesis, Julius-Maximilians-Universität Würzburg, 2011.
(118) Vangrondelle, R.; Dekker, J. P.; Gillbro, T.; Sundstrom, V. *Biochim. Biophys. Acta* **1994**, *1187*, 1.
(119) Davydov, A. S. *Zh. Eksp. Teor. Fiz.* **1948**, *18*, 210.
(120) Davydov, A. S. *Theory of Molecular Excitons*; McGraw-Hill: New York, 1962.
(121) Marcus, R. A. *Rev. Mod. Phys.* **1993**, *65*, 599.
(122) Marcus, R. A.; Sutin, N. *Biochim. Biophys. Acta* **1985**, *811*, 265.
(123) Hush, N. S. *J. Chem. Phys.* **1958**, *28*, 962.
(124) Stehr, V.; Pfister, J.; Fink, R. F.; Engels, B.; Deibel, C. *Phys. Rev. B* **2011**, *83*.
(125) Shaw, P. E.; Ruseckas, A.; Samuel, I. D. W. *Adv. Mater.* **2008**, *20*, 3516.
(126) Landau, L. D. *Phys. Z. Sowj.* **1933**, *3*, 664.
(127) Mott, N. F. *Electronic processes in ionic crystals*; 2d ed. ed.; Dover Publications: New York, 1964.
(128) Mott, N. F.; Stoneham, A. M. *Journal of Physics C-Solid State Physics* **1977**, *10*, 3391.
(129) Toyozawa, Y. *J. Phys. Soc. Jpn.* **1978**, *44*, 482.
(130) Castner, T. G.; Känzig, W. *J. Phys. Chem. Solids* **1957**, *3*, 178.
(131) Känzig, W. *Phys. Rev.* **1955**, *99*, 1890.
(132) Schoemaker, D. *Phys. Rev. B* **1973**, *7*, 786.
(133) Loveland, R. J.; Spear, W. E.; Lecomber, P. G. *Phys. Lett. A* **1972**, *A 39*, 225.
(134) Kanzaki, H.; Suemoto, T. *Semicond. Insul.* **1983**, *5*, 345.
(135) Leung, C. H.; Emery, L.; Song, K. S. *Phys. Rev. B* **1983**, *28*, 3474.
(136) Engel, V.; Metiu, H.; Almeida, R.; Marcus, R. A.; Zewail, A. H. *Chem. Phys. Lett.* **1988**, *152*, 1.
(137) Sobolewski, A. L.; Domcke, W. *ChemPhysChem* **2006**, *7*, 561.
(138) Schultz, T.; Samoylova, E.; Radloff, W.; Hertel, I. V.; Sobolewski, A. L.; Domcke, W. *Science* **2004**, *306*, 1765.
(139) Bendich, A.; Olson, J. A. *Faseb J.* **1989**, *3*, 1927.
(140) Hauptmann, S. *Organische Chemie*; Wiley-VCH: Weinheim, 1991.
(141) Glowe, J.-F.; Perrin, M.; Beljonne, D.; Hayes, S. C.; Gardebien, F.; Silva, C. *Phys. Rev. B* **2010**, *81*.
(142) Psiachos, D.; Mazumdar, S. *Phys. Rev. B* **2009**, *79*, 155106.
(143) Rossi, L.; Bongiovanni, G.; Borghesi, A.; Lanzani, G.; Kalinowski, J.; Mura, A.; Tubino, R. *Synt. Met.* **1997**, *84*, 873.
(144) Platt, A. D.; Kendrick, M. J.; Loth, M.; Anthony, J. E.; Ostroverkhova, O. *Phys. Rev. B* **2011**, *84*.
(145) Jursenas, S.; Gulbinas, V.; Kuprionis, Z.; Kananavicius, R.; Kodis, G.; Gustavsson, T.; Mialocq, J. C.; Valkunas, L. *Synt. Met.* **2000**, *109*, 169.
(146) Spano, F. C.; Meskers, S. C. J.; Hennebicq, E.; Beljonne, D. *J. Am. Chem. Soc.* **2007**, *129*, 7044.
(147) Howard, I. A.; Laquai, F.; Keivanidis, P. E.; Friend, R. H.; Greenham, N. C. *J. Phys. Chem. C* **2009**, *113*, 21225.
(148) Chang, M. H.; Frampton, M. J.; Anderson, H. L.; Herz, L. M. *Phys. Rev. Lett.* **2007**, *98*, 027402.
(149) Dykstra, T. E.; Hennebicq, E.; Beljonne, D.; Gierschner, J.; Claudio, G.; Bittner, E. R.; Knoester, J.; Scholes, G. D. *J. Phys. Chem. B* **2009**, *113*, 656.

(150) Traub, M. C.; Vogelsang, J.; Plunkett, K. N.; Nuckolls, C.; Barbara, P. F.; Vanden Bout, D. A. *ACS Nano* **2012**, *6*, 523.
(151) Blatchford, J. W.; Jessen, S. W.; Lin, L. B.; Gustafson, T. L.; Fu, D. K.; Wang, H. L.; Swager, T. M.; MacDiarmid, A. G.; Epstein, A. J. *Phys. Rev. B* **1996**, *54*, 9180.
(152) Athanasopoulos, S.; Hennebicq, E.; Beljonne, D.; Walker, A. B. *J. Phys. Chem. C* **2008**, *112*, 11532.
(153) Bolinger, J. C.; Traub, M. C.; Adachi, T.; Barbara, P. F. *Science* **2011**, *331*, 565.
(154) Kim, D. Y.; Grey, J. K.; Barbara, P. F. *Synt. Met.* **2006**, *156*, 336.
(155) Yang, J.; Zhu, F.; Yu, B.; Wang, H.; Yan, D. *Appl. Phys. Lett.* **2012**, *100*, 103305.
(156) Camerman, A.; Trotter, J. *Proceedings of the Royal Society of London Series a-Mathematical and Physical Sciences* **1964**, *279*, 129.
(157) Tanaka, J. *Bull. Chem. Soc. Jap.* **1963**, *36*, 1237.
(158) West, B. A.; Womick, J. M.; McNeil, L. E.; Tan, K. J.; Moran, A. M. *J. Phys. Chem. B* **2011**, *115*, 5157.
(159) Hochstrasser, R. M.; Nyi, C. A. *J. Chem. Phys.* **1980**, *72*, 2591.
(160) Nelson, K. A.; Dlott, D. D.; Fayer, M. D. *Chem. Phys. Lett.* **1979**, *64*, 88.
(161) Tamai, N.; Porter, C. F.; Masuhara, H. *Chem. Phys. Lett.* **1993**, *211*, 364.
(162) Yago, T.; Tamaki, Y.; Furube, A.; Katoh, R. *Phys. Chem. Chem. Phys.* **2008**, *10*, 4435.
(163) Furube, A.; Murai, M.; Tamaki, Y.; Watanabe, S.; Katoh, R. *J. Phys. Chem. A* **2006**, *110*, 6465.
(164) Vonfreydorf, E.; Kinder, J.; Michelbeyerle, M. E. *Chem. Phys.* **1978**, *27*, 199.
(165) Graaf, H.; Friedriszik, F.; Wagner, C.; von Borczyskowski, C. *J. Phys. Chem. C* **2011**, *115*, 8150.
(166) Schlosser, M.; Lochbrunner, S. *J. Phys. Chem. B* **2006**, *110*, 6001.
(167) Erwin, P.; Thompson, M. E. *Appl. Phys. Lett.* **2011**, *98*, 223305.
(168) Fink, R. F.; Seibt, J.; Engel, V.; Renz, M.; Kaupp, M.; Lochbrunner, S.; Zhao, H. M.; Pfister, J.; Würthner, F.; Engels, B. *J. Am. Chem. Soc.* **2008**, *130*, 12858.
(169) Koch, H.; Jorgensen, P. *J. Chem. Phys.* **1990**, *93*, 3333.
(170) Olsen, J.; Jorgensen, P. *Modern Electronic Structure Theory Part II*; World Scientific Publishing Co. Pte. Ltd.: Singapore, 1995.
(171) Olsen, J.; Jorgensen, P. *J. Chem. Phys.* **1985**, *82*, 3235.
(172) Dreuw, A.; Head-Gordon, M. *Chem. Rev.* **2005**, *105*, 4009.
(173) Szabo, A.; Ostlund, N. S. *Modern Quantum Chemistry - Introduction to Advanced Electronic Structure Theory* New York, 1989.
(174) Weigend, F.; Häser, M. *Theor. Chem. Acc.* **1997**, *97*, 331.
(175) McWeeny, R. *Methods of Molecular Quantum Mechanics*; 2nd Edition ed.; Academic Press Limited: London, 1989.
(176) Runge, E.; Gross, E. K. U. *Phys. Rev. Lett.* **1984**, *52*, 997.
(177) van Leeuwen, R. *Phys. Rev. Lett.* **1999**, *82*, 3863.
(178) Peach, M. J. G.; Benfield, P.; Helgaker, T.; Tozer, D. J. *J. Chem. Phys.* **2008**, *128*, 044118.
(179) Helgaker, T.; Jorgensen, P.; Olsen, J. *Molecular Electronic-Structure Theory*; John Wiley & Sons Ltd: Chichester, 2000.
(180) Christiansen, O.; Koch, H.; Jorgensen, P. *Chem. Phys. Lett.* **1995**, *243*, 409.
(181) Hättig, C.; Weigend, F. *J. Chem. Phys.* **2000**, *113*, 5154.
(182) Christiansen, O.; Koch, H.; Jorgensen, P. *J. Chem. Phys.* **1995**, *103*, 7429.
(183) Christiansen, O.; Koch, H.; Halkier, A.; Jorgensen, P.; Helgaker, T.; deMeras, A. S. *J. Chem. Phys.* **1996**, *105*, 6921.
(184) Hättig, C. In *Advances in Quantum Chemistry, Vol 50: A Tribute to Jan Linderberg and Poul Jorgensen*; Sabin, J. R. B. E., Ed. 2005; Vol. 50, p 37.
(185) Trofimov, A. B.; Krivdina, I. L.; Weller, J.; Schirmer, J. *Chem. Phys.* **2006**, *329*, 1.
(186) Wormit, M. PhD thesis, Johann Wolfgang Goethe Universität Frankfurt am Main, 2009.
(187) Starcke, J. H.; Wormit, M.; Dreuw, A. *J. Chem. Phys.* **2009**, *130*.
(188) Grimme, S. *J. Comput. Chem.* **2004**, *25*, 1463.

(189) Grimme, S. *J. Comput. Chem.* **2006**, *27*, 1787.
(190) Dirac, P. A. M. *Proc. Royal Soc. A* **1929**, *123*, 714.
(191) Slater, J. C. *Phys. Rev.* **1951**, *81*, 385.
(192) Lee, C. T.; Yang, W. T.; Parr, R. G. *Phys. Rev. B* **1988**, *37*, 785.
(193) Schäfer, A.; Huber, C.; Ahlrichs, R. *J. Chem. Phys.* **1994**, *100*, 5829.
(194) Weigend, F.; Häser, M.; Patzelt, H.; Ahlrichs, R. *Chem. Phys. Lett.* **1998**, *294*, 143.
(195) Grimme, S. *J. Chem. Phys.* **2003**, *118*, 9095.
(196) Hättig, C.; Köhn, A. *J. Chem. Phys.* **2002**, *117*, 6939.
(197) Hellweg, A.; Grün, S. A.; Hättig, C. *Phys. Chem. Chem. Phys.* **2008**, *10*, 4119.
(198) Schäfer, A.; Horn, H.; Ahlrichs, R. *J. Chem. Phys.* **1992**, *97*, 2571.
(199) Eichkorn, K.; Treutler, O.; Öhm, H.; Häser, M.; Ahlrichs, R. *Chem. Phys. Lett.* **1995**, *242*, 652.
(200) Eichkorn, K.; Weigend, F.; Treutler, O.; Ahlrichs, R. *Theor. Chem. Acc.* **1997**, *97*, 119.
(201) TURBOMOLE V6.0 2009 a development of University of Karlsruhe and Forschungszentrum Karlsruhe GmbH 1989-2007 TURBOMOLE GmbH since 2007.
(202) Liu, W.; Settels, V.; Fink, R. F.; Engels, B. *in preparation* **2012**.
(203) Liu, W. PhD thesis, Universität Würzburg, 2011.
(204) Tafipolsky, M.; Engels, B. *J. Chem. Theory Comput.* **2011**, *7*, 1791.
(205) Kasha, M.; Rawls, H. R.; Bayoumi, M. A. E. *Pure Appl. Chem.* **1965**, *11*, 371.
(206) Scholes, G. D. *Annu. Rev. Phys. Chem.* **2003**, *54*, 57.
(207) Dexter, D. L. *J. Chem. Phys.* **1953**, *21*, 836.
(208) Gierschner, J.; Huang, Y.-S.; Van Averbeke, B.; Cornil, J.; Friend, R. H.; Beljonne, D. *J. Chem. Phys.* **2009**, *130*, 044105.
(209) Fückel, B.; Köhn, A.; Harding, M. E.; Diezemann, G.; Hinze, G.; Basche, T.; Gauss, J. *J. Chem. Phys.* **2008**, *128*, 074505.
(210) Scholes, G. D.; Curutchet, C.; Mennucci, B.; Cammi, R.; Tomasi, J. *J. Phys. Chem. B* **2007**, *111*, 6978.
(211) Scholz, R.; Kobitski, A. Y.; Zahn, D. R. T.; Schreiber, M. *Phys. Rev. B* **2005**, *72*, 245208.
(212) Havil, J.; Dyson, F. *Gamma: Exploring Euler's Constant*; Princeton University Press: Princeton, 2003.
(213) Steuding, J. *Diophantine Analysis*; Chapman & Hall: Boca Raton, 2005.
(214) Ponder, J. W.; Ren, P.; Pappu, R. V.; Hart, R. K.; Hodgson, M. E.; Cistola, D. P.; Kundrot, C. E.; Richards, F. M.; 5.1 ed.; Washington University School of Medicine: St. Louis, http://dasher.wustl.edu/tinker/, 2010.
(215) Stone, A. J. *J. Chem. Theory Comput.* **2005**, *1*, 1128.
(216) Stone, A. J. http://www-stone.ch.cam.ac.uk/programs.html, 2011.
(217) Becke, A. D. *Phys. Rev. A* **1988**, *38*, 3098.
(218) Becke, A. D. *J. Chem. Phys.* **1993**, *98*, 5648.
(219) Zhao, H. M.; Pfister, J.; Settels, V.; Renz, M.; Kaupp, M.; Dehm, V. C.; Würthner, F.; Fink, R. F.; Engels, B. *J. Am. Chem. Soc.* **2009**, *131*, 15660.
(220) Frisch, M. J.; Trucks, G. W.; Schlegel, H. B.; Scuseria, G. E.; Rob, M. A.; Cheeseman, J. R.; Montgomery Jr., J. A.; Vreven, T.; Kudin, K. N.; Burant, J. C.; Millam, J. M.; Iyengar, S. S.; Tomasi, J.; Barone, V.; Mennucci, B.; Cossi, M.; Scalmani, G.; Rega, N.; Petersson, G. A.; Nakatsuji, H.; Hada, M.; Ehara, M.; Toyota, K.; Fukuda, R.; Hasegawa, J.; Ishida, M.; Nakajima, T.; Honda, Y.; Kitao, O.; Nakai, H.; Klene, M.; Li, X.; Knox, J. E.; Hratchian, H. P.; Cross, J. B.; Bakken, V.; Adamo, C.; Jaramillo, J.; Gomperts, R.; Stratmann, R. E.; Yazyev, O.; Austin, A. J.; Cammi, R.; Pomelli, C.; Ochterski, J. W.; Ayala, P. Y.; Morokuma, K.; Voth, G. A.; Salvador, P.; Dannenberg, J. J.; Zakrzewski, V. G.; Dapprich, S.; Daniels, A. D.; Strain, M. C.; Farkas, O.; Malick, D. K.; Rabuck, A. D.; Raghavachari, K.; Foresman, J. B.; Ortiz, J. V.; Cui, Q.; Baboul, A. G.; Clifford, S.; Cioslowski, J.; Stefanov, B. B.; Liu, G.; Liashenko, A.; Piskorz, P.; Komaromi, I.; Martin, R. L.; Fox, D. J.; Keith, T.; Al-Laham, M. A.; Peng, C. Y.; Nanayakkara, A.; Challacombe,

M.; Gill, P. M. W.; Johnson, B.; Chen, W.; Wong, M. W.; Gonzalez, C.; Pople, J. A.; Gaussian, Inc.: Wallingford, CT, 2003.
(221) Francl, M. M.; Pietro, W. J.; Hehre, W. J.; Binkley, J. S.; Gordon, M. S.; Defrees, D. J.; Pople, J. A. *Journal of Chemical Physics* **1982**, *77*, 3654.
(222) Hehre, W. J.; Ditchfie.R; Pople, J. A. *J. Chem. Phys.* **1972**, *56*, 2257.
(223) Gordon, M. S. *Chem. Phys. Lett.* **1980**, *76*, 163.
(224) Frisch, M. J.; Pople, J. A.; Binkley, J. S. *J. Chem. Phys.* **1984**, *80*, 3265.
(225) Bauernschmitt, R.; Ahlrichs, R. *Chem. Phys. Lett.* **1996**, *256*, 454.
(226) Casida, M. E.; Jamorski, C.; Casida, K. C.; Salahub, D. R. *J. Chem. Phys.* **1998**, *108*, 4439.
(227) Stratmann, R. E.; Scuseria, G. E.; Frisch, M. J. *J. Chem. Phys.* **1998**, *109*, 8218.
(228) Furche, F.; Ahlrichs, R. *J. Chem. Phys.* **2002**, *117*, 7433.
(229) Scalmani, G.; Frisch, M. J.; Mennucci, B.; Tomasi, J.; Cammi, R.; Barone, V. *J. Chem. Phys.* **2006**, *124*.
(230) Liu, W.; Settels, V.; Harbach, P. H. P.; Dreuw, A.; Fink, R. F.; Engels, B. *J. Comput. Chem.* **2011**, *32*, 1971.
(231) Mennucci, B.; Cammi, R.; Tomasi, J. *J. Chem. Phys.* **1998**, *109*, 2798.
(232) Cances, E.; Mennucci, B.; Tomasi, J. *J. Chem. Phys.* **1997**, *107*, 3032.
(233) Mennucci, B.; Cances, E.; Tomasi, J. *J. Phys. Chem. B* **1997**, *101*, 10506.
(234) Tomasi, J.; Mennucci, B.; Cammi, R. *Chem. Rev.* **2005**, *105*, 2999.
(235) Santoro, F.; Barone, V.; Gustavsson, T.; Improta, R. *J. Am. Chem. Soc.* **2006**, *128*, 16312.
(236) Yesudas, K.; Chaitanya, G. K.; Prabhakar, C.; Bhanuprakash, K.; Rao, V. J. *J. Phys. Chem. A* **2006**, *110*, 11717.
(237) Crespo-Hernandez, C. E.; Burdzinski, G.; Arce, R. *J. Phys. Chem. A* **2008**, *112*, 6313.
(238) Curutchet, C.; Mennucci, B.; Scholes, G. D.; Beljonne, D. *J. Phys. Chem. B* **2008**, *112*, 3759.
(239) Liang, Y.; Zhang, R.; Jiang, F. *J. Mol. Struc. - Theochem* **2008**, *848*, 1.
(240) Alvarado-Gonzalez, M.; Flores-Holguin, N.; Gallo, M.; Orrantia-Borunda, E.; Glossman-Mitnik, D. *J. Mol. Struc. - Theochem* **2010**, *945*, 101.
(241) Cossi, M.; Barone, V. *J. Phys. Chem. A* **2000**, *104*, 10614.
(242) Bayliss, N. S. *J. Chem. Phys.* **1950**, *18*, 292.
(243) Hilborn, R. C. *Am. J. Phys.* **1982**, *50*, 982.
(244) Chako, N. Q. *J. Chem. Phys.* **1934**, *2*, 644.
(245) Van Grondelle, R.; Valkunas, L.; Van Amerongen, H. *Photosynthetic Excitons*; World Scientific Publishing Company: Singapore, 2000.
(246) Wasielewski, M. R. *Acc. Chem. Res.* **2009**, *42*, 1910.
(247) Schwoerer, M.; Wolf, C. H. *Organic Molecular Solids*; Wiley-VCH Verlag GmbH & Co. KGaA: Weinheim, 2007.
(248) Braun, A.; Mayer, U.; Auweter, H.; Wolf, H. C. *Z. Naturforsch. A* **1982**, *37*, 1013.
(249) Elkareh, T. B.; Wolf, H. C. *Z. Naturforsch. A* **1967**, *A 22*, 1242.
(250) Warta, W.; Stehle, R.; Karl, N. *Appl. Phys. A* **1985**, *36*, 163.
(251) Nishimura, H.; Yamaoka, T.; Mizuno, K.; Iemura, M.; Matsui, A. *J. Phys. Soc. Jpn.* **1984**, *53*, 3999.
(252) Kotani, M.; Kakinuma, K.; Yoshimura, M.; Ishii, K.; Yamazaki, S.; Kobori, T.; Okuyama, H.; Kobayashi, H.; Tada, H. *Chem. Phys.* **2006**, *325*, 160.
(253) Zhan, X.; Facchetti, A.; Barlow, S.; Marks, T. J.; Ratner, M. A.; Wasielewski, M. R.; Marder, S. R. *Adv. Mater.* **2011**, *23*, 268.
(254) Chen, Z. J.; Stepanenko, V.; Dehm, V.; Prins, P.; Siebbeles, L. D. A.; Seibt, J.; Marquetand, P.; Engel, V.; Würthner, F. *Chem. Eur. J.* **2007**, *13*, 436.
(255) Settels, V.; Schubert, A.; Liu, W.; Würthner, F.; Meier, C.; Fink, R. F.; Schindlbeck, S.; Lochbrunner, S.; Engels, B.; Engel, E. *in preparation* **2012**.
(256) Lauvergnat, D.; Nauts, A. *J. Chem. Phys.* **2002**, *116*, 8560.
(257) Schubert, A. PhD thesis, Universität Würzburg, 2012.

(258) Feit, M. D.; Fleck, J. A.; Steiger, A. *J. Comput. Phys.* **1982**, *47*, 412.
(259) Molmer, K.; Castin, Y.; Dalibard, J. *J. Opt. Soc. Am. B* **1993**, *10*, 524.
(260) Makarov, D. E.; Metiu, H. *J. Chem. Phys.* **1999**, *111*, 10126.
(261) Giaimo, J. M.; Gusev, A. V.; Wasielewski, M. R. *J. Am. Chem. Soc.* **2002**, *124*, 8530.
(262) Hippius, C.; van Stokkum, I. H. M.; Zangrando, E.; Williams, R. M.; Wykes, M.; Beljonne, D.; Würthner, F. *J. Phys. Chem. C* **2008**, *112*, 14626.
(263) Spano, F. C. *Acc. Chem. Res.* **2010**, *43*, 429.
(264) Roden, J.; Eisfeld, A.; Dvorak, M.; Buenermann, O.; Stienkemeier, F. *J. Chem. Phys.* **2011**, *134*.
(265) Bakulin, A. A.; Rao, A.; Pavelyev, V. G.; van Loosdrecht, P. H. M.; Pshenichnikov, M. S.; Niedzialek, D.; Cornil, J.; Beljonne, D.; Friend, R. H. *Science* **2012**, *335*, 1340.
(266) Beljonne, D.; Cornil, J.; Muccioli, L.; Zannoni, C.; Bredas, J.-L.; Castet, F. *J. Chem. Mater.* **2011**, *23*, 591.
(267) Collini, E.; Scholes, G. D. *Science* **2009**, *323*, 369.
(268) Heremans, P.; Cheyns, D.; Rand, B. P. *Acc. Chem. Res.* **2009**, *42*, 1740.
(269) Schmidt-Mende, L.; Fechtenkotter, A.; Müllen, K.; Moons, E.; Friend, R. H.; MacKenzie, J. D. *Science* **2001**, *293*, 1119.
(270) Forrest, S. R. *Chem. Rev.* **1997**, *97*, 1793.
(271) Giaimo, J. M.; Lockard, J. V.; Sinks, L. E.; Scott, A. M.; Wilson, T. M.; Wasielewski, M. R. *J. Phys. Chem. A* **2008**, *112*, 2322.
(272) Gisslen, L.; Scholz, R. *Phys. Rev. B* **2009**, *80*, 115309.
(273) Settels, V.; Liu, W.; Pflaum, J.; Fink, R. F.; Engels, B. *J. Comput. Chem.* **2012**, *33*, 1544.
(274) Scholes, G. D.; Rumbles, G. *Nature Mater.* **2006**, *5*, 683.
(275) Heinemeyer, U.; Scholz, R.; Gisslen, L.; Alonso, M. I.; Osso, J. O.; Garriga, M.; Hinderhofer, A.; Kytka, M.; Kowarik, S.; Gerlach, A.; Schreiber, F. *Phys. Rev. B* **2008**, *78*.
(276) Scholz, R.; Schreiber, M. *Chem. Phys.* **2006**, *325*, 9.
(277) Domcke, W.; Yarkony, D. R.; Köppel, H. *Conical Intersections: Electronic Structure, Dynamics & Spectroscopy: Electronic Structure, Dynamics and Spectroscopy*; World Scientific Publishing: Singapore, 2004.
(278) Kosloff, R.; Tal-Ezer, H. *Chem. Phys. Lett.* **1986**, *127*, 223.
(279) Podolsky, B. *Phys. Rev.* **1928**, *32*, 812.
(280) Nauts, A.; Chapuisat, X. *Mol. Phys.* **1985**, *55*, 1287.
(281) Ziessel, R.; Harriman, A. *Chem. Commun.* **2011**, *47*, 611.
(282) Soos, Z. G.; Hennessy, M. H.; Wen, G. *Chem. Phys.* **1998**, *227*, 19.
(283) Kazmaier, P. M.; Hoffmann, R. *J. Am. Chem. Soc.* **1994**, *116*, 9684.
(284) Vura-Weis, J.; Ratner, M. A.; Wasielewski, M. R. *J. Am. Chem. Soc.* **2010**, *132*, 1738.
(285) Cornil, J.; Beljonne, D.; Calbert, J. P.; Bredas, J. L. *Adv. Mater.* **2001**, *13*, 1053.
(286) Burquel, A.; Lemaur, V.; Beljonne, D.; Lazzaroni, R.; Cornil, J. *J. Phys. Chem. A* **2006**, *110*, 3447.
(287) Engel, E.; Schmidt, K.; Beljonne, D.; Bredas, J. L.; Assa, J.; Frob, H.; Leo, K.; Hoffmann, M. *Phys. Rev. B* **2006**, *73*, 245216.
(288) Clark, A. E.; Qin, C. Y.; Li, A. D. Q. *J. Am. Chem. Soc.* **2007**, *129*, 7586.
(289) Gregg, B. A.; Hanna, M. C. *J. Appl. Phys.* **2003**, *93*, 3605.
(290) Gregg, B. A. *J. Phys. Chem. B* **2003**, *107*, 4688.
(291) Gregg, B. A. *J. Phys. Chem.* **1996**, *100*, 852.
(292) Conboy, J. C.; Olson, E. J. C.; Adams, D. M.; Kerimo, J.; Zaban, A.; Gregg, B. A.; Barbara, P. F. *J. Phys. Chem. B* **1998**, *102*, 4516.
(293) Gomez, U.; Leonhardt, M.; Port, H.; Wolf, H. C. *Chem. Phys. Lett.* **1997**, *268*, 1.
(294) Bulovic, V.; Burrows, P. E.; Forrest, S. R.; Cronin, J. A.; Thompson, M. E. *Chem. Phys.* **1996**, *210*, 1.
(295) Gangilenka, V. R.; Titova, L. V.; Smith, L. M.; Wagner, H. P.; DeSilva, L. A. A.; Gisslen, L.; Scholz, R. *Phys. Rev. B* **2010**, *81*, 155208.

(296) Settels, V.; Schubert, A.; Tafipolsky, M.; Liu, W.; Stehr, V.; Topczak, A. K.; Pflaum, J.; Deibel, C.; Engel, V.; Fink, R. F.; Engels, B. *submitted* **2012**.
(297) Tojo, K.; Mizuguchi, J. *Z. Kristallogr.* **2002**, *217*, 253.
(298) Zollinger, H. *Color Chemistry: Syntheses, Properties, and Applications of Organic Dyes and Pigments*; 3 ed.; Wiley-VCH: Weinheim, 2003.
(299) Shaheen, S. E.; Jabbour, G. E.; Kippelen, B.; Peyghambarian, N.; Anderson, J. D.; Marder, S. R.; Armstrong, N. R.; Bellmann, E.; Grubbs, R. H. *Appl. Phys. Lett.* **1999**, *74*, 3212.
(300) Katz, H. E.; Lovinger, A. J.; Johnson, J.; Kloc, C.; Siegrist, T.; Li, W.; Lin, Y. Y.; Dodabalapur, A. *Nature* **2000**, *404*, 478.
(301) Bao, Z. N. *Adv. Mater.* **2000**, *12*, 227.
(302) Scholz, R.; Kobitski, A. Y.; Vragovic, I.; Wagner, H. P.; Zahn, D. R. T. *Org. Electron.* **2004**, *5*, 99.
(303) Veldman, D.; Chopin, S. M. A.; Meskers, S. C. J.; Janssen, R. A. J. *Journal of Physical Chemistry A* **2008**, *112*, 8617.
(304) Heinz, H.; Suter, U. W.; Leontidis, E. *J. Am. Chem. Soc.* **2001**, *123*, 11229.
(305) Munoz-Losa, A.; Curutchet, C.; Fdez Galvan, I.; Mennucci, B. *J. Chem. Phys.* **2008**, *129*, 034104.
(306) Curutchet, C.; Munoz-Losa, A.; Monti, S.; Kongsted, J.; Scholes, G. D.; Mennucci, B. *J. Chem. Theory Comput.* **2009**, *5*, 1838.
(307) Neugebauer, J.; Curutchet, C.; Munoz-Losa, A.; Mennucci, B. *Journal of Chemical Theory and Computation* **2010**, *6*, 1843.
(308) Dreuw, A.; Head-Gordon, M. *J. Am. Chem. Soc.* **2004**, *126*, 4007.
(309) Alonso, M. I.; Garriga, M.; Karl, N.; Osso, J. O.; Schreiber, F. *Org. Electron.* **2002**, *3*, 23.

# List of abbreviations

| | |
|---|---|
| ADC | Algebraic diagrammatic construction |
| ALDA | Adiabatic local density approximation |
| AO | Atomic orbital |
| BCH | Baker-Campbell-Hausdorff (series) |
| CASPT2 | 2$^{nd}$ order complete active space perturbation theory |
| CASSCF | Complete active space self-consistent field theory |
| CC | Coupled cluster theory |
| CCSD | Coupled cluster single and doubles method |
| CC2 | Approximate Coupled Cluster method 2nd order |
| CI | Conical intersection or configuration interaction |
| CIS | Configuration interaction singles method |
| CISD | Configuration interaction singles and doubles method |
| CT | Charge transfer (state) |
| -D | Empirical dispersion correction |
| DIP | Diindeno perylene |
| DFT | Density functional theory |
| EBL | Exciton blocking layer |
| EET | Excitation energy transfer |
| EOM | Equation of motion |
| FRET | Förster resonant energy transfer |
| fs | Femtosecond (1 fs: $10^{-15}$ s) |
| GGA | Generalized gradient approximation |
| HF | Hartree-Fock theory |
| HOMO | Highest occupied molecular orbital |
| IEFPCM | Integral equation formalism variant of the polarizable continuum model |
| IS | Inorganic semiconductor |
| ITO | Indium tin oxide |
| KS | Kohn-Sham theory |
| $L_D$ | Diffusion length |
| LR | Linear response |
| LUMO | Lowest unoccupied molecular orbital |
| MO | Molecular orbital |
| MP2 | 2$^{nd}$ order Møller-Plesset perturbation theory |
| MRCI | Multi-reference configuration interaction theory |
| nm | Nanometer (1 nm: $10^{-9}$ m) |
| ns | Nanosecond (1 ns: $10^{-9}$ s) |

| | |
|---|---|
| OPV | Organic photovoltaic or organic solar cell |
| PBI | 3,4,9,10-perylene tetracarboxylic acid bisimide |
| PEC | Potential energy curve |
| PES | Potential energy surface |
| PCM | Polarizable continuum model |
| PMI | 3,4,9,10-perylene tetracarboxylic acid monoimide |
| ps | Picosecond (1 ps: $10^{-12}$ s) |
| PTCDA | 3,4,9,10-perylene tetracarboxylic acid dianhydride |
| QM/MM | Combined quantum mechanics and molecular mechanics approach |
| RI | Resolution of identity approximation |
| SAC | Symmetry-adapted cluster |
| SCS | Spin component scaling |
| SOPPA | $2^{nd}$-order polarization propagator approximation |
| TD | Time-dependent |
| TDA | Tamm-Dancoff approximation |
| XC | Exchange correlation (functional) |

# Danksagung

An erster Stelle möchte ich mich bei Herrn Prof. Dr. Bernd Engels dafür bedanken, dass er mir eine so spannende und herausfordernde Promotion ermöglicht hat, an der er immer ein sehr großes Interesse bekundete. Diskussionen mit ihm waren stets eine Bereicherung und haben wertvolle Beiträge zu meiner Arbeit geliefert. Auch die von ihm geschaffene fachliche Umgebung in Würzburg sowie die Möglichkeit, viele internationale Konferenzen zu besuchen, waren hervorragend. Seine Fähigkeit, viele große Projekte erfolgreich einzuwerben, hat meine wissenschaftliche Arbeit nachhaltig gefördert. Für die Chance eigene Ideen zu verfolgen, bin ich ihm sehr dankbar.

Ebenso danke ich zutiefst Herrn Prof. Dr. Reinhold Fink für die außerordentlich guten wissenschaftlichen Gespräche. Ich habe sehr viel von ihm gelernt und es hat mir sehr geholfen, dass seine Tür immer offen stand. Ich habe enorm von seiner Erfahrung und seinem Engagement profitiert.

Weiterhin gilt mein Dank Herrn Prof. Dr. Volker Engel für eine exzellente Zusammenarbeit bei den in Kapitel 5 dargestellten Ergebnissen und viele konstruktive Diskussionen.

Besonders hervorheben möchte ich die äußerst produktive Zusammenarbeit mit Herrn Alexander Schubert sowie Herrn Dr. Wenlan Liu und Herrn Christoph Walter, für die ich sehr dankbar bin. Ohne diese vorbildlichen Kooperationen wäre meine Arbeit in der Form nicht möglich gewesen.

Ich danke allen Kooperationspartnern, die mich bei meiner Promotion unterstützt haben. Bei Herrn Dr. Maxim Tafipolski möchte ich mich für die Kraftfeldrechnungen an Kristallstrukturausschnitten von $\alpha$-PTCDA und DIP bedanken sowie bei Herrn Philipp Harbach und Herrn Prof. Dr. Andreas Dreuw für Rechnungen mit ADC(2)-x und long-range corrected DFT. Weiter gilt mein Dank Frau Katharina Topczak und Herrn Prof. Dr. Jens Pflaum für die Experimente an DIP-Einkristallen sowie Herrn Prof. Dr. Stefan Lochbrunner für zeitaufgelöste Experimente an PBI-Aggregaten. Auch möchte ich mich bei Herrn Dr. Ralf Tonner für plane-wave Rechnungen an Ag-Oberflächen bedanken sowie bei Herrn Markus Scholz und Herrn Priv. Doz. Dr. Achim Schöll bei der Hilfe zum Verständnis der experimentellen Funde in diesem Gebiet. Außerdem bin ich Herrn Dr. Alexander Eisfeld und Herr Prof. Dr. Frank Stienkemeier für die Zusammenarbeit bei der Strukturaufklärung von PTCDA-Dimeren dankbar. Darüber hinaus bedanke ich mich bei Herrn Dr. Alexander Eisfeld für beeindruckende wissenschaftliche Debatten in Würzburg und Dresden, die unvergessen bleiben.

Weiterhin bin ich allen Studierenden, die mit mir zusammengearbeitet haben, zu tiefem Dank verpflichtet. Besonders Herr Daniel Bellinger aber auch Anca Boariu, Tim Walter, David Bialas und Christoph Menrath haben wichtige Beiträge zu meiner Arbeit geliefert.

Außerdem gilt mein tiefster Dank Frau Uschi Rüppel für die großartige Hilfe und Stütze während meiner gesamten Zeit in Würzburg.

Allen Mitgliedern der Arbeitsgruppen Engels und Engel sowie des Graduiertenkollegs 1221 danke ich für die angenehme und erfolgreiche Zeit in Würzburg. Dies gilt besonders für Herrn Thomas Schmidt, Herrn Alexander Paasche und Herrn Johannes Becker, welche die vorbildliche Betreuung der Computercluster übernahmen, sowie für Herrn Kay Ansorg und Herrn Johannes Becker für das Schaffen des guten Arbeitsklimas.

Ich möchte mich bei Herrn Christof Walter, Herrn Alexander Schubert, Herrn Kay Ansorg, Herrn Johannes Becker, Herrn Daniel Weber, Frau Kristin Lange, Herrn Daniel Bellinger, Frau Anca Boariu, Frau Zarah Falk, Frau Katharina Werner, Frau Kathrin Hahn, Herrn Fabian Knorr, Frau Anke Horneber, Frau Sabine Stahl und Herrn Peter Buschmann für das Korrekturlesen meiner Dissertation bedanken.

Meinen Eltern, meinen Geschwistern Marion und Carsten, meiner Oma und meinen Freunden gilt mein herzlichster Dank für die großartige Unterstützung während meines Studiums und meiner Promotion. Das gleiche gilt für meine Großtante Hannelore und meinen Großonkel Stefan, die mir während der gesamten Zeit mit Rat und Tat zur Seite standen. Schön euch alle zu haben!

Bei Kristin Lange will ich mich aus ganzem Herzen dafür bedanken, dass sie für mich da ist und mir so sehr geholfen und mich gestützt hat. Ohne dich hätte ich das alles niemals erreicht!